WIRELESS SENSING OF TISSUE DEFORMATIONS FEATURING POLYMERIC MAGNETS

by

Tianshuo (Tony) Zhang

A Dissertation

Submitted to the Faculty of Purdue University

In Partial Fulfillment of the Requirements for the degree of

Doctor of Philosophy

School of Electrical and Computer Engineering

West Lafayette, Indiana

December 2020

THE PURDUE UNIVERSITY GRADUATE SCHOOL
STATEMENT OF COMMITTEE APPROVAL

Dr. Babak Ziaie, Ph.D., Chair
School of Electrical and Computer Engineering

Dr. Riyi Shi, M.D., Ph.D.
College of Veterinary Medicine

Dr. David B. Janes, Ph.D.
School of Electrical and Computer Engineering

Dr. Saeed Mohammadi, Ph.D.
School of Electrical and Computer Engineering

Approved by:
Dr. Dimitrios Peroulis

Thank you 少女, 老妈, 老爸, and 外公外婆 for years of accompany and support.

Thank you all for shaping me as who I am and inspiring me to where I am.

This is for you.

ACKNOWLEDGMENTS

This thesis details some highly interdisciplinary and collaborative study that would not be successful without the guidance, cooperation, and facilitation from senior professors and from fellow scientists and engineers. My gratitude to them are beyond words but I must acknowledge their contributions here.

First, a special thanks to my advisor, Dr. Babak Ziaie for the guidance, advice and support. You had always been teaching us to ‘think big’, to find the root cause of a problem, and to adopt application-oriented mindset, which influences me enormously. Thank you also for the kindness to endorse me academically and financially, as well as for the forgiveness on my mistakes.

Thank you to my committee: Dr. Riyi Shi, Dr. David Janes, and Dr. Saeed Mohammadi for the helps and feedbacks provided along my research progress. A major component of my research work involved continuous collaboration with Dr. Nick Race from Dr. Shi’s lab and thank you for bringing facility, material, and know-how in biomechanics and neuroscience to fuel the success of our collaboration.

Next my appreciations go to my fellow ZBML members: Manny, Albert, Sammy, Jiawei, Rahim, Hongjie, Wuyang, Chang, Mark, Zach, VJ, Jun, and Chris. Thank you all for the time we spent together in the lab, in the office, in the conferences and in the Nine Irish Brothers. I’m grateful for having each of you during this journey.

TABLE OF CONTENTS

LIST OF TABLES

LIST OF FIGURES

ABSTRACT

Measurement of physiological deformations in specific tissues can provide significant information for the diagnosis, monitoring, and treatment of medical conditions. Yet these deformation measurements can be hard to obtain, especially when the targeted tissue is inside the body where optical access is denied. Current medical imaging technologies, including ultrasound, magnetic resonance imaging (MRI) and X-ray, can image soft tissues and bones with decent spatial resolution. However, they are not feasible for chronic tissue monitoring or cases in which rapid tissue deformation/vibration measurements are required. Wireless magnetic sensing is a favorable option for implantable pressure, strain, or deformation sensing systems due to its compact size, passiveness, high sampling rate and minimal interference from biological materials. Polymeric magnets, made from polymer carrier and embedded magnetic micro/nano-particles, possess the traits of flexibility, stretchability and biocompatibility that are preferred for biomedical applications. Nonetheless, their magnetic field is much weaker comparing to that of traditional ferrous/rare earth magnets. Emergence of highly sensitive magnetic sensors based on various principles (Hall effect, anisotropic magneto-resistance (AMR), giant magneto-resistance (GMR), giant magneto-impedance (GMI), tunneling magneto-resistance (TMR)) has enabled precise magnetic sensing of such polymeric magnets. To this end, we developed wireless magnetic sensing systems capable of measuring tissue deformations through implantable polymeric magnets for biomedical applications. This thesis work details the end-to-end development (magnetic sensor selection, magnetic transducer design & fabrication, measurement algorithm development) and the collaborative, interdisciplinary experiment result of a wireless brain deformation sensing system for blast induced traumatic brain injury (bTBI) featuring a polymeric magnetic disk, and a wireless strain sensing system for bladder dysfunction or heart failure (HF) featuring a stretchable polymeric magnetic band. Both systems comprise of one or more polymeric magnetic transducers, an external magnetic sensor / sensor array, and a signal processing unit. Upon tissue deformation, the magnetic transducers attached to the tissue deform jointly, inducing a change in the magnetic field that can be measured wirelessly by the external magnetic sensor / sensor array. Tissue deformation is then recovered from the measured magnetic field signal via the signal processing unit.

1. INTRODUCTION

1.1 Soft Tissue and Its Deformation

In biology, tissue is a cellular organizational level intermediate between cells and a complete organ. It is an aggregation of similar cells from the same origin that carry out a specific function together. Soft tissues refer to the tissues that are not hardened or calcified with the functionality of connecting, supporting, or surrounding other structures and organs of the body. More specifically, soft tissue includes tendons, ligaments, fascia, skin, fibrous tissues, fat, muscles, nerves and blood vessels. Composition of soft tissues includes various cells and the extracellular matrix (ECM), which is a collection of extracellular molecules (collagen, elastin and ground substances for animals) that provide biomechanical and biochemical support to the surrounding cells [1]. Figure 1 shows an illustration of the ECM in relation to epithelial, endothelial and fibroblast cells.

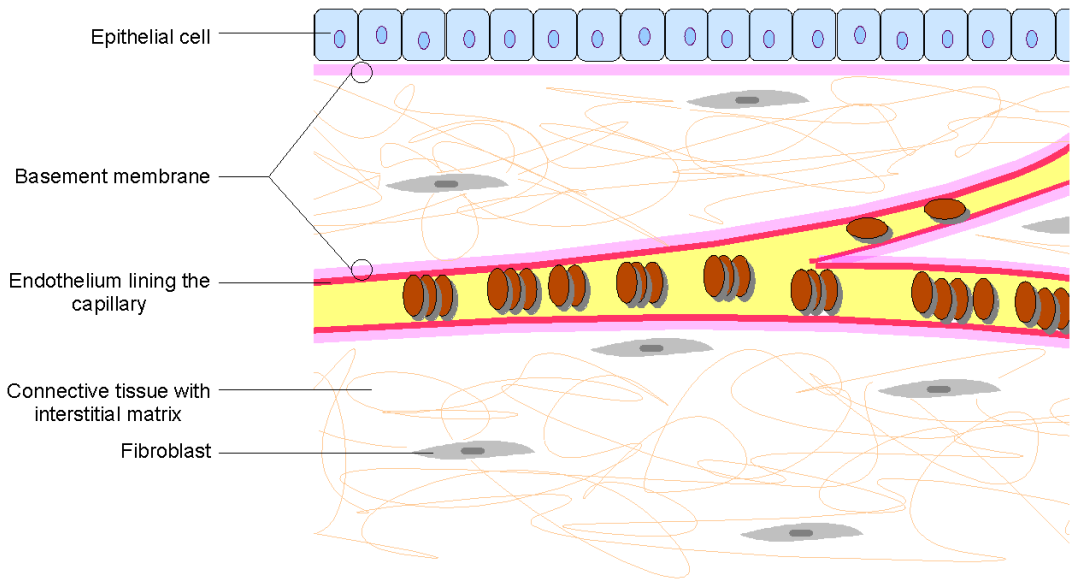

Figure 1. Illustration depicting extracellular matrix in relation to epithelium, endothelium and connective tissue.

Soft tissues deform in innumerable forms, namely elongation/contraction, twist/rotation, bending, and such deformation are essential to every physiological activity: about 10 to 12 muscles

are used during smiling; anterior cross ligament binds tibia and femur together and stabilizes the knee from excessive motion ranges. Mechanical properties of selected human soft tissues are summarized in Table 1 [2], [3].

Table 1. Mechanical properties of selected human soft tissues [2], [3]. Ultimate tensile strain is measured as % elongation beyond initial strain of 100%.

Substance	**Ultimate tensile strength, MPa**	**Ultimate tensile strain, %**
Tendon	53	9
Skin	12.8	90
Cardiac muscle	0.11	37.5
Skeletal muscle	0.11	61
Urinary bladder	0.23	226

Measurement of specific tissue deformation is of great significance to the practical purposes of diagnosis, monitoring, and treatment of medical conditions. For example, many diseases and medical conditions, including pneumonia, tumor, joint or muscle injuries, and hydrocephalus, are diagnosed, evaluated or monitored by examining the images of the targeted tissue of the patient, Figure 2.

Figure 2. Examples of diagnosis, monitoring and treatment of medical conditions through soft tissue deformation measurements. Left: X-ray image shows lung cavitation of a patient with pneumonia; middle: ultrasonic image of a baby inside uterus; right: magnetic resonance imaging (MRI) shows expanded ventricle (dark center region) of a patient with hydrocephalus and shunt placement (bright tube).

Some deformation measurements, especially real-time measurements of soft tissues in animals or phantoms provide insights on complex mechanisms of some diseases and injuries, and therefore boost pathology study and therapy development. For example, real-time deformation measurements of spinal cord or brain tissue during animal study would shed light on the injury mechanism and its subsequent biochemical complications in human being, fueling the development of more effective protective equipment and more injury-specific therapies.

1.2 Current Medical Imaging Techniques for Tissue Deformation Sensing

X-ray radiography, magnetic resonance imaging (MRI) and medical ultrasonography are the three most common medical imaging technologies. Table 2 manifests a summary of their operation principle, target tissue, spatial and temporal resolution [4]–[8].

Table 2. Summary of current medical imaging technologies.

Imaging Technology	**X-ray**	**MRI**	**Ultrasonic**
Operation Principle	Ionizing radiation	Nuclear magnetic resonance	High-frequency acoustic waves
Target Tissue	Bones, some tissues in chest and abdomen	Soft tissues	Soft tissues, bones
Spatial Resolution (μm)	175 (radiography) 500 (CT)	200 (static, 1 Tesla) 130 (static, 7 Tesla) 1500-2000 (real-time)	500 (3 MHz wave)
Temporal Resolution (fps)	N/A (X-ray/CT) 125 (photofluorography)	50 (real-time)	$>10^5$

X-ray radiography, including conventional X-ray, computed tomography (CT) and photofluorography, uses ionizing radiation to generate images of the body. When X-ray beam transverses through the body, a portion of the high-energy photons (5-10 keV) are absorbed or scattered and the remaining photons that pass through are picked up by a monitor or sensor array. The difference of photon attenuation (absorption & scatter) rate across various tissue is responsible for generating image contrast in X-ray radiography. It is useful in detecting the pathology of the

skeletal system as well as in identifying some diseases in soft tissue. Generally, conventional X-ray and CT takes a series of stationary images, implying no temporal resolution, and has a spatial resolution of about 200 μm [4]. Photofluorography, or fluorography, is the real-time version of X-ray radiography that shows the movement of a body part such as the beating of a heart, or the passage of contrast agent in gusto-intestine track, at a sampling rate of 125 fps [5]. As the most common medical imaging technique, X-rays (body, dental, CT scan) combine about 28 million tests in England in 2018 [9], and about 80 million tests in the USA annually. Emergence of portable X-ray devices (Figure 3) provides a convenient option of taking X-rays images at home and thus reduced hospital visits. Despite the prevalence of X-ray imaging and recent progress in home test, it utilizes ionizing radiation that has enough energy to damage the DNA and may elevate a person's lifetime risk of developing cancer. That said, X-ray should be used under discretion to minimize the radiation dose and therefore its potential for chronical deformation sensing is diminished.

Figure 3. Portable X-ray units. Left: Clarox Portable X-ray; right: Nomad Pro 2 handheld X-ray system.

Magnetic resonance imaging (MRI) uses strong (>1 Tesla), static magnetic fields and radiofrequency (RF) waves to make images. Protons hold either parallel or anti-parallel states and a tiny, non-zero net magnetization exists for each infinitesimal proton. When a strong, static magnetic field is present, protons' magnetization is forced to line up with the external magnetic field and such alignment can be perturbed by a pulse of RF electromagnetic wave. Upon removal of the RF pulse wave, the protons have their perturbed magnetization realigned with the external magnetic field (relaxation) and emits an oscillating magnetic field. Such excited magnetic field,

picked up by small receiver coils, are used to estimate proton concentration that varies across different body parts/tissues. Abundant protons in fat and water molecules make MRI more effective for imaging soft tissues such as the brain, ligament or muscle. Static MRI with a 1 Tesla magnetic field has a decent spatial resolution of 200 μm [6] and can reach 130 μm under 7 Tesla field [7]. Real-time MRI, on the other hand, has a compromised spatial resolution of 1.5-2 mm but enables real-time sampling at a rate of 50 fps.

Medical ultrasonic imaging, or ultrasonography, uses acoustic waves whose frequencies are higher than those audible to humans (>20,000 Hz) to view the inner of the body. During imaging, short electrical pulses drive a piezoelectric transducer to vibrate at certain frequency (1-18 MHz), sending acoustic waves to body tissue. A portion of the acoustic waves are reflected whenever they reach an interface between two materials with distinct density, suggesting the detection of tissue or organ boundaries. A receiving transducer converts the reflected wave back to electrical signal and the time and intensity difference between outbound and return waves are used to compute a grayscale image. Because ultrasound images are captured continuously in real-time, they can also show movement of the body's internal tissues. Ultrasonic imaging has a spatial resolution that is proportional to the wave frequency and a penetration depth that is inversely proportional to the wave frequency [8]. It uses portable imaging device and does not use harmful ionizing radiation. Its major limitations include the difficulty of imaging structures behind bones and inside gastro-intestine (GI) tract, and the dependence on a skilled, trained operator.

Review of the current medical imaging technologies suggests that they can generate static or real-time images/tomographies of bones or soft tissues with a hundred-micrometer scale resolution and a sub-hundred Hz sampling rate. However, none of the three technologies is suitable for cases in which more rapid tissue deformation/vibration measurements are required. Moreover, both X-ray and MRI require high energy input that is adverse to miniaturization, making them impractical for chronical tissue deformation sensing. Handheld ultrasonic devices were not commercialized until very recently and their efficacy are yet to be tested in market, Figure 4.

Figure 4. Commercialized handheld ultrasonic devices. Left: Butterfly iQ; right: SonoQue L3.

1.3 Motivation of Deploying Wireless Magnetic Sensing for Soft Tissue Deformation

Wireless magnetic sensing is a favorable option for implantable pressure, strain, or deformation sensing systems as well as for localization and orientation tracking of objects inside the human body [10]–[17], Figure 5. This is mainly because human body has a magnetic permeability very close to that of the air and exerts very little influence on the static (or low frequency) magnetic signal, making it possible to achieve high sensing resolution and accuracy. Also, the static or low frequency magnetic fields are benign to human and impose no concern for chronical measurements. In addition, the magnetic sensing technique is also of higher speed or sampling rate comparing with the common medical imaging techniques reviewed in the previous section. Short distance magnetic sensing systems require minimal power input as they utilize low intensity electromagnetic field or static magnetic field from a permanent magnet, enabling miniaturization into mobile, wearable or implantable devices.

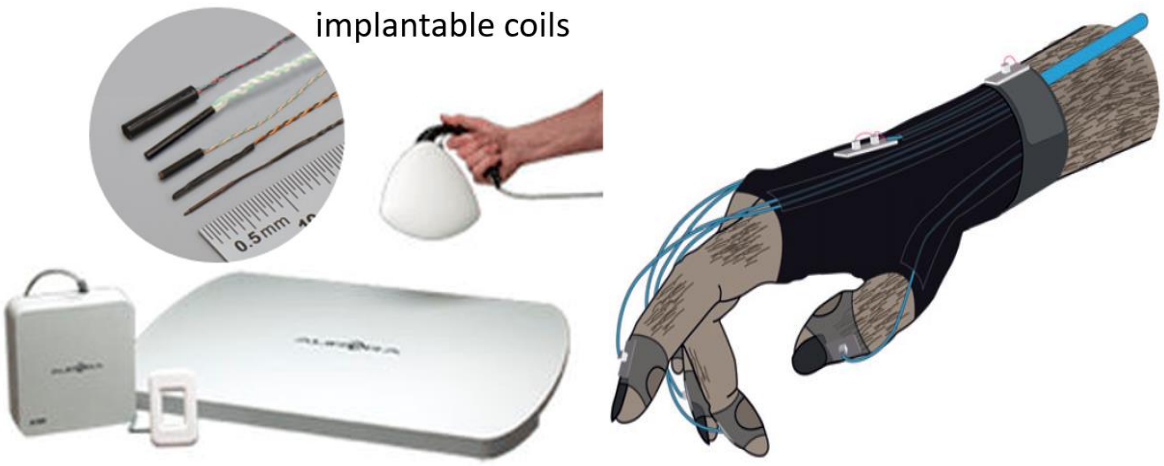

Figure 5. Some applications of magnetic tracking system. Left: NDI Aurora magnetic tracking system capable of tracking catheters and biopsy needles, insight shows the implantable magnetic sensors (coils); right: wired magnetic tracking system for hand motion tracking.

Typically, the magnetic localization and orientation tracking technique uses a magnetic excitation source with one or more magnetic dipoles or coils, generating magnetic signals that can be picked up by the external magnetic coils or sensors. From the detected signals, the system computes the localization (x, y, z) and orientation (roll, yaw, pitch) parameters by applying appropriate algorithms. In some applications, external AC magnetic fields induce a signal from the implanted coil, which is physically connected to a readout device [18]–[20]. However, for tracking objects or medical apparatus inside the human body, e.g., the wireless capsule endoscope and the monitoring of the pill transit [17], [21], [22], the wireless technique, where a readout device picks up signals from an implanted magnetic source wirelessly, is preferable. Figure 6 describes the wired and wireless magnetic tracking technique.

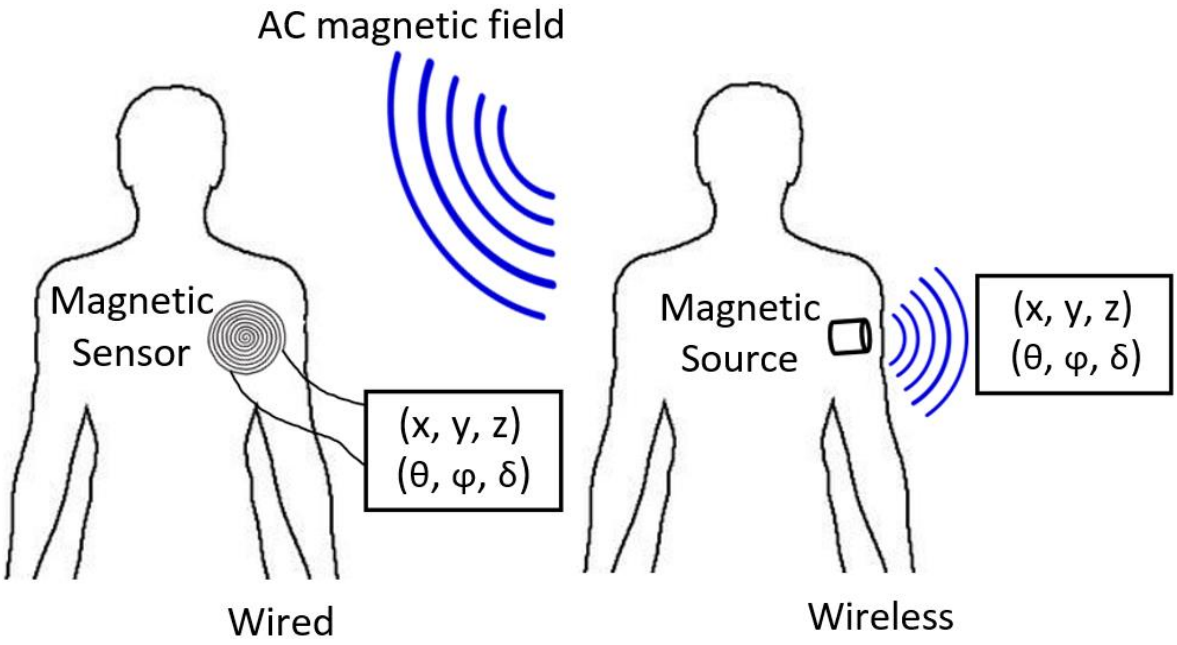

Figure 6. Wired vs. wireless magnetic tracking technique.

Based on the type of the implanted magnetic source, wireless magnetic tracking systems can be classified into two categories: systems with active source or systems with passive source. Systems with active magnetic sources usually contain a power source such as a battery and a field excitation coil that dissipates AC magnetic field. Systems with passive magnetic sources utilize permanent magnets that emit DC magnetic field. Benefiting from signal selection and processing by the frequency and phase of AC magnetic field, systems with active magnetic sources generally have better sensitivity, precision and noise robustness. In addition, systems with active magnetic sources can track multiple magnetic sources simultaneously with one receiver by configuring the magnetic field of these sources into different frequencies and subsequently applying multiple bandpass filters to the acquired signal. Systems with passive magnetic sources better systems with active sources for the void of power consumption, the simplicity of physical design, and the ease of miniaturization. Thus, for applications in which power consumption and space requirements are critical, small permanent magnets can be a more optimal option to serve as the excitation source instead of coils.

Magnetic sensors can date back to ancient Han Dynasty (around 20 BC) in China where lodestone, a naturally magnetized stone of iron, was shaped into compass needle that senses geomagnetic field for navigation. Since then magnetic sensors based on various physics principles

have been developed for applications ranging from navigation, metal detection, to digital storage and so on. Superconducting Quantum Interference Device (SQUID), Hall effect sensors, anisotropic magnetoresistance (AMR) sensors, giant magnetoresistance (GMR) sensors, giant magnetoimpedance (GMI) sensors and tunneling magnetoresistance (TMR) sensors are among the most prevalent magnetic sensor options. Wireless magnetic localization and orientation tracking systems with high precision and accuracy also mandate highly sensitive magnetic sensors. Specifically, the magnetic sensors must be of high sensitivity, wide sensing range and low hysteresis to ensure robust and spurious free magnetic measurements. Some researchers have demonstrated monitoring the transit of a magnetic marker using SQUID technique [21], [23], [24]. However, the SQUID require bulky cooling equipment, and the measurements are usually performed in a magnetically shielded room. It is desirable to find a more convenient magnetic detection technique that can be realized in a normal environment. There have been reports of wireless magnetic tracking systems utilizing arrays of coils [17], Hall effect sensors [25], [26], GMR sensors [27]–[29], and AMR sensors [30]–[32]. Chapter 2.2 details a review of current magnetic sensing techniques and how sensor selection is performed based on specific project requirements.

Polymeric magnets, made from polymer carrier and embedded magnetic micro/nano-particles, possess the traits of flexibility, stretchability and biocompatibility that are desired for biomedical applications of magnetic sensors and actuators [10], [11], [33]–[39]. Polymeric magnets are usually fabricated by mixing liquid pre-polymer such as epoxy [33], polydimethylsiloxane (PDMS) [10], [34]–[39], or silicone [11], with magnetic micro/nano-particles of iron oxide [11], [34], [35] or rear-earth magnets [10], [33], [36]–[39]. The mixture is then shaped and cured using cast-modeling, spin coating, or other microfabrication processes. Unlike the rigid permanent magnets that are sintered from ferrous powder, polymeric magnets have more versatility in terms of shape and magnetic property by selecting various types and mixing ratios of polymer carrier and embedded magnetic particles, and therefore can be more easily customized for specific purposes. It is true that polymeric magnets usually have a much weaker magnetic field comparing to rigid magnets due to the sparser density of ferrous particles. However, recent development of highly sensitive magnetic sensors has enabled precise magnetic sensing of such polymeric magnets.

We propose that, by using wireless magnetic tracking technique featuring polymeric magnets, high speed and chronical measurements of real-time soft tissue deformation can be realized with accuracy. Even though the deformation measurements from such a system are localized deformations and contain less information than the images and tomographies generated by conventional medical imaging from X-ray, MRI or ultrasound, it excels in cases where rapid or chronical deformation measurements are required and could shed some light on pathology studies or enable new means of monitoring medical conditions. The purpose of this research is to explore such possibilities in high speed or chronic deformation monitoring.

To demonstrate the feasibility of wireless magnetic sensing of tissue deformation for applications that require high speed or chronical deformation monitoring, we chose blast induced traumatic brain injury, chronic heart failure and bladder dysfunction as target injuries and diseases. Typical soft tissue deformations in the targeted cases are listed in Table 3. Blast induced traumatic brain injury is widespread among military personnel during combat and its study has been seriously hindered by the lack of means to observe high-speed brain deformation dynamics during blast. Chronic heart failure and bladder dysfunction are two quintessences of inner organ disease where long-term organ volume and deformation monitoring needs to be addressed. Results for a wireless brain deformation sensing system for blast induced traumatic injury (bTBI) featuring a polymeric magnetic disk and results for a wireless, smartphone-aided strain sensing system for heart failure (HF) or bladder dysfunction featuring a stretchable polymeric magnetic band are manifested in Chapter 2 and 3. Background, operation theory, design rationale, sensor selection, localization algorithms, system calibration, and experiment results are covered. Both systems comprise of one or more implantable polymeric magnetic transducer and an external magnetic sensor / sensor array. Upon tissue deformation, the polymeric magnetic transducer attached to the tissue deforms together, inducing a change in the magnetic field that can be measured wirelessly by the external magnetic sensor. Overall, results from abovementioned applications proved that wireless magnetic sensing of tissue deformation is feasible for applications that require high speed or chronic deformation monitoring, providing new insights to bTBI study and promoting more convenient chronic condition monitoring. What's more, we found that the implanted magnetic sensors, when exposed to strong external magnetic field, can also be used for actuation that may enable safer, more convenient and more

comfortable urine management for patients with chronic urinary retention, a common complication of bladder dysfunction.

Table 3. Typical tissue deformations in targeted cases.

Cases	**Normal strain (%)**	**Abnormal strain (%)**	**Strain rate (s^{-1})**
bTBI	< 7 [40]	> 18.8 [41], [42]	36-3000 [43]–[46]
Systolic heart failure	GLS ≤ -16 [47]	GLS ≥ -12 [48]	1-1.4
Diastolic heart failure	GLS ≤ -15.8	GLS > -15.8 [49]	1-1.4
Bladder dysfunction	0-100	> 100	< 0.03

2. A WIRELESS INTRACRANIAL DEFORMATION SENSING SYSTEM FOR BLAST-INDUCED TRAUMATIC INJURY (BTBI)[1]

2.1 Background

2.1.1 Blast physics and blast-induced traumatic injury

Blast wave, or shockwave, is the increase in air pressure and flow resulting from the release of a large amount of energy in a very small, localized space. A blast wave can be considered as a layer of highly compressed air volume propagating outward and is very different from acoustic waves where air molecules pass mechanical vibrations forward. An interesting fact of a blast wave is that it travels supersonically (about 500 m/s), with a speed roughly 1.5× that of the sound in the air. Explosive detonation is a common source of shockwaves.

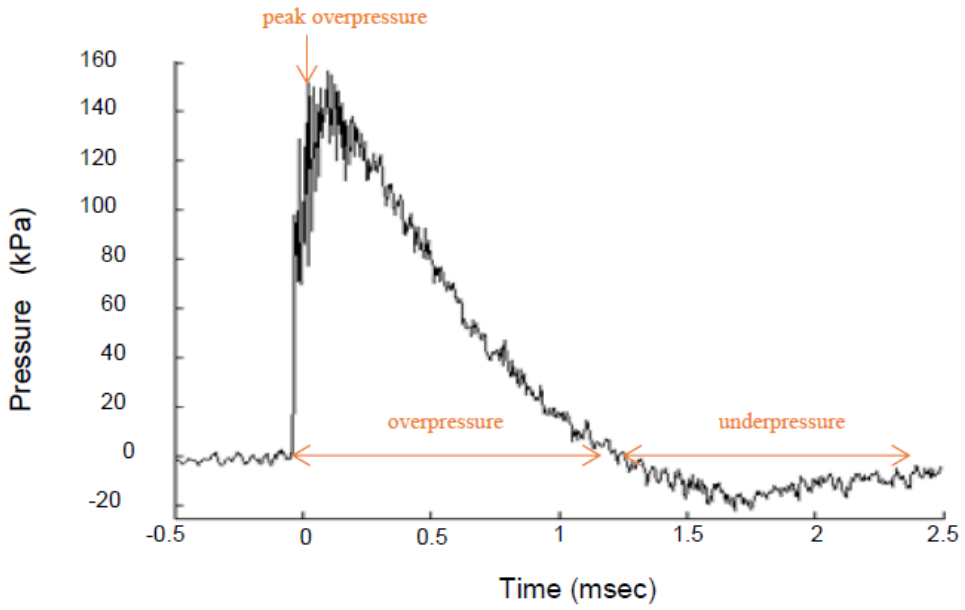

Figure 7. A representative free-field blast pressure profile illustrating the Friedlander waveform, characterized by its abrupt but dramatic pressure elevation to the 'peak overpressure', followed by an exponential decay in pressure during the 'overpressure' period, and closed by a negative pressure change termed as the 'underpressure' before normalization to ambient pressure. The whole blast wave lasts for approximately 2.5 milliseconds.

[1] Part of this chapter was published in 'A Wireless Intracranial Deformation Sensing System for Blast-Induced Traumatic Brain Injury' in *Scientific Reports* by S. Song, N. Race, A. Kim, T. Zhang, R. Shi, and B. Ziaie [11].

When traveling unimpeded in an open space, the pressure profile of a blast wave consists of positive and negative pressure surges, characterized as the Friedlander waveform. A blast wave's arrival is marked by an abrupt, almost instantaneous and dramatic elevation in pressure to its maximum value, i.e. the 'peak overpressure'. Once the maximum overpressure is reached, pressure decays exponentially over time. The time interval between the wave's arrival and its intersection with the horizontal zero-pressure axis is termed the 'overpressure duration.' Following the compressive overpressure, a tensile 'underpressure' period precedes the recovery to ambient pressure (0 kPa relative pressure) [50]. Figure 7 shows a representative pressure profile of a blast wave in free field.

Typically, the duration of the whole blast wave ranges from 2.5 milliseconds to 10 milliseconds for conventional high-explosives [45]. The peak overpressure decays drastically as the distance from blast source increases.

Contrary to the ideal free-field case, blast waves usually propagate with obstacles or barriers along the way. When the blast wave encounters an object, part of the wave is reflected while another part penetrates through. Parts of the wave that is not in contact with the obstacle continues to propagate freely. Figure 8 illustrates the wave reflection/transmission mechanism including effects from the ground surface and buildings, as well as the intact free-field propagation [51]. Depending on the amount of confinement surrounding the blast, the intensity of waves reflected from a solid surface can be 1× to 20× greater than that of the incident waves, leading to a remarkably stronger pressure experienced.

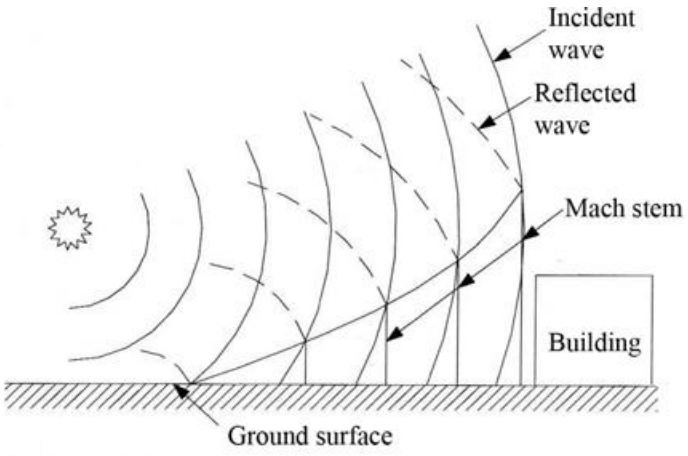

Figure 8. Illustration of blast wave propagation with objects in path. Part of the wave that hits the ground surface or building are reflected or transmitted. Part of the wave not in contact with the object remains free-field propagation [51].

High explosives, including bombs, grenades, landmines, improvised 'roadside' explosives, etc., are the common sources of blast wave. Generation of high-energy blast waves is often accompanied by other types of energy and substance dissipation such as thermo energy (extreme heat), kinetic energy (shrapnel) and chemical release (toxic gas), resulting in primary, secondary, tertiary, and quaternary blast-related injuries. The definition of each injury component is summarized in Table 4.

Table 4. Components of blast-induced injury

Primary	Direct interaction between the body and the blast wave
Secondary	Projectile contact with and penetration of the body
Tertiary	Resultant whole-body acceleration, deceleration, and blunt impacts
Quaternary	Thermal, chemical, and other injuries associated with the blast event

Secondary, tertiary, and quaternary injury modalities are prevalent in moderate and severe blast injuries in which individuals are located in close proximity to an explosion [45], [52]. Acute symptoms are apparent in these cases, calling for immediate medical evaluation, monitoring, and treatment [52]. Primary blast injury, particularly in its isolated form where individuals are situated sufficiently distanced from the site of explosion so that all other blast injury modalities are avoided, is of great interest for recent research studies [45], [52], [53]. Such injury, termed as the mild b-TBI, can lead to long-term mental health and/or neurodegenerative sequelae [54]–[59]. The heterogeneity nature of human tissues further complicates how blast wave interact with our body, leading to highly variating tissue damage mechanisms for b-TBI and, more specifically, mild b-TBI.

2.1.2 Blast-induced traumatic brain Injury: epidemiology and existing problems

With the continual advancement and lowering cost of small explosives, particularly improvised explosive devices, blast-induced traumatic brain injury (bTBI), already one of the most significant wounds throughout Operation Enduring Freedom (OEF) and Operation Iraqi Freedom (OIF), has become increasingly prevalent. Approximately 167,000 bTBI cases have been documented during OEF and OIF deployments alone [60], [61], and the true number of bTBI

incidents is expected to be even higher due to under-reporting and the fact that they can also occur during training exercises [61]. Post-bTBI consequences are dire, ranging from neurodegenerative diseases such as chronic traumatic encephalopathy to neuropsychiatric alterations such as depression, anxiety, and more [54], [57]. Many of these consequences originate from mild bTBI which occurs from blasts with such a low intensity that no acute symptoms can be observed. Such sub-threshold damage may not become evident until weeks, if not months, after the initial injury and are impossible to diagnose clinically. These risks pose a substantial public health burden upon military members' return to civilian life, as the conditions are generally chronic and involve lengthy and costly treatment courses both in terms of dollars and quality of life. To pursue targeted innovation of new preventative, diagnostic, and therapeutic measures, we must first develop greater understanding of bTBI pathogenesis, its initiating mechanical events, and the links between blast-induced damage and subsequent neuropathologies.

Blast waves' ability to cause primary injury to brain has been debated without a consensus in terms of whether the blast wave can propagate through the skull, or if the injury can be prevented or mitigated by a neck fixation [62]. Previously it was long been thought that the skull served as a protective 'helmet' capable of preventing blast waves from injuring the brain; however, growing evidence now supports the idea that the brain is vulnerable to blast-induced injury at thresholds below those of other organs such as heart, liver, or kidney [45], [63], [64]. Although it has been demonstrated that exposures to blast waves compromise the blood-brain barrier and cause both dynamic short-term and sustained long term intracranial pressure rises hypothesized to lead to axonal injuries, knowledge regarding the pathobiological mechanisms of primary bTBI is limited [65]–[67]. This can largely be attributed to the experimental challenges of studying the brain deformation caused by blast waves in real time due to the presence of the skull, and high temporal and spatial resolution requirements [62], [65], [68]–[70]. Such requirements render traditional imaging methods inapplicable to study brain dynamics in the primary bTBI. Alternatives are simulations or controlled experimental models to mimic the actual injury. Simulation models to date have suffered from a lack of experimental data to validate the results [65], [71] as few experimental bTBI biomechanics investigations have been conducted in animal models.

To address such issue in conducting bTBI, especially mild bTBI, experiments and boost research on bTBI biomechanics, we present a sensor system capable of real-time *in vivo* measurements of the intracranial brain deformation using an implantable elastomeric polymeric

magnet and three external giant magnetoresistance sensors (GMR). The sensor system was characterized, validated, and applied to three different experimental models (3D-printed skull with agarose gel, dead rats, and live rats) to measure intracranial brain deformations during blast waves generated via an open-ended shock tube system.

2.2 Design Rationale

2.2.1 Operation theory and system requirements

By narrow definitions, sensors are devices that can detect or quantify changes of certain parameter and convert such dynamics into readable and analyzable analog electrical signals for subsequent analysis. Common parameters to be sensed include mechanical, electrical, chemical, optical, thermal, magnetic, pressure, radiation, etc. Sensing systems integrate one or more sensors from one or more sensing categories with additional components for functionalities of noise reduction, analog-to-digital conversion (ADC), signal processing, sensor control and data storage. Sensing systems need to be specifically designed for the intended application and a thorough understanding/analysis of the underlying problem is of significant importance.

In my opinion, the first few questions for designing sensing systems has always been:

- What is our system trying to sense?
- How should the system sense it?
- Under what conditions will the sensing system usually operate?

These questions are explained and answered one-by-one in the following paragraphs.

What is our system trying to sense? The intended application is to record the high frequency yet minor biomechanical dynamics of brain tissue deformation during mild b-TBI events in animal experiments. Prior works attempted to extrapolate such biomechanical behavior indirectly through other physical parameters. Sundaramurthy et al. [72] and Cavko et al. [73] gained insights on brain deformation by measuring air pressure or acceleration at external (nose tip) and internal (brain surface & thoracic cavity) sites of a rat. Wired pressure probes and accelerometers are inserted via drilled holes on the skull and internal pressure variation as results of diverse incident blast pressure and relative position/orientation of the rat with respect to the blast is observed. Despite the high frequency intracranial brain dynamics are monitored in real-time, substantial gap exists between

indirect pressure or acceleration observations and the real brain tissue deformation. In addition, holes drilled through the animal skulls compromises the hermiticity of the skull-brain environment, leading to lesser skull protection than that in reality. In aware of the limitations from previous work, we aim to design a sensing system that can record *intracranial brain tissue deformation directly*, *wirelessly*, and in *real-time*.

How should the system sense it? At least one type of the sensing techniques is to be selected from the common sensors. Mechanical sensors can convert tissue deformation straightly into electrical signals. In spite of convenient deformation sensing, acquired electrical signals require wired or wireless data transmission, which demands either a cable through the skull for wired data transmission or a wireless data transmission unit with an active power source. The opaque skull denies any optical means of observation to the brain tissue without an open crack and it undermines the integrity of the skull if a piece of the bone is replaced by transparent material for visual access. Electrical, thermal, or chemical sensors are not applicable to deformation sensing. Magnetic sensing, particularly the 'wireless magnetic tracking technique' described in Section 1.3 seems to be a feasible candidate. With a piece of magnet attached to the brain tissue, any tissue deformation will move the magnet, inducing a change in the magnetic field that can be measured wirelessly outside the skull. Without the presence of other ferromagnetic material, there is no delay or distortion on the motion-induced magnetic field dynamics so that it can faithfully represent the brain tissue deformation as long as a magnetic sensor with sufficient sampling rate is used. No electrical signal is picked up internal of the skull so that neither wired nor wireless data transmission module needs to be placed. Only a passive piece of magnet gets implanted, meeting our requirements to measure intracranial tissue deformation directly, wirelessly and in real-time. Detailed explanation of operation theory is described in the following paragraphs.

The magnitude of magnetic flux density $\vec{\boldsymbol{B}}$ inside or over the surface of a magnet, which is directly proportional to the external magnetic field *H* and material magnetization *M*, is:

$$\left|\vec{\boldsymbol{B}}\right| = \mu_0(H + M) = \mu_0\mu_r H \qquad (1)$$

where μ_0 is the vacuum magnetic permeability and μ_r is the relative magnetic permeability of the material. Under zero external magnetic field *H*, the resultant magnetic flux density is:

$$\left|\vec{\boldsymbol{B}}\right|(H = 0) = \mu_0 M = B_r \qquad (2)$$

where B_r is the remaining material magnetization when $H = 0$, termed as the remanence.

In vector notation, the magnetic field outside of a magnetic dipole (a zero-volume point with both north and south poles) with magnetic dipole moment $\vec{\boldsymbol{m}}$ can be expressed as the negative gradient of a magnetostatic potential Φ_m:

$$\vec{\boldsymbol{B}}(\vec{\boldsymbol{r}}) = -\nabla\Phi_m(\vec{\boldsymbol{r}}) = -\nabla\frac{\mu_0}{4\pi}\vec{\boldsymbol{m}}\cdot\vec{\boldsymbol{r}}/|\vec{\boldsymbol{r}}|^3 \quad (3)$$

where $\vec{\boldsymbol{r}}$ is the vector between the magnetic dipole and the point in space.

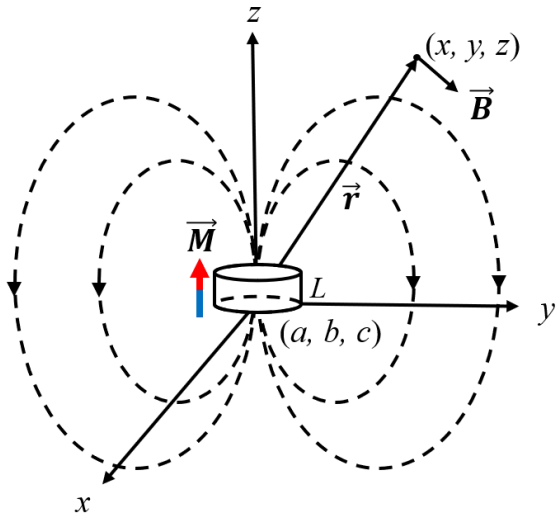

Figure 9. Illustration of magnetic field induced by a disk magnet.

Shown in , the magnetic flux B induced from a magnetic disk at (a, b, c), measured from point (x, y, z) can be calculated by integrating magnetic flux density of dipoles over the entire volume of the cylinder, with magnetic dipole moment $\vec{\boldsymbol{m}}$ replaced by magnetization density $\vec{\boldsymbol{M}}$ ($\vec{\boldsymbol{m}} = \int \vec{\boldsymbol{M}}\, dxdydz$):

$$\vec{\boldsymbol{B}} = \int_0^L \int_{-\sqrt{\sigma^2-x^2}}^{\sqrt{\sigma^2-x^2}} \int_{-\sigma}^{\sigma} -\nabla\frac{\mu_0}{4\pi}\vec{\boldsymbol{M}}\cdot\langle x-a, y-b, z-c\rangle/[(x-a)^2+(y-b)^2+(z-c)^2]^{3/2}dxdydz$$

$$= B_x\vec{\boldsymbol{\imath}} + B_y\vec{\boldsymbol{\jmath}} + B_z\vec{\boldsymbol{k}} = \frac{\mu_r\mu_0\pi\sigma^2 L}{4\pi}\left(\frac{3(\vec{\boldsymbol{m}}\cdot\vec{\boldsymbol{r}})\vec{\boldsymbol{r}}}{|\vec{\boldsymbol{r}}|^5} - \frac{\vec{\boldsymbol{m}}}{|\vec{\boldsymbol{r}}|^3}\right) \quad (4)$$

where B_x, B_y, and B_z are the three components of the magnetic flux density in the position of measurement; L is the length of σ is the radius of the cylindrical magnet; $\vec{\boldsymbol{M}}$ is a vector defining

the direction and magnitude of the magnet's magnetization; $\vec{r}$ is a vector defined as <*x-a*, *y-b*, *z-c*> and $|\vec{r}|$ is its magnitude. This is the key principle that enables wireless magnetic localization and tracking of a magnet. As part of an electromagnetic wave, the change in magnetic field propagates at the speed of light (approximately 3×10^{8} m/s. At a sensing distance comparable to the thickness of rat skull (0.5 – 1.5 mm) [74], the amount of latency in the response between location and magnetic field is around 3.5×10^{-12} s. This delay is minimal compared with the application's desired temporal resolution (1/(6000 s^{-1}) or 1.7×10^{-4} s, twice of a high bTBI strain rate of 3000 s^{-1} [75] by Nyquist sampling theorem) and thus can be ignored in our sensing system.

Before a blast experiment, a polymeric magnet is implanted on the surface of the brain, either outside of the dura mater or inside of it. When the brain deforms by the blast wave, the implanted polymeric magnet follows the movement of the brain. Such displacement creates a dynamic magnetic field, which is detectable via a GMR sensor array fixed to the surface of the skull. The operation mechanism of the proposed wireless magnetic intracranial deformation sensing system is illustrated in Figure 10.

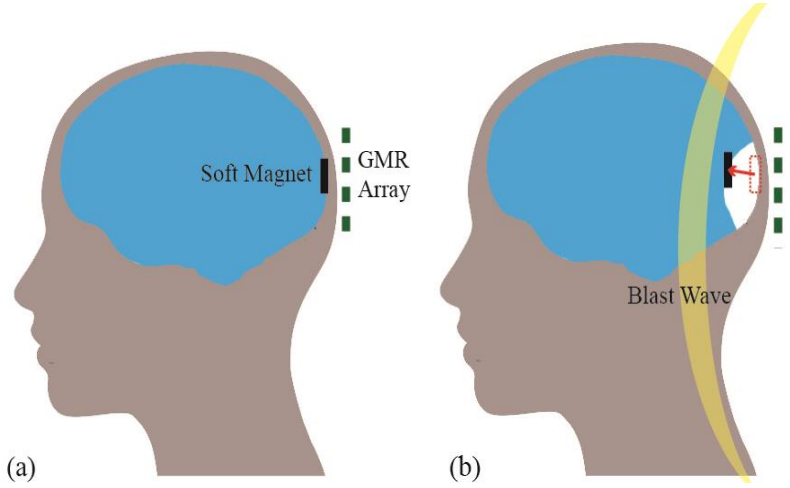

Figure 10. Deformation tracking system (a) at rest and (b) during a blast.

Signals from the GMR sensor array is then processed and goes through localization algorithms so that the corresponding displacement of the polymeric magnet, which is equivalent to the localized deformation of the brain tissue, is computed.

Under what conditions will the sensing system usually operate? We plan to measure brain tissue deformation of animals during a mild blast experiment. Recent research studies have shifted toward the use of open-ended shock tubes for their advantage of inducing primary shock overpressures free of complex wave reflections or tailwinds [45], [76]. The animal will be placed within 30 cm of tube opening and thus the external magnetic sensor must be compact so that it will not act as an obstacle or shield that hinders blast wave propagation. On the other hand, the part of the sensing system that is exposed to shock wave must survive the experiment without breaking down or introducing any motion-related noise and artefact.

As for the implanted magnet, there are four major concerns: strong magnetic field intensity, low material stiffness, moderate material density and good in-vivo stability/biocompatibility. The magnetic field strength of implanted magnet decays rapidly in a reverse cubic law and the motion-induced magnetic field gradient must be detectable by the external magnetic sensor which is separated by the animal's skull and, possibly, an air gap. In addition, stronger magnetic field boosts the signal-to-noise ratio (SNR) of the sensing system, enhancing the system's the robustness, spatial precision and accuracy of deformation measurement. Besides, the magnetic source and the magnetic sensor together promote the SNR and performance of the sensing system so that ideally the selected sensor should be as sensitive as possible. The implanted magnet needs to have low material stiffness which, in the most optimal case, matches the toughness of the brain tissue. With a brittle magnet implanted, it may penetrate the brain tissue during a blast event, bringing in irrelevant brain damage that pollutes experiment results. Under similar mentality, the density of the magnet must be comparable to that of the brain tissue so that the magnet imposes minimal interference during blast induced tissue deformation. Otherwise, the density mismatch between the magnet and the brain tissue transforms their combination into an approximation of spring-mass system where harmonic oscillation starts to take place. Lastly, some live animal experiments, especially those involving post-blast behavior evaluations or long-term injury assessments, are anticipated to last for weeks and the implanted magnets must stay benignly inside the animal's body. What's more, the implanted magnet should maintain stable magnetic field strength in-vivo throughout the experiment period so that the sensing system can perform consistent deformation measurements without repeated calibration.

Overall requirements for the wireless intracranial deformation sensing system, as well as their corresponding target specifications are summarized in Table 5. Note that the target specification are preliminary numbers.

Table 5. Summary of wireless intracranial deformation sensing system requirements and target specifications

Requirements	Component	Target specifications
Temporal resolution	System	≥ 100 kHz or ≤ 0.01 ms [77]
Spatial resolution	System	Order of micrometers
Sensing range	System	> 0.5 mm [74]
Structure integrity	System	Should survive blast experiments
Magnet stiffness	Magnet	Close to that of brain tissue (white matter 1.895 kPa, gray matter 1.389 kPa[78]; 1-40 kPa [46], [71])
Magnet density	Magnet	Close to that of brain tissue (1.0107 g/cm^3) [79]
Magnetic stability	Magnet	Magnetic field decay < 10% in vivo for > 20 days
Biocompatibility	Magnet	Biocompatible material or hermetic biocompatible coating

Bearing sensing system requirements and target performance specifications in mind, we proceed to sensor selection.

2.2.2 Magnetic sensing physics and sensor selection

To select the appropriate magnetic sensor for the intracranial tissue deformation sensor, magnetic sensors based on various principles, including superconducting quantum interference device (SQUID), Hall effect, anisotropic magnetoresistance (AMR), giant magnetoresistance (GMR), giant magnetoimpedance (GMI), and tunneling magnetoresistance (TMR) were evaluated for feasibility. Operation theories of investigated magnetic sensors are briefly surveyed below.

Superconducting quantum interference device (SQUID) SQUID is a very sensitive magnetometer for measuring extremely small magnetic fields using superconducting loops. In its

simplest form, a SQUID sensor comprises of a superconducting loop with two junctions (Josephson junctions) where current flows through the two branches of the loop equally in absence of external magnetic field. Once a small magnetic field is applied to the superconducting loop, a screen current I_s starts to circulate around the loop that induces a magnetic field cancelling the applied external magnetic field. This screen current, proportional to the applied magnetic field, is parallel to the current in one branch but antiparallel to that in the other branch. The magnetic flux that penetrates the superconducting loop is quantized into an integer multiple of Φ_0 and I_s starts to decrease if the external flux exceeds $\Phi_0/2$. As a result, the current fluctuates periodically with maximum and minimum at flux = $(n+1/2)\ \Phi_0$ and flux = $n\Phi_0$ where n are non-negative integers. Plots explaining the dynamics between current, voltage and applied magnetic flux is shown in Figure 11. Thus, the applied magnetic field can be calculated by counting the number of periods the loop current fluctuated and multiply this count by the flux quantum Φ_0. A remarkable sensitivity of 5×10^{-18} T can be achieved with SQUID. Despite the astonishingly good sensitivity, the SQUID measurement assumes perfect flux quantization that only holds true for big loops with high inductance. Equipped with a cooling system that keeps the measurement loop in superconducting, the entire SQUID system is usually very bulky and energy consuming.

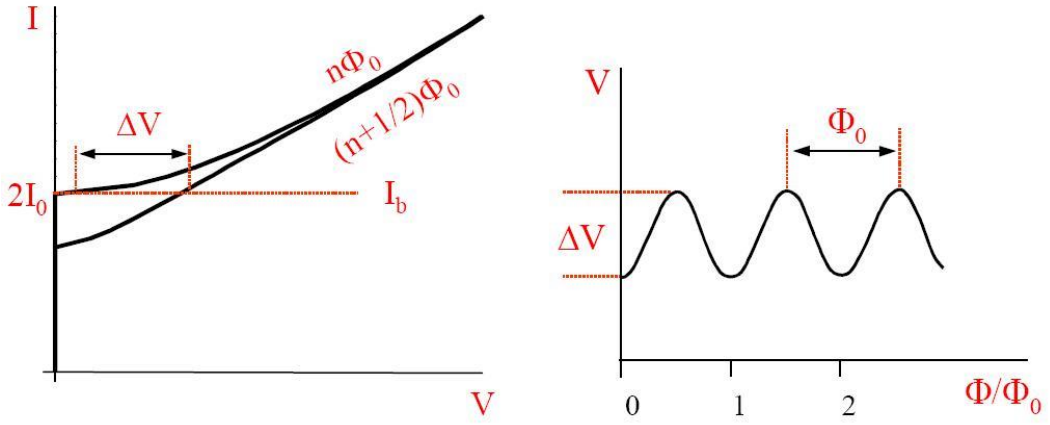

Figure 11. Plots explaining the dynamics between current, voltage and applied magnetic flux.

Hall effect Hall effect utilizes the nature of electron flow in a conductor. When an external magnetic field is applied perpendicularly on a rectangular planar conductor where current flows along the long edge, Lorentz forces are exerted on the electrons and they start drifting to one of

the shorter edges. Electrons accumulated on the short edge builds up an electric potential and an equilibrium is reached when the electro-static force from the equilibrium Hall voltage V_H balances the Lorentz force so that no more electrons are drifted. Thus, the magnitude of external magnetic field is calculated from V_H as:

$$B_z = \frac{nteV_H}{I} \quad (5)$$

where I is the current flowing through the conductor; n is the charge carrier density of the conductor; t is the thickness of the conductor and e is the charge of each electron.

Anisotropic magnetoresistance (AMR) Anisotropic magnetoresistance, discovered by Lord Kelvin in mid-nineteenth century, is the oldest type of magnetic sensing principle men ever found. It is the change in electrical conductivity of spontaneously magnetized materials with respect to the relative direction of the electrical current and the magnetization. The conductor's resistivity is at its minimum value when the current and the magnetization are aligned, at its maximum when they are perpendicular to each other, and varies at a $\cos^2$ rate in between, Figure 12. The effect arises from the interaction between magnetization and the magnetic spin of spontaneously magnetized atoms. In spontaneously magnetized material, atoms' magnetization is self-aligned in a uniform direction in local regions named magnetic domains. The final magnetization direction has a strong geometric dependency that tries to minimize the overall entropy of the material and generally, the longer dimension of a piece of such material is favored by spontaneous magnetization.

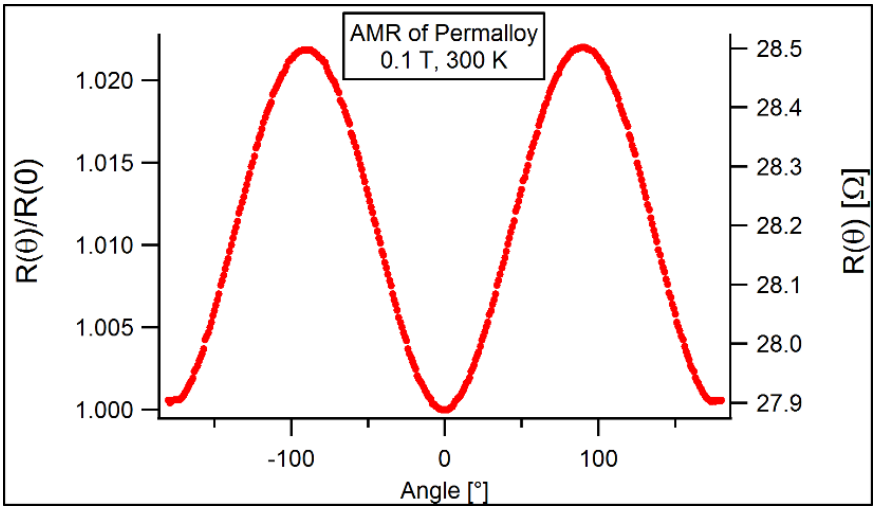

Figure 12. Anisotropic magnetoresistance: resistance of a thin Permalloy film as a function of the angle of an external magnetic field.

Giant magnetoresistance (GMR) Discovered in 1988, the Nobel Prize-winning discovery of giant magnetoresistance shows a substantial quantum magnetoresistance effect in alternating ferromagnetic and non-magnetic conductive multilayer structure. Similar to the phenomenon of AMR, resistance of a GMR device is a function of the angle between ferromagnetic material's magnetization and the external magnetic field. Spin-dependent scattering attributes to the GMR phenomena. In ferromagnetic materials such as cobalt, iron, scattering is strong for electrons with spin antiparallel to the magnetization direction and is weak for electrons with spin parallel to the magnetization direction. Strong electron scattering reduces the mean free path for an electron to travel before it scatters away and as a result, increase the resistance. Figure 13 illustrates a thin layer (~5 nm) of non-magnetic conductor, normally copper, sandwiched between two ferromagnetic layers who have parallel or antiparallel magnetization directions while electric current flows in the material's plane [80]. The top layer is magnetically pinned so that its magnetization remains unchanged under external magnetic field. The bottom layer is a free layer whose magnetization aligns with external field. Since the copper layer is only a few nanometers thick, electrons flowing through the copper layer will drift into the ferromagnetic layer, whose electron scattering property varies with magnetization direction. At zero external magnetic field, the top and bottom layer's magnetization are aligned in parallel, weakening electron scattering and lowering the GMR unit's resistance. Upon applying an external magnetic field, the bottom layer

aligns its magnetization with the field and becomes antiparallel to that of the top layer, enhancing electron scattering and increasing the resistance.

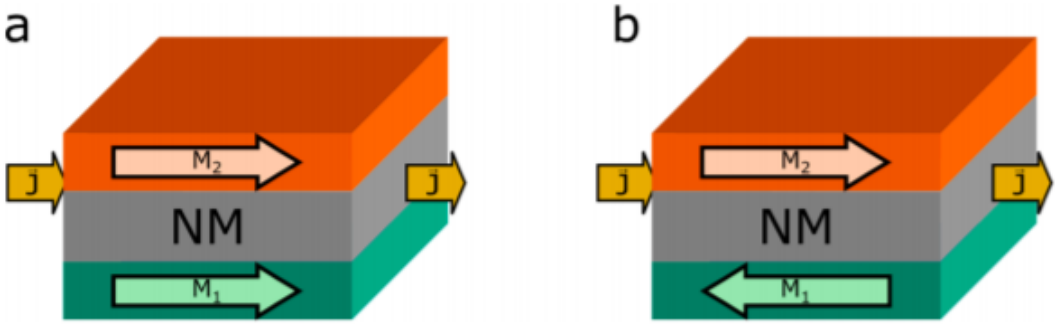

Figure 13. Illustration of GMR structure in a) parallel magnetization where the resistance is at its lowest and b) antiparallel magnetization where the resistance is at its highest.

Giant magnetoimpedance (GMI) Apart from other magnetoresistance phenomena, where the resistance changes in response to applied magnetic field, GMI is a magnetoimpedance phenomenon where the complex impedance of a material changes with magnetic field. GMI is backed by the skin effect of conductors. It can be easily explained if we think conductor as a tube and current as water flowing through. When direct current flows through a piece of conductor, electrons will fill up the entire conductor to flow forward. However alternative current may only fill up to a certain depth inside an electrical conductor just like water flowing through a smaller tube. This maximum depth AC current can flow in a conductor, called the skin depth, is inverse proportional to the square root of the product of the conductor's magnetic permeability and the frequency of the AC current. explains how skin depth and impedance vary with AC current frequency.

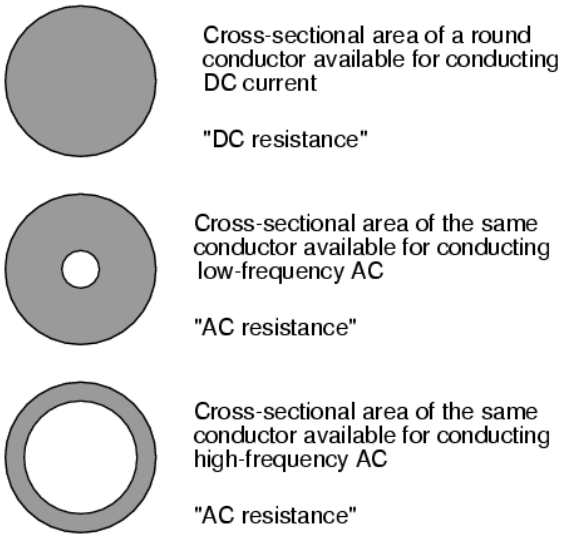

Figure 14. Explanation of skin effect: how skin depth and impedance vary with AC current frequency.

The magnetic permeability of some material changes drastically with external magnetic field, leading to a highly sensitive magnetoimpedance response.

Tunneling magnetoresistance (TMR) TMR is a magnetoresistive effect that occurs in a magnetic tunnel junction (MTJ) at quantum level. In short words it is an electron tunneling effect controlled by external magnetic field. MTJ has a structure consisting of two ferromagnetic layers sandwiching a thin insulator, whose thickness is typically a few nanometers. It is noteworthy that TMR has similar structure as GMR except for having insulated middle layer instead of conductive middle layer in GMR. One of the two ferromagnetic layers has pinned magnetization while that of the other layer aligns freely with external magnetic field. Under zero magnetic field, the magnetization of the two layers are in opposite directions and electrons are less likely to tunnel through, increasing the MTJ's resistance. When external magnetic field aligns the magnetization of two layers to parallel direction, electrons are more likely to tunnel through, lowering the MTJ's resistance.

The ideal magnetic sensor for the wireless intracranial tissue deformation sensing application should possess features of compact size, high sensitivity, high signal-to-noise ratio (SNR), high sampling rate and low magnetic hysteresis. We investigated the commercial magnetic sensors based on various magnetic sensing techniques and some key properties of candidate magnetic sensors are summarized in Table 6. Note that the TMR sensor, Crocus CT100, was not

available until 2020. For sensors with analog-to-digital converter (ADC) integrated in chip, they output digital readings already and their sampling rates depend on the type of ADC used and cannot be altered. Sensors without built-in ADCs generate analog outputs, which can be sampled at various rates based on application requirement.

Table 6. Summary of key properties of candidate commercial magnetic sensors based on various magnetic sensing techniques. The TMR sensor, Murata CT100, was not available until 2020.

Technique	Sensor model	Sensitivity	Linear Range	Sampling rate (Hz)
Hall effect	Honeywell SS494B	0.05 mV/μT	$\pm 4.2\times10^4$ μT	-
AMR	Kohden KG1302-01	0.0097 mV/μT at 5V	±3100 μT	-
TMR	Murata CT100*	1.35 mV/μT at 3V	$\pm 2\times10^4$ μT	-
GMR	NVE AAH002-02E	0.75 mV/μT at 5V	±300 μT	-
GMI	Aichi Steel AMI306R	6 LSB/μT	±1200 μT	1000
SQUID	Quantum Design MPMS®3	2×10^5 LSB/μT	±7 T	1000

* Not available until 2020.

SQUID sensors require bulky cooling components and would not be feasible for mounting outside of the skull. Both Hall effect and AMR sensors have relatively low sensitivity. GMR sensors exhibit good sensitivity while GMI sensors are the most sensitive type. However, the GMR sensor excels because it provides the best sensitivity among sensors with analog output, allowing the concatenation of customized analog-to-digital converter (ADC) with high sampling rate which is a critical requirement for real-time, high frequency deformation sensing during a blast event. In the end, we selected GMR sensor chips (AAH002-02E) from NVE Corporation. It uses SOIC8 package with dimensions of 5×3.85×0.5 mm and 8 pins (4 used). Key specifications, magnetic response curve and chip architecture are shown in Table 7 and Figure 15.

Table 7. Key specifications of NVE AAH002-02E GMR sensor [81].

Linear Range	Saturation	Sensitivity	Neutral resistance
3-300 μT	600 μT	0.15 mV/V·μT	2 kΩ

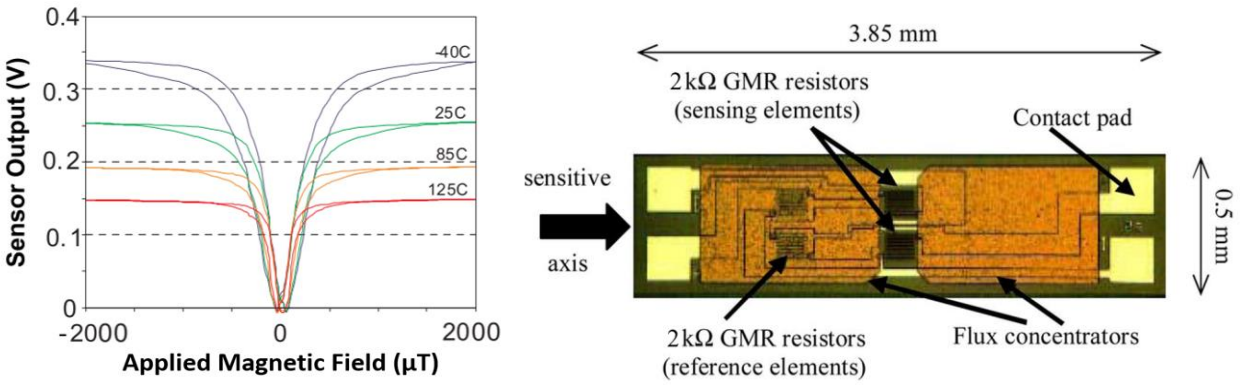

Figure 15. Magnetic field response curve with 5V supply voltage (left) and internal architecture of NVE AAH002-02E GMR sensor (right) [81]. Horizontal arrow in right indicates the axis of magnetic sensitivity.

Each sensor chip consists of 4 GMR serpentine resistor units connected in a Wheatstone bridge configuration. Two diagonal resistor units are magnetically shielded so that they act as reference resistors. The other two units are wrapped with high permeability material that works as a flux concentrator, enhancing the sensor's sensitivity to the applied magnetic field. Compared to a simple voltage divider, the Wheatstone bridge configuration further amplifies the voltage response with respect to the magnetic field.

The only disadvantage of the selected GMR sensor is that it measures the magnitude of the magnetic field along a single axis of sensitivity instead of the field's 3-axial components. The direction of sensitivity is in the plane of the sensor package and its two modes of magnetic sensing are illustrated in Figure 16. Since magnetic localization is a 3 degree-of-freedom (x, y, z) problem in our case, a minimum of three sensors are required to provide adequate data.

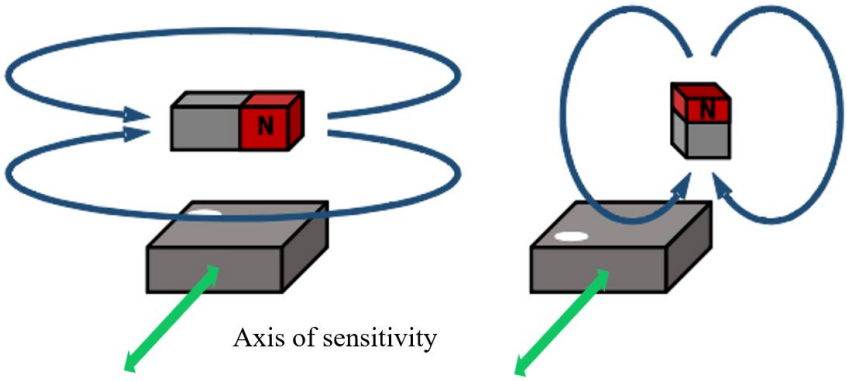

Figure 16. Sensing modes of NVE AAH002-02E GMR sensor: magnet parallel to plane (left) and magnet perpendicular to plane (right) [81]. The green arrow indicates the sensor's direction of sensitivity and the sensor output is indifferent of magnetic polarity (omni-polar).

2.2.3 Polymer magnet design and material selection

Polymer magnets are non-rigid, flexible magnets made from polymer substrate with embedded magnetic microparticles or nanoparticles. Polymer is formed by assembling repeating molecular polymer subunits (prepolymer) into chains and webs during crosslinking process. Countless tiny gaps and holes exist between the polymer chains and webs, providing spaces for micro/nanoparticle impurities to reside. If magnetic micro/nanoparticles are mixed uniformly with liquid prepolymer, they will be trapped and locked in place by the chains and webs formed in polymer, resulting in flexible polymer possessing the magnetic property of embedded magnetic particles. Since the magnetic particles in polymer magnet are separated and thus cannot form contiguous magnetic domains that promote spontaneous magnetization, forced magnetization (polarization) by external magnetic field is typically required.

One of the most noteworthy advantages of polymer magnet is its flexibility in design and fabrication. Liquid prepolymers carrying magnetic microparticles can be shaped into various contours and volumes by casting into molds with different shapes. By selecting different types of polymer substrates and magnetic particles and by varying the particle doping ratio or the polymer crosslink temperature, researchers can achieve distinct mechanical and magnetic properties on polymer magnets that cater to needs of the specific application. One typical application of the polymer magnets is the fridge magnet where a small polymer magnet sheet with chosen shapes is attached to a piece of ornament such as a picture or a figurine. Lagorce et al. [33] fabricated magnetic microactuators based on polymer magnets.

Common magnetic materials include iron (Fe), iron oxide (Fe_2O_3), cobalt (Co), manganese iron oxide ($MnOFe_2O_3$), strontium ferrite ($SrFe_{12}O_{19}$), barium ferrite ($BaFe_{12}O_{19}$) and neodymium iron boron (NdFeB). Only iron and iron oxide are known to be biocompatible while strontium ferrite is reported as 'not harmful' to aquatic organisms and 'no acute toxicity' upon ingestion [82], [83]. The rest of magnetic materials impose biohazard to cells and tissues [84]–[86]. As stated above, our application requires extended implantation of polymer magnets so that only biocompatible materials can be selected. Given that pure iron will be oxidized in-vivo (rust), we selected iron oxide, which is rather stable, as the magnetic material. In addition, a thin layer of pure polymer is coated outside the polymer magnet as a passivation against body fluids and tissues.

Typically, magnetic particles of the same material can be classified, by their grain size, into microparticles (particle diameter > 1 μm), sub-microparticles (500 nm < particle diameter < 1 μm) and nanoparticles (particle diameter < 500 nm). Smaller particles are less likely to conglomerate and achieves more uniform particle distribution within the polymer magnet. However, the design of polymer magnet does not favor smaller particles monotonically. Very small magnetic particles (particle diameter < 20 nm) falls into the superparamagnetic regime where the particles are so tiny that no magnetic domain can be formed for spontaneous magnetization. As a result, superparamagnetic particles lose their magnetization (remanence = 0) upon the removal of applied polarization magnetic field. We selected iron oxide nanoparticles with particle diameter around 50 nm for polymer magnet fabrication.

Silicone polymers are a general category of synthetic polymers with repeating silicon-oxygen structure and have been used extensively for biomedical applications such as implantable devices, wound dressing, controlled drug delivery, etc. [87], [88]. Polydimethylsiloxane (PDMS), which has $-CH_3$ group connected to silicon atom, is the most common type of silicone. Although mechanical properties of PDMS can be modified easily by varying the prepolymer base-to-crosslinker ratio and polymer curing temperature, its stiffness (360-870 kPa) is still nowhere comparable the stiffness of the brain tissue mentioned above (1.895 kPa for white matter, 1.389 kPa for gray matter [78]). Instead we investigated into softer silicones and found a super-soft silicone, Ecoflex®, with an elastic modulus of 28.8 kPa, close to that of the brain tissue. What's more, it has a density of 1.04 g/cm^3 which is almost identical to that of brain tissue (1.0107 g/cm^3 [79]), forming density continuity between the fabricated polymer magnet and brain tissue at the site of implantation.

2.3 Fabrication

Fabrication of the polymeric magnet starts by mixing Ecoflex® supersoft silicone prepolymers (0010, Smooth-On Inc., Macungie, PA, USA 1:1), Figure 17a. A certain load of iron oxide nanoparticles (Fe_3O_4, Sigma-Aldrich, St. Louis, MO, USA 50 nm) is mixed with the silicone prepolymer, Figure 17b. The well stirred mixture is then sent into a vacuum chamber for a 2-minute degassing. This step is crucial for achieving uniform magnetic particle distribution as gas bubbles form cavities that are void of magnetic particles. The degassed mixture is then casted into a 1mm thick acrylic mold left for curing at room temperature for 4 hours, Figure 17c, d. During the curing process, cylindrical neodymium magnets are used to magnetize the iron oxide nanoparticles in the mixture, Figure 17e. Once cured, the polymeric magnet is released from the mold and trimmed into the desired size. Figure 17f, g. Another layer of pure Ecoflex® silicone is then dip-coated over the polymeric magnet as passivation, Figure 17h. The embedded nanoparticles make the polymeric magnetic more susceptible to moisture penetration by loosening the silicone matrices and the less permeable pure silicone layer forms a shell against leaching.

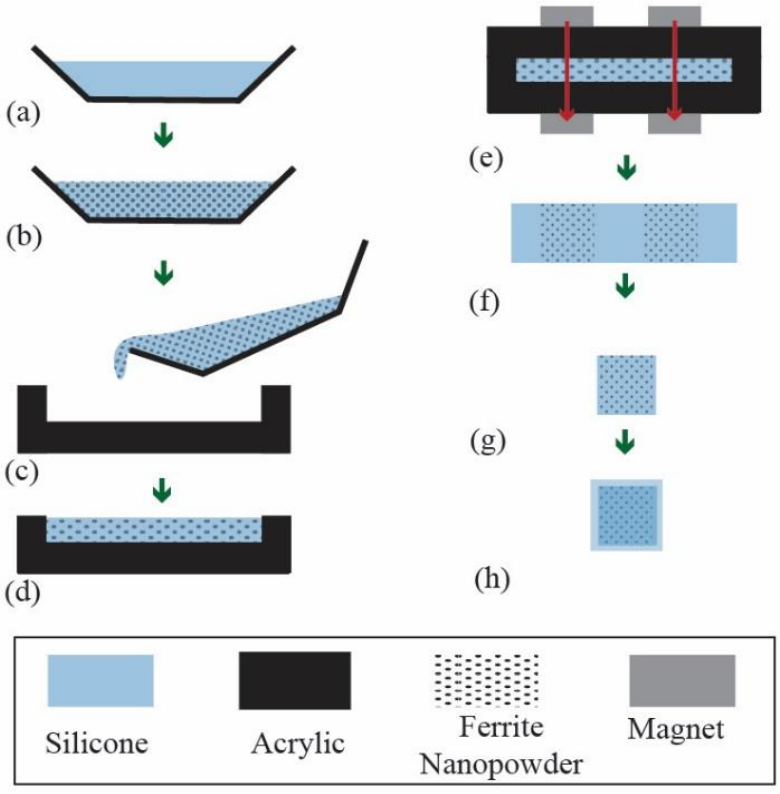

Figure 17. Polymeric magnet fabrication process

Figure 18 shows the fabricated polymeric magnetic disks with different diameters compared with a U.S. one cent coin (penny). Note the additional transparent Ecoflex® layer as passivation against body fluids and tissues.

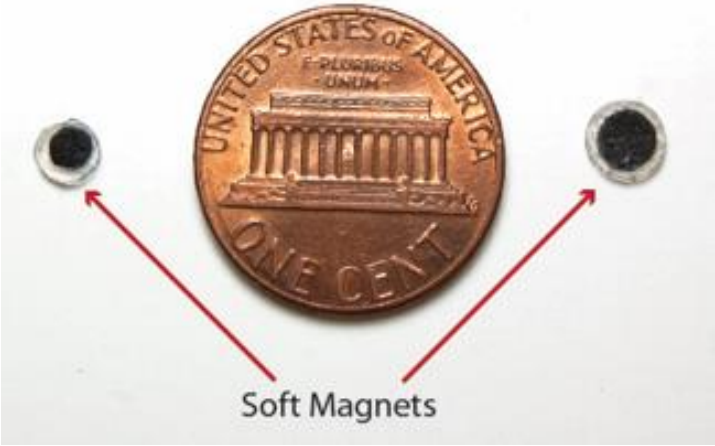

Figure 18. Fabricated 3.5 mm and 5 mm polymeric magnet with magnetic flux intensity around 80 μT, compared with a U.S. one cent coin (penny). Note the additional transparent Ecoflex® layer acting as passivation against body fluids and tissues.

The three GMR sensors (AAH002-02E, NVE Corp., Eden Prairie, MN, USA) are soldered onto a circuit board in a triangular arrangement to track the movement of the soft magnets implanted on dura mater. The detailed sensor configuration on board of the array is illustrated in Figure 19 left. A 5V DC power source is used to drive the sensor array. Hot glue is applied at solder joints to improve mechanical robustness of the wiring. The soldered GMR sensor array is displayed in Figure 19. Upon implantation, a polymeric magnet disc is carefully placed on dura mater so that the sensor array can be aligned parallelly with the magnet later in experiments. This special sensor arrangement fully utilizes the magnet-perpendicular-to-plane sensing mode of the GMR sensor (illustrated in Figure 16) while minimizing the separation between individual sensor, ensuring maximal magnetic field exerted over all three sensors so that a strong magnetic response relative to magnet location is achieved. At the start of the experiment, the disc magnet is aligned around the initial position (red circle in Figure 19) by moving the sensor array so that the readings on all three sensors are high. The blast wave deforms the brain and moves the magnet disc away from the initial position.

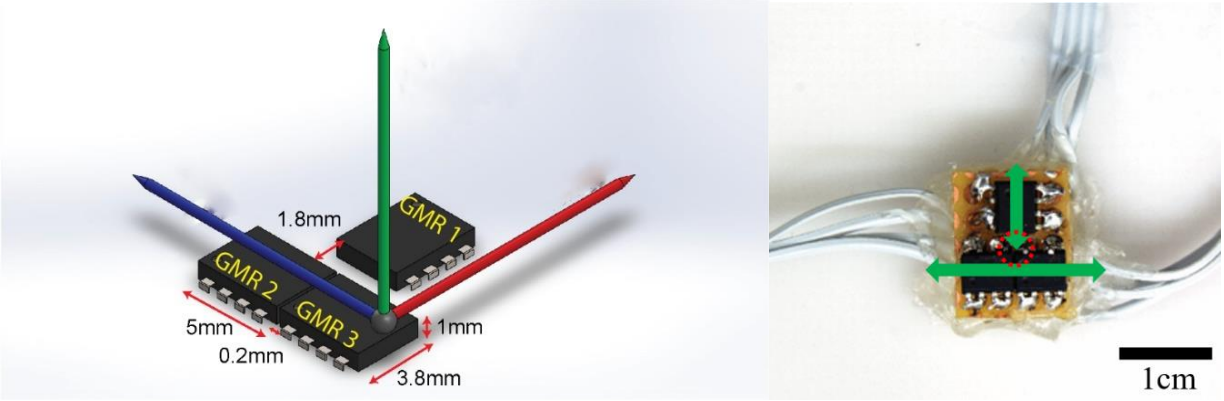

Figure 19. GMR sensor array. Left: GMR sensor arrangement on the sensor array; right: photo of the GMR sensor array. In the right figure, green arrows indicate sensors' axis of sensitivity and red circle shows the approximate position of the polymeric magnet in experiments. Scale bar shows 1 cm.

2.4 Experiment Setup and Methods

2.4.1 Mechanical and magnetic characterization of soft magnet

Soft magnets were prepared in four different loading concentrations (20%, 30%, 40% and 50% by weight) in a rectangular film of 15 × 5 × 0.8 mm^3 for strain-stress characterization. Young's modulus of polymeric magnetic strips with 20%, 30%, 40% and 50% iron oxide were measured via digital mechanical analysis (Q800, TA Instruments, New Castle, DE, USA). Magnetic flux density of the polymeric magnets placed *in vitro* environment (37ºC phosphate-buffered saline) was monitored over three weeks.

2.4.2 Intracranial deformation sensing system calibration, validation, experiments

The GMR sensor's response to directional motion of the polymeric magnet was characterized with an aluminum micromanipulator (460A-XY, Newport Corporation, Irvine, CA, USA). Each GMR sensor was calibrated by scanning the polymeric magnet in a space above the sensor. The overall deformation sensing system was then validated in aid of the high-speed camera. Additional control experiments were also conducted under the same validation setup. All GMR sensor readings were recorded by an oscilloscope and were subsequently transferred to a computer via a USB flash drive. A 2nd order digital Butterworth bandstop filter with cutoff frequencies at 57 and 63 Hz, and a 3rd order digital Savitzky-Golay filter [89] with window size 999 was applied sequentially to all validation and experiment data for denoising purposes.

Following the sensor system validation, the sensor system was applied to different experimental models to measure intracranial brain deformations to study the primary bTBI. The experimental subjects were 3-D printed rat skull filled with 0.6% agarose gel, dead rats, and live rats. Each subject was exposed to an incident blast wave with a maximum overpressure of 150 kPa and 1.5 ms positive phase duration delivered through an open-ended shock tube model.

Animal Subjects All animal procedures were carried out in accordance with animal experimental protocols using 350-400 g male Sprague Dawley rats as approved by the Purdue Animal Care and Use Committee (Protocol #1111000280).

Blast Exposure Blast exposure was conducted with an open-end blast tube producing blast waves as described in Section 2.1.1. An air chamber sealed with polyethylene terephthalate (PET) membrane was connected to one end of the blast tube. Compressed air was pumped into the chamber until the air pressure breaks the membrane and thus releases a blast wave. The peak overpressure of the blast wave was controlled by the thickness of the PET membrane, the thicker the membrane, the higher the peak overpressure. Blast wave with a peak overpressure of 150 kPa was used in experiments. High dynamic pressure sensors (DPX101-250, OMEGA, Norwalk, CT, USA) were mounted at both outlet of the air chamber and the exit of the blast tube. Figure 20 illustrates an exemplary blast experiment setup.

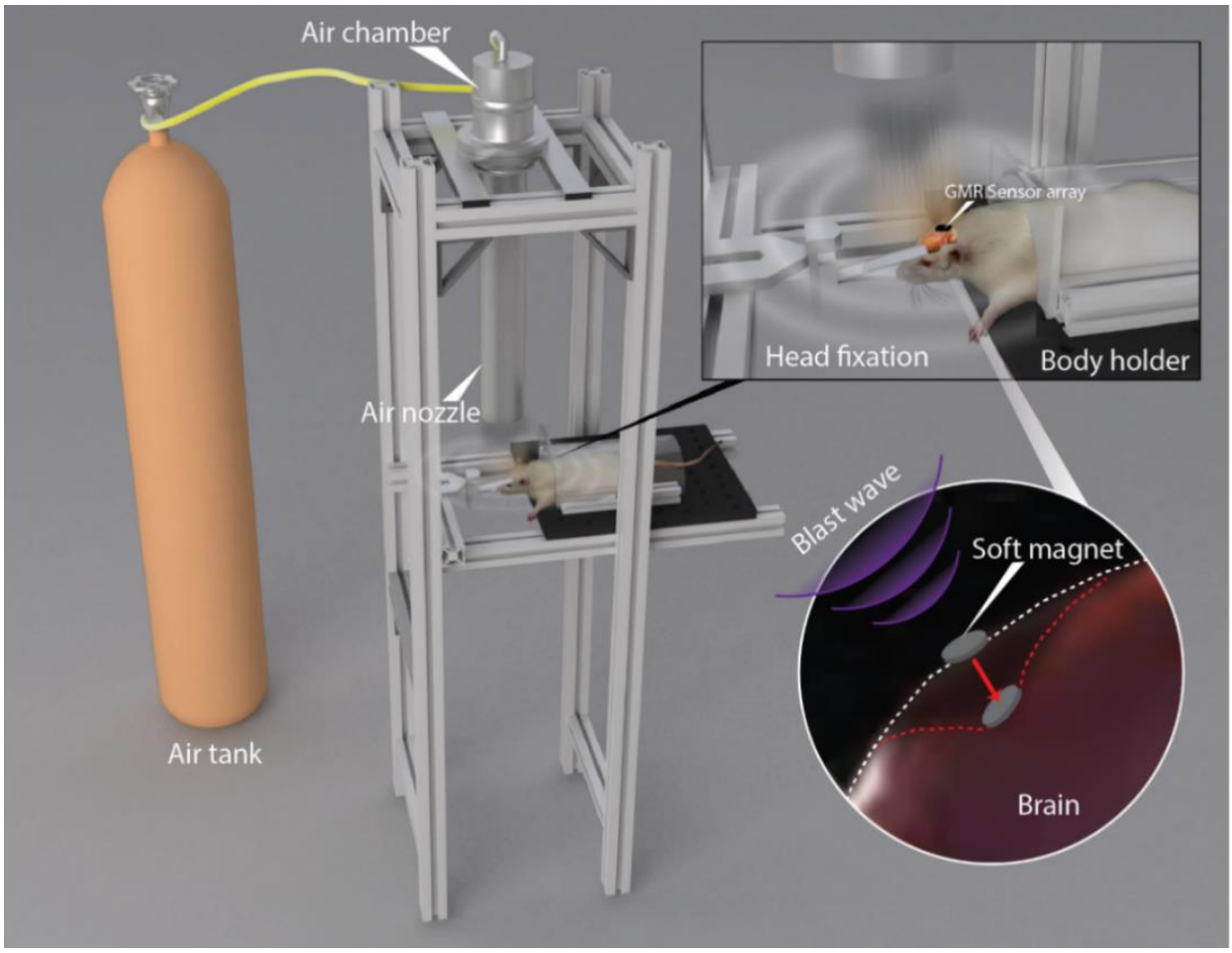

Figure 20. Exemplary blast experiment setup.

Surgical Polymer Magnet Implantation Methods Rats were placed into anesthesia (Ketamine/Xylazine cocktail, 80 mg/kg and 10 mg/kg respectively) or sacrificed before the implantation procedure and had their head shaved prior to surgery. The skull flap was removed during an opening procedure to expose the brain surface (dura mater). The polymer magnet was then positioned at a designated location on the brain surface. Figure 21 shows a picture taken during the implantation procedure with the skull flap opened and polymer magnet positioned (green dashed circle).

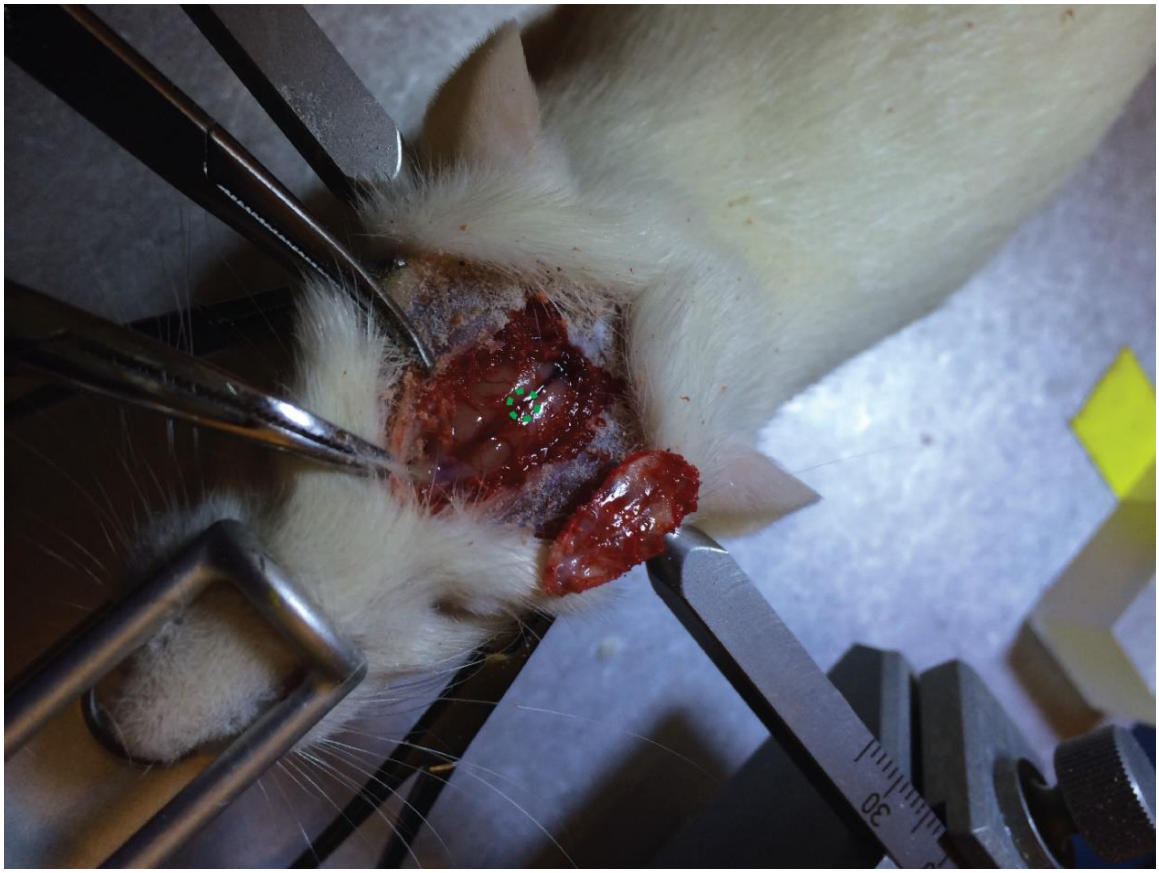

Figure 21. Picture taken during implantation of soft magnet onto the dura mater. The rat was sacrificed just before the surgery. The typical implantation site is outlined by a green dashed circle.

The removed skull flap was placed back in its original position and acrylic bone cement powder (Simplex P., Stryker Instruments) was applied into the gap between the removed skull and the rest of the skull. Please see [90] for more details regarding the sensor implantation procedure.

High-Speed Camera Imaging The validation of wireless magnetic deformation sensing system involves direct comparison between the deformation recorded by the sensing system and that observed from a high-speed camera (Vision Research Phantom Camera v7.1M). High-speed video recordings were captured at a rate of 66666 frames per second. Only one-dimensional (vertical) movement was induced in the validation experiment as it is hard to measure three-dimensional motion accurately with a single high-speed camera.

2.5 Results

2.5.1 Polymeric magnet characterization

Because the system operates by tracking an implanted soft magnet, both magnetic and mechanical properties of the polymeric soft magnets are critical parameters. The soft magnet must have sufficient magnetic strength to be measured wirelessly at reasonable distance. In addition, for the soft magnet to move with the brain during the deformation and not to injure the tissue, the Young's modulus of the soft magnet needs to be similar to that of the brain (1–40 kPa depending on rate and magnitude of the impact, [46], [71]). If too stiff, the soft magnet could penetrate the brain during deformation in a similar manner to a projectile, damaging the brain and compromising the accuracy and validity of the system. If too pliable, the soft magnet could be permanently deformed during bTBI after absorbing the impact during a blast event, which would potentially change the magnetic field in a manner inconsistent with our calibration efforts.

Generally, the soft magnets became magnetically stronger and mechanically stiffer as the concentration of doped iron oxide nanoparticles increased. Among the four different particle concentrations (weight percentage) tested; 20, 30, 40, and 50%, 30 and 40% loading concentrations provided a good combination of mechanical and magnetic properties; whereas the 20% and 50% were either too magnetically weak or too mechanically brittle. Figure 22 and Table 8 depicts stress vs. strain plots and the polymeric magnets' Young's modulus in comparison with some common elastomeric materials respectively. Note that our pure Ecoflex® has a lower elastic modulus (28.8 kPa) than the modulus of 55.2 kPa stated in the datasheet. We achieved this by skipping the recommended heating process after curing.

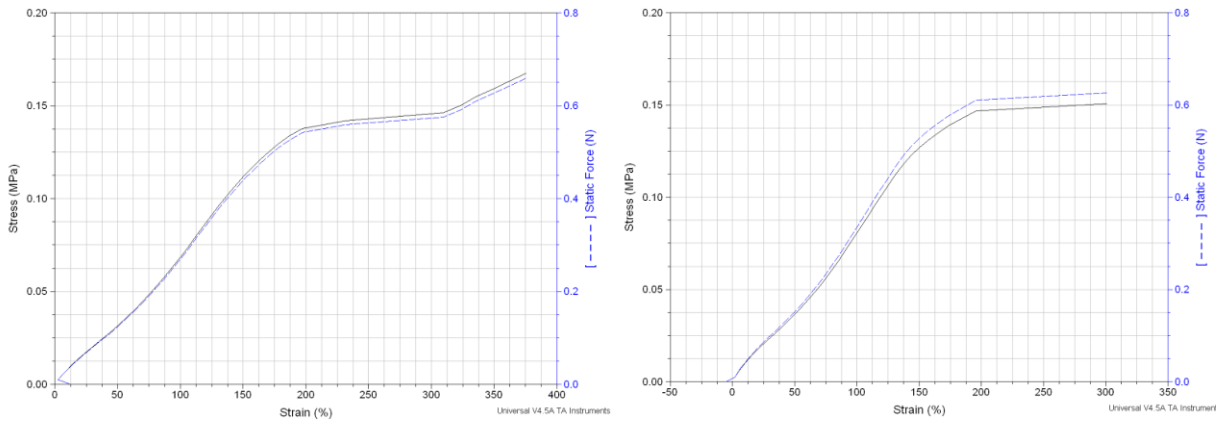

Figure 22. Stress-strain curves of a 30% sample (left) and a 40% sample (right).

Table 8. Young's modulus of polymeric magnets in comparison with common elastomeric materials and brain

Ecoflex	30% sample	40% sample	PDMS	Brain
28.8 kPa	40-70 kPa	60-90 kPa	360-870 kPa	1-40 kPa [46], [71], [78]

To verify the stability of the soft magnet, ten polymeric magnets with 30 and 40% iron oxide loading (5 each) was immersed in 37ºC phosphate buffered saline (PBS) and their magnetic flux density was measured at the surface of the disk daily over 25 days, Figure 23. Polymeric magnets exhibited the strongest magnetic flux density right after fabrication and the flux density decayed gradually over time. It stabilized after approximately 20 days and were ready for implantation. After the characterization, 30% soft magnets were chosen to be utilized in the intracranial brain deformation sensor system for its excellent magnetic and mechanical properties.

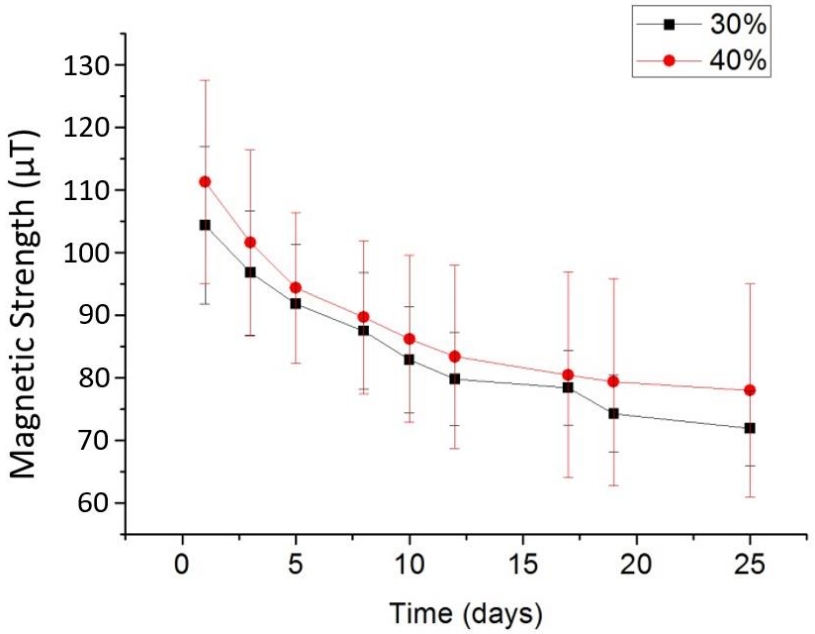

Figure 23. Magnetic flux density of polymeric magnets over 25 days.

2.5.2 GMR sensor calibration

The characterization of the GMR outputs as a function of the soft magnet positions was performed by scanning a soft magnet over a single GMR sensor with a motor-controlled micro-

manipulator at a step size of 100 μm over a cubic space of 1 cm^3. Figure 24 explains the scanning procedure (not drawn to scale). The voltage output of the GMR sensor was recorded as a function of the relative soft magnet position.

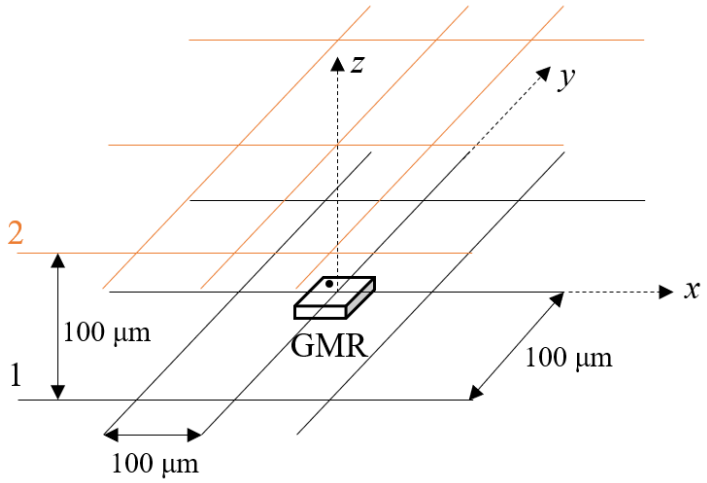

Figure 24. Schematic showing the scanning procedure in sensor calibration. A polymeric magnet was scanned along horizontal lines that are 100 μm apart. Each level of line grid is also separated by 100 μm.

As a proof of concept, a calibration containing polymeric magnet movements only along the z-axis in Figure 24 was conducted. Calibration results of a 30% and a 40% polymeric magnet initially placed at (0, 0, 0) moving away from the GMR sensor along the z-axis is shown in Figure 25. Both 30% and 40% magnets showed good linearity between 500 μm and 8500 μm with good repeatability. Distance sensitivity within linear range were 0.0083 μT/μm and 0.0095 μT/μm for 30% and 40% magnets, respectively, indicating the feasibility of using the proposed sensing system for wireless magnetic localization.

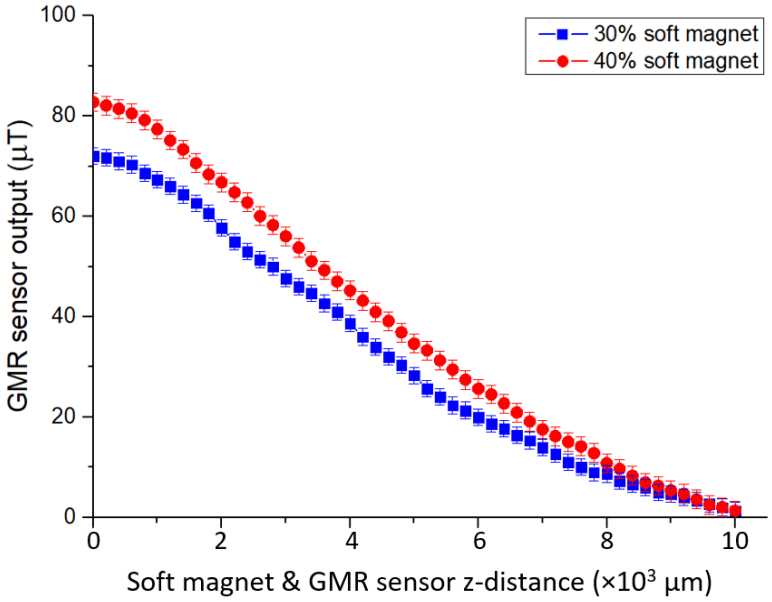

Figure 25. Calibration results of a 30% and a 40% polymeric magnet initially placed at (0, 0, 0) moving away from the GMR sensor along the z-axis. Earth magnetic field had been subtracted.

Three slices of the scanned calibration map are shown in Figure 26a. Each slice shows the magnetic field strength measured by a GMR sensor as a function of X-Y position at Z = 0, 200, and 400 μm. Note that a baseline voltage indicating the signal from geomagnetic field was measured and subtracted from the recordings. The same baseline was also measured prior to each experiment. The color map indicates the magnetic field strength w.r.t the Earth's magnetic field.

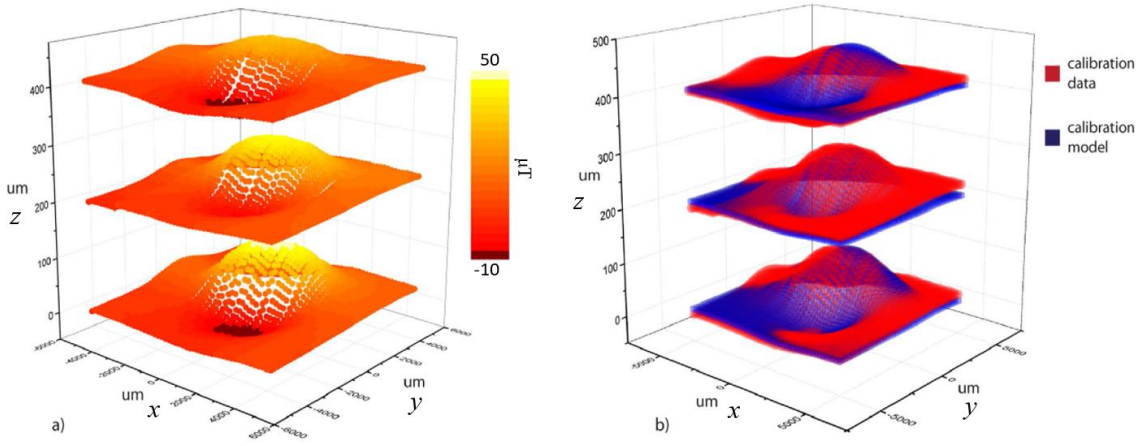

Figure 26. (a) Three horizontal slices of the measured magnetic strength as a relative position of a soft magnet. (b) Calibration model using two 3-variable Gaussian functions in comparison with the measured data. A GMR sensor is placed at (0, 0, 0) in both (a) and (b).

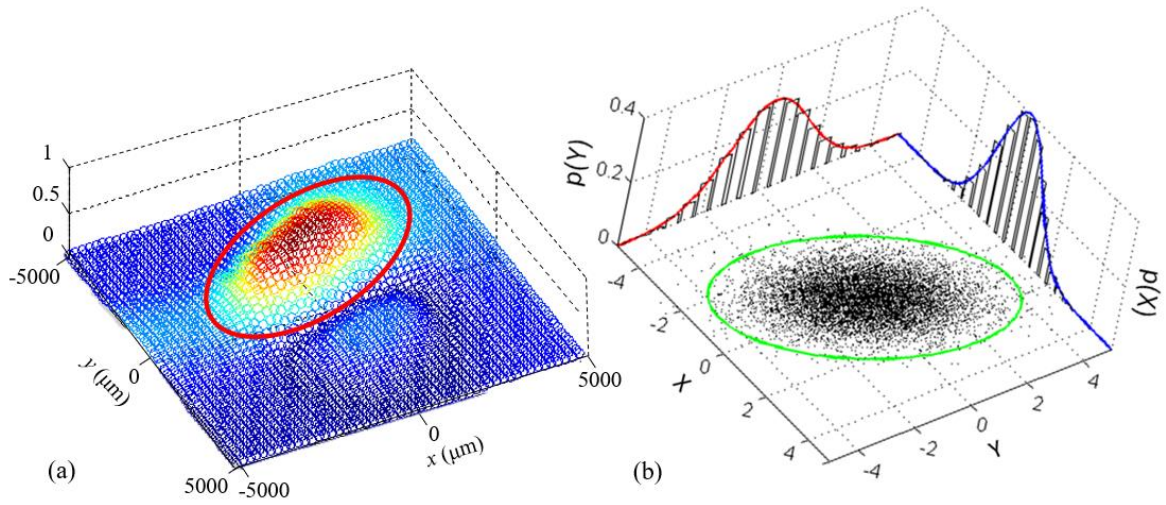

Figure 27. (a) A horizontal slice of measured magnetic strength as relative position of a soft magnet. (b) An exemplary of multivariate Gaussian distribution. Data distribution in the red circle of (a) is similar to that in the green circle of (b).

Figure 27 compares the calibration result with a multivariate Gaussian distribution and their data distributions look alike. The calibration data was then modeled as a sum of two 3-variable Gaussian functions, which accurately described the measurement as the two overlap in Figure 26b. It is notable that the calibration model consists of two Gaussian functions, each representing the positive peak and the negative peak of the calibration data, along with a constant M_0 representing a DC offset of the reading. The equations and the parameters of the calibration model are

Overall:
$$M(x,y,z) = M_0 + M_1(x,y,z) + M_2(x,y,z) \quad (6)$$

Positive peak:
$$M_1(x,y,z) = A1 \cdot exp\left(-\frac{1}{2}\left[\left(\frac{x\cos\theta + y\sin\theta - x_{c1}\cos\theta - y_{c1}\sin\theta}{w_{x1}}\right)^2 + \left(\frac{-x\sin\theta + y\cos\theta + x_{c1}\sin\theta - y_{c1}\cos\theta}{w_{y1}}\right)^2 + \left(\frac{z - z_{c1}}{w_{z1}}\right)^2\right]\right) \quad (7)$$

Negative peak:
$$M_2(x,y,z) = A2 \cdot exp\left(-\frac{1}{2}\left[\left(\frac{x\cos\theta + y\sin\theta - x_{c2}\cos\theta - y_{c2}\sin\theta}{w_{x2}}\right)^2 + \left(\frac{-x\sin\theta + y\cos\theta + x_{c2}\sin\theta - y_{c2}\cos\theta}{w_{y2}}\right)^2 + \left(\frac{z - z_{c2}}{w_{z2}}\right)^2\right]\right) \quad (8)$$

Parameters except for (x, y, z) in the above Gaussian functions were fitted from calibration scanning data and are manifested in Table 9.

Table 9. Gaussian function parameters.

Variable Name	Value	Variable Name	Value
M_0	0.059	–	–
A_1	2.8	A_2	-0.95
Xc_1	200	Xc_2	500
Yc_1	1300	Yc_2	-1630
Zc_1	-3817	Zc_2	-3817
Wx_1	2000	Wx_2	1600
Wy_1	1000	Wy_2	2000
Wz_1	2090	Wz_2	2090
θ_1	0.5	θ_2	0

From the voltage output of GMR a series of possible positions can be inferred by solving Equations Overall: $M(x,y,z) = M_0 + M_1(x,y,z) + M_2(x,y,z)$ (6)Positive peak: $M_1(x,y,z) = A1 \cdot exp\left(-\frac{1}{2}\left[\left(\frac{xcos\theta+ysin\theta-x_{c1}cos\theta-y_{c1}sin\theta}{w_{x1}}\right)^2 + \left(\frac{-xsin\theta+ycos\theta+x_{c1}sin\theta-y_{c1}cos\theta}{w_{y1}}\right)^2 + \left(\frac{z-z_{c1}}{w_{z1}}\right)^2\right]\right)$ (7)Negative peak: $M_2(x,y,z) = A2 \cdot exp\left(-\frac{1}{2}\left[\left(\frac{xcos\theta+ysin\theta-x_{c2}cos\theta-y_{c2}sin\theta}{w_{x2}}\right)^2 + \left(\frac{-xsin\theta+ycos\theta+x_{c2}sin\theta-y_{c2}cos\theta}{w_{y2}}\right)^2 + \left(\frac{z-z_{c2}}{w_{z2}}\right)^2\right]\right)$ (8). The only correct position can be selected from a list of possible positions by solving a series of GMR position prediction equations simultaneously for all three GMR sensors. Accounting for the location offset of the three GMR sensors, the following equations can be derived:

$GMR_1\left(x - x_{GMR_1}, y - y_{GMR_1}, z - z_{GMR_1}\right)$

$$= M_0\left(x - x_{GMR_1}, y - y_{GMR_1}, z - z_{GMR_1}\right) + M_1\left(x - x_{GMR_1}, y - y_{GMR_1}, z - z_{GMR_1}\right)$$
$$+ M_2\left(x - x_{GMR_1}, y - y_{GMR_1}, z - z_{GMR_1}\right) \quad (9)$$

$$GMR_2\left(x - x_{GMR_2}, y - y_{GMR_2}, z - z_{GMR_2}\right)$$
$$= M_0\left(x - x_{GMR_2}, y - y_{GMR_2}, z - z_{GMR_2}\right) + M_1\left(x - x_{GMR_2}, y - y_{GMR_2}, z - z_{GMR_2}\right)$$
$$+ M_2\left(x - x_{GMR_2}, y - y_{GMR_2}, z - z_{GMR_2}\right) \quad (10)$$

$$GMR_3\left(x - x_{GMR_3}, y - y_{GMR_3}, z - z_{GMR_3}\right)$$
$$= M_0\left(x - x_{GMR_3}, y - y_{GMR_3}, z - z_{GMR_3}\right) + M_1\left(x - x_{GMR_3}, y - y_{GMR_3}, z - z_{GMR_3}\right)$$
$$+ M_2\left(x - x_{GMR_3}, y - y_{GMR_3}, z - z_{GMR_3}\right) \quad (11)$$

The 3D localization (*x*, *y*, *z*) of the polymeric magnet relative to the GMR sensor array can then be computed from the model above.

2.5.3 Intracranial deformation sensing system validation

To verify if the sensor system can measure the position of a soft magnet accurately, a quantitative validation experiment was performed. A soft magnet was embedded in a PDMS block of 1 mm thick sitting on top of the GMR sensor array and was exposed to a 150 kPa peak overpressure blast wave with 1.5 ms positive phase duration. The deformation of the PDMS block, and hence the movement of the embedded soft magnet, was monitored with a high-speed camera. Simultaneously, the GMR sensor outputs were measured during the experiment. The displacement measured with the deformation sensing system was compared to that extracted from images taken with the high-speed camera (Vision Research Phantom Camera v7.1M, 66666 frames per second). For this validation experiment, only the vertical displacement was considered since displacements in other directions were difficult to quantify with a single high-speed camera. The validation experiment results are summarized in Figure 28. The positions of the soft magnet for every 1 ms immediately following the blast are shown in Figure 28a. The yellow dots and the red lines indicate the soft magnets positions and the original position, respectively. In Figure 28b, the initial position of the soft magnet, the GMR sensor array, and the scale bar are shown. From the frame-by-frame

analysis, it was observed that the soft magnet was displaced by about 100 μm in vertical direction and returned to its original position within a few milliseconds as shown as the red dots on the Figure 28c. The position of the soft magnet in vertical (z) direction (sampling rate of 25 kHz) is plotted in the Figure 28c in black solid line. Both the time scale (few milliseconds) and the displacement (120 μm) agreed well with the images taken with the high-speed camera validating the sensor system accuracy in measuring the soft magnet positions. The mean and standard deviation for measurement differences between the result from the sensing system and the ground truth in this recording was 8 μm ± 14.3 μm with most errors occurring at small deformations around the commencement and the end of the blast event. Possible sources of error include reduced localization accuracy at larger magnet-sensor separation (about 1 mm) where the magnetic response is weak, as well as minor polymeric magnet deformation which distorts the induced magnetic field.

Aside from the deformation sensing accuracy validation, two control experiments were conducted to evaluate the sensing system's robustness and signal integrity against any blast-induced signal noise or artefacts. The same experiment setup as the deformation validation was utilized except that in control experiment 1) the polymer magnet was taken out so that the GMR sensor array should not pick up anything other than the static geomagnetic field and in control experiment 2) the polymer magnet is fixed within a rigid aluminum block so that no polymer movement is possible. A representative voltage output of the GMR sensor array output is shown in Figure 29. In both control experiments minimal additional noise and signal artefacts beyond the system's electrical noise floor were observed on site of the blast, inferring good system robustness against the blast wave and that no signal can be observed without the motion of polymer magnet. Thus, we had successfully validated our assumption that the sensing system can only pick up magnetic field dynamics induced from the movement of a polymer magnet in absence of other magnetic sources.

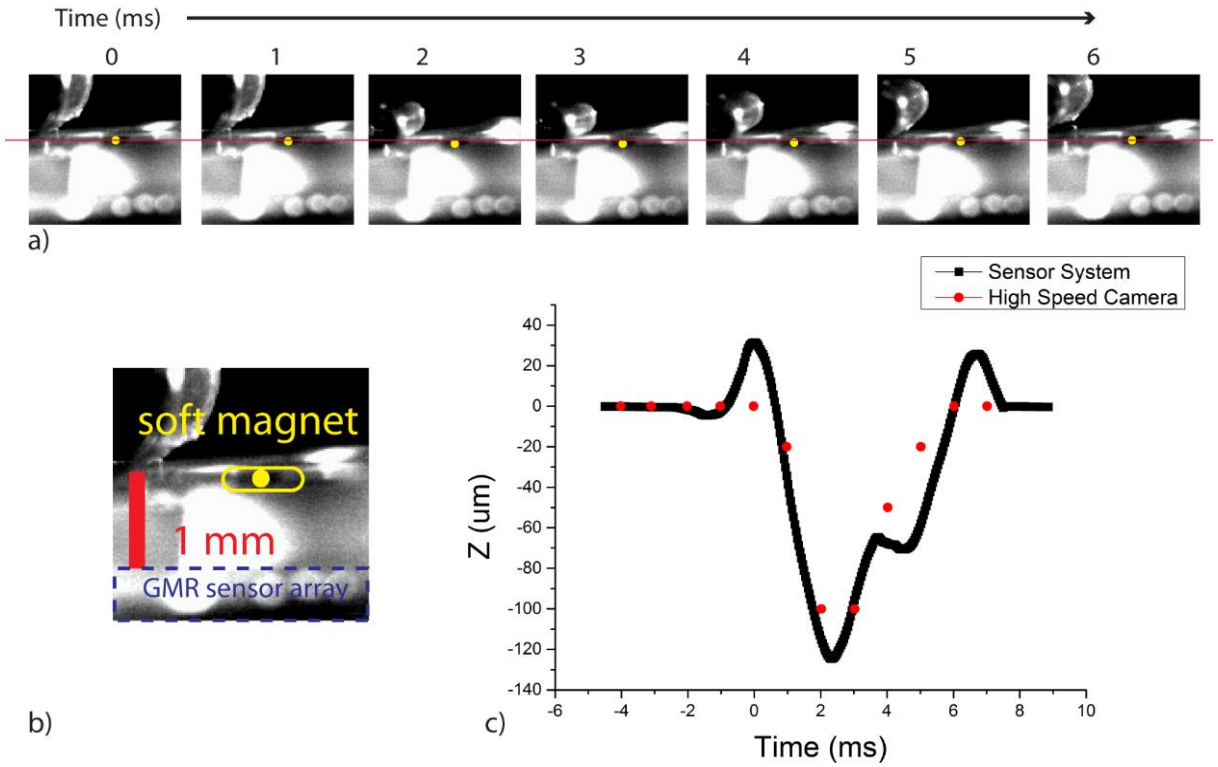

Figure 28. Validation Experiment Results: a) time evolution of the soft magnet displacement following the blast event. The yellow dots indicate the position of the soft magnet and the red line indicates the original position. Maximum deformation of around 100 µm between 2 and 3 ms was observed with a high-speed camera; b) scale bar and the soft magnet location are shown; c) soft magnet displacements relative to its original position measured with the sensor system and the high-speed camera as a function of time.

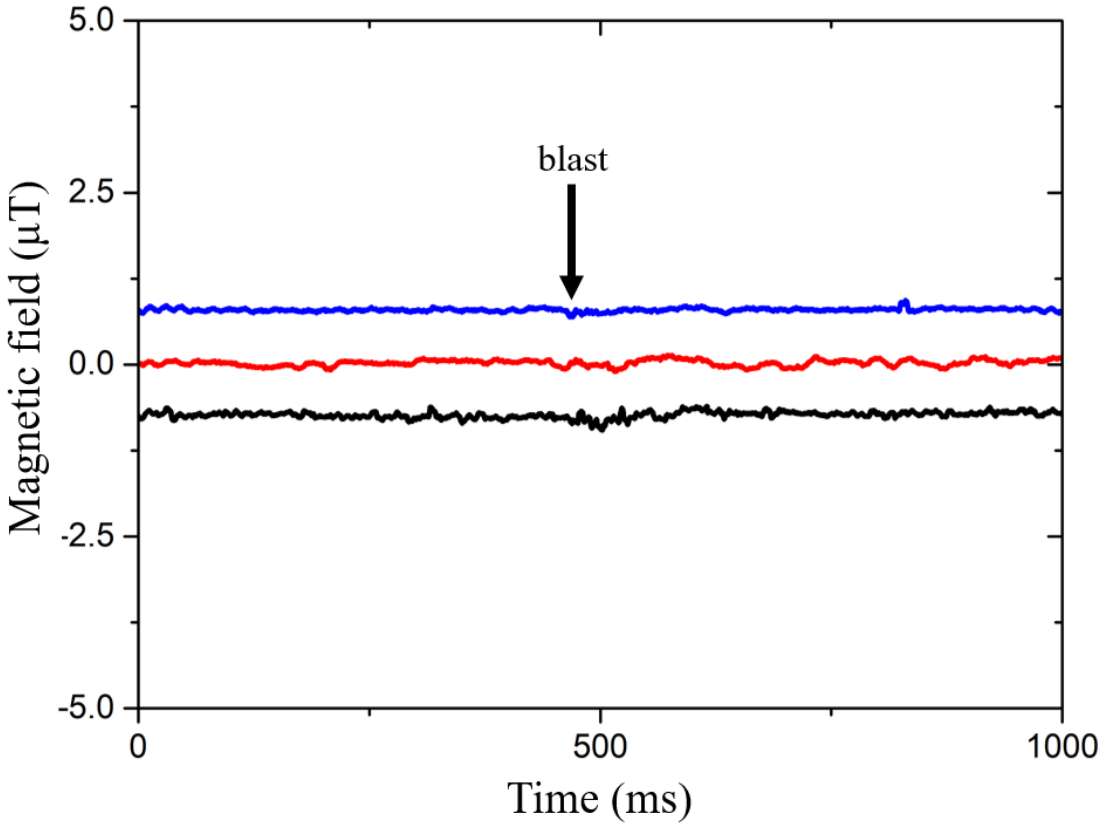

Figure 29. A representative voltage output of the GMR sensor array output of control experiments. The same setup as the deformation validation was utilized except that in experiment 1) the polymer magnet was taken out so that the GMR sensor array should not pick up anything other than the geomagnetic field and in experiment 2) the polymer magnet is fixed within a rigid aluminum block so that no polymer movement is possible. In both control experiments minimal additional noise and signal artefacts beyond the system's electrical noise floor were observed on site of the blast, inferring good system robustness against blast wave and that no signal can be observed without the motion of polymer magnet.

The last assumption to be validated regarding the wireless intracranial deformation sensing system is that the implanted polymeric magnet moves with the brain tissue upon blast induced brain deformation. This was particularly important as no adhesives was applied to bond the polymer magnet and the brain tissue together. To verify that no relative movement between the polymer magnet and the brain tissue is present, CT images were taken to image the brain and the polymer magnet 5 minutes pre- and post-blast, Figure 30. No permanent displacement in any direction is observed from the merged CT images per direction, per animal ($n = 5$; $p_x = 0.521$, $p_y = 0.888$, $p_z = 0.444$ by ANOVA). This confirmed the polymer magnet moved together with, rather than through or in shear motion with the brain during blast-induced tissue deformation.

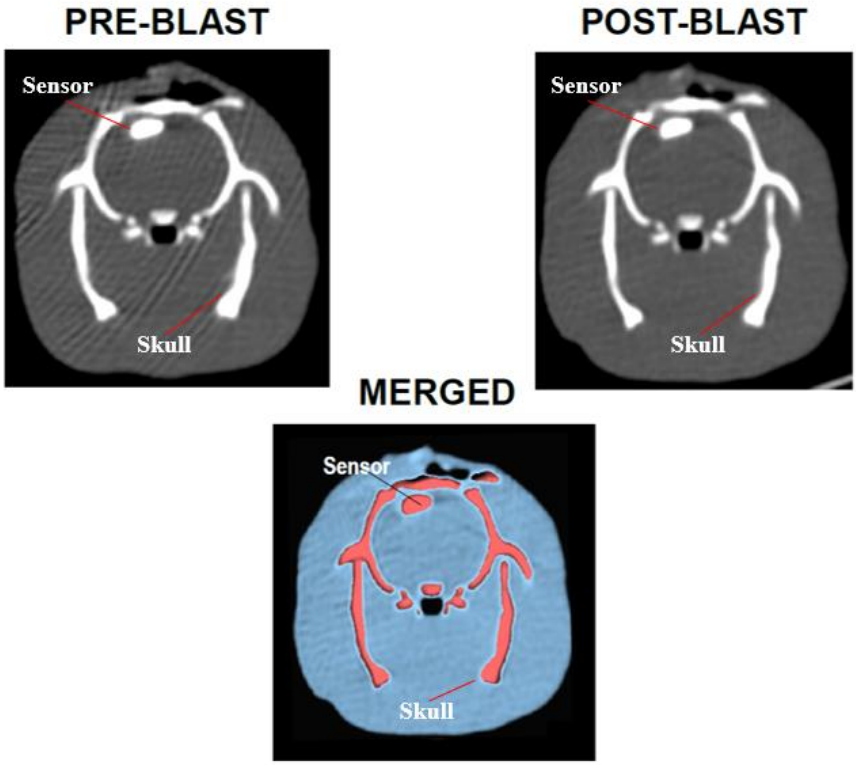

Figure 30. Frontal CT images of the brain and the polymer magnet 5 minutes pre-blast (top-left) and post-blast (top-right) and the merged image (bottom). No permanent displacement in any direction is observed from the merged CT image ($p>0.05$ all axes). This confirmed the polymer magnet moved together with, rather than through or in shear motion with the brain during blast-induced tissue deformation.

2.5.4 Experiment in 3D-printed rat phantom

Following the sensor system validation experiment, the sensor system was applied to different experimental subjects to measure intracranial brain deformations to study the primary bTBI. The experimental models were 3-D printed rat skull filled with agarose gel, dead rats, and live rats. Each specimen was exposed to an incident blast overpressure wave with a maximum overpressure of 150 kPa and 1.5 ms positive phase duration delivered through an open-ended shock tube model. Blast waves were generated by compressing nitrogen into a chamber with one end sealed by a thin (0.025 inch) PET membrane. When the pressure inside the chamber exceeds the mechanical strength of the membrane, the membrane breaks. As a result, the compressed nitrogen is released through the shock tube generating a shock wave that exhibits characteristics mimicking the ideal Friedlander waveform used to describe shock wave phenomena. While a single shock wave was chosen for this study consistent with blast injury models from other investigations and expert recommendations, altering the thickness of the membrane as well as the chamber sizes would allow for tunable shock wave parameters such as overpressure magnitude and positive phase duration.

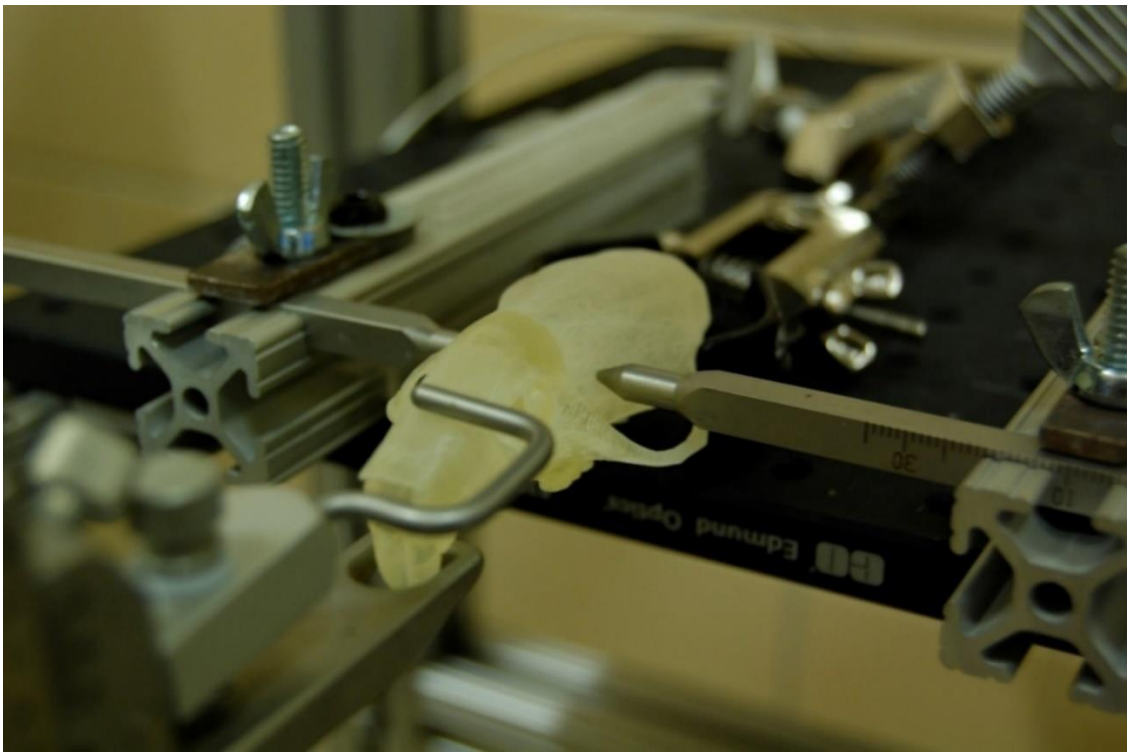

Figure 31. Picture of a 3D printed rat skull model filled with agarose gel fixed under the exit of blast tube.

First, a 3D-printed rat skull was utilized as an experimental model. Its translucent shell allowed an optical monitoring of the soft magnet's position with a high-speed camera. However, the exact displacement was difficult to quantify with the high-speed camera through the translucent skull. Thus, only a qualitative comparison of the soft magnet displacement and the system measurement was feasible. The skull was filled with agarose gel of 0.6% to mimic the mechanical properties of brain tissue. The soft magnet (30%) was placed in the agarose gel with the GMR sensor array was fixed on the skull just above the soft magnet. Figure 31 shows a picture of a 3D-printed rat skull model filled with agarose gel fixed under the exit of blast tube.

The GMR outputs were recorded with an oscilloscope while the position of the soft magnet was monitored with the high-speed camera. The recorded outputs were later converted to positions by inferring from the calibration data, Figure 32.

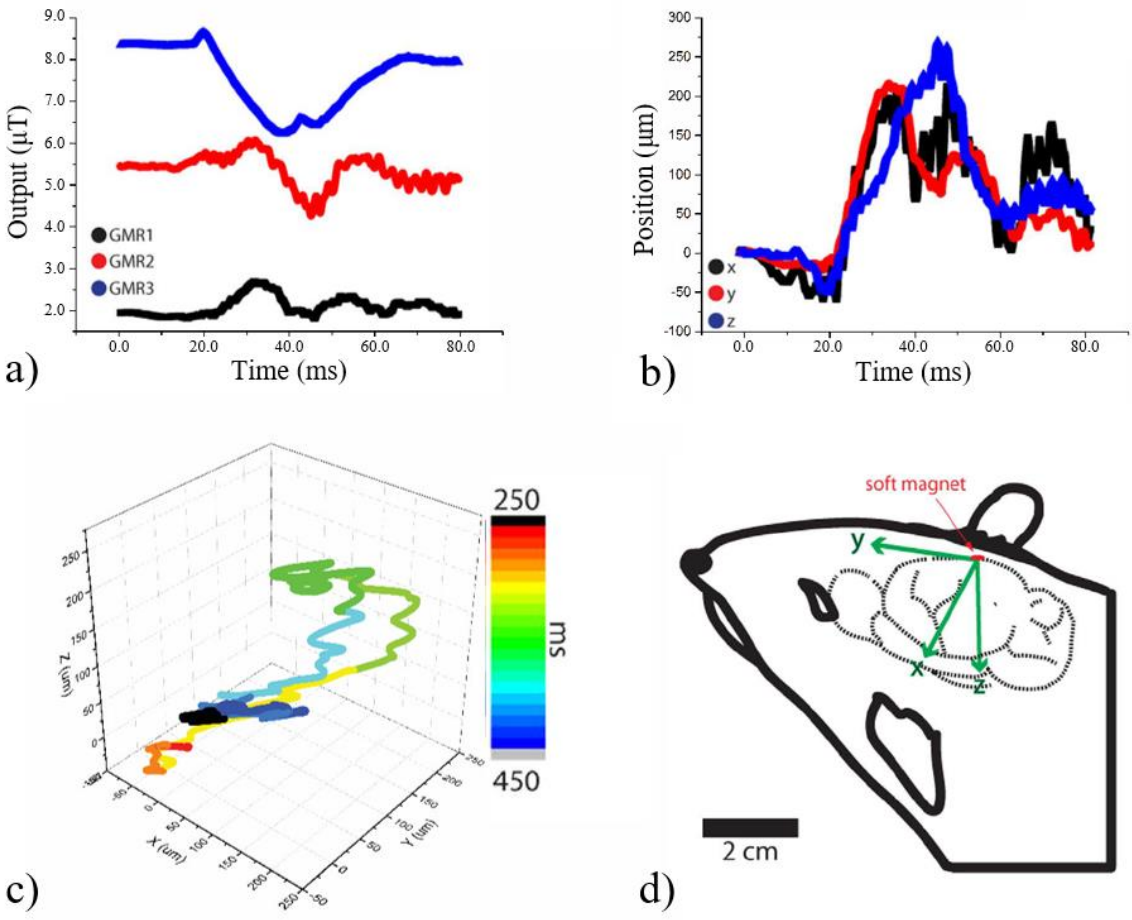

Figure 32. Deformation of agarose gel filled 3D-printed rat skull: a) the GMR sensor array outputs, b) relative position of the soft magnet, c) the trajectory of the soft magnet in 3D printed skull (color indicates time), and d) illustration of coordinates.

2.5.5 In vitro experiment in dead and live rats

In both dead and live rats, the soft magnets were implanted by placing them on top of the dura mater after surgically removing a piece of the skull. The removed piece was later glued back to its original location with bone cement (Simplex P, Stryker Instruments) after the soft magnet implantations. The GMR sensor array was fixed to the skull using a helmet and the wires were taped down. In the experiment with a live rat, the rat was anesthetized prior to the implantation and exposures to blast waves. After the experiment, the rat was sacrificed. The animal experiment setup is illustrated in Figure 30. The rats were held down by an acrylic body holder serving as both a protective gear and an immobilizer, and their heads were immobilized using a stereotaxic head fixation to isolate primary shock wave-induced deformation from secondary blast wind acceleration-induced brain motion. The blast tube was placed right above the head within one shock tube diameter of the outlet for optimal shock wave conditions. Lastly, the GMR array embedded helmet was strapped onto the rats. After sacrificing the rat following the blast experiment, the top of the skull was removed to ensure the implanted soft magnet did not penetrate through dural or brain tissue and to assess any visible deformation to the brain. Although signs of deformation due to the blast were evident as indicated by the measurements, the soft magnet remained superficial to the dura at the implantation site and did not penetrate the tissue, confirming the sensor moved *with* and not through the tissue during bTBI.

Following the experiment with the 3D-printed skull, a dead rat was prepared. The rat was sacrificed just before the surgery to implant the soft magnet and was exposed to a 150 kPa blast wave. The GMR outputs, and the soft magnet position as functions of time are plotted in Figure 33a and Figure 33b. The trajectory of the implanted soft magnet, to the brain of the dead rat, is shown in Figure 33c with the color indicating the time. Immediately after the blast wave, the brain exhibited a deformation-relaxation behavior as expected from viscoelastic materials such as a brain. There was a sustained deformation by a millimeter within 100 ms, mostly in the transverse (ear to ear) direction. The result indicates that a brain can be deformed by an exposure to blast wave even when the head and neck fixation prevent inertial acceleration effects, at least in rat models. Another interesting finding is that the displacement of the soft magnets was mostly in the transverse direction. It indicates that the deformations during the bTBI may not be as simple as a blunt force trauma, but rather have a complex, multi-axial dynamic strain field. Multi-axial deformations with

heterogeneous strain fields have been shown to be more injurious to neurons than uniaxial deformation.

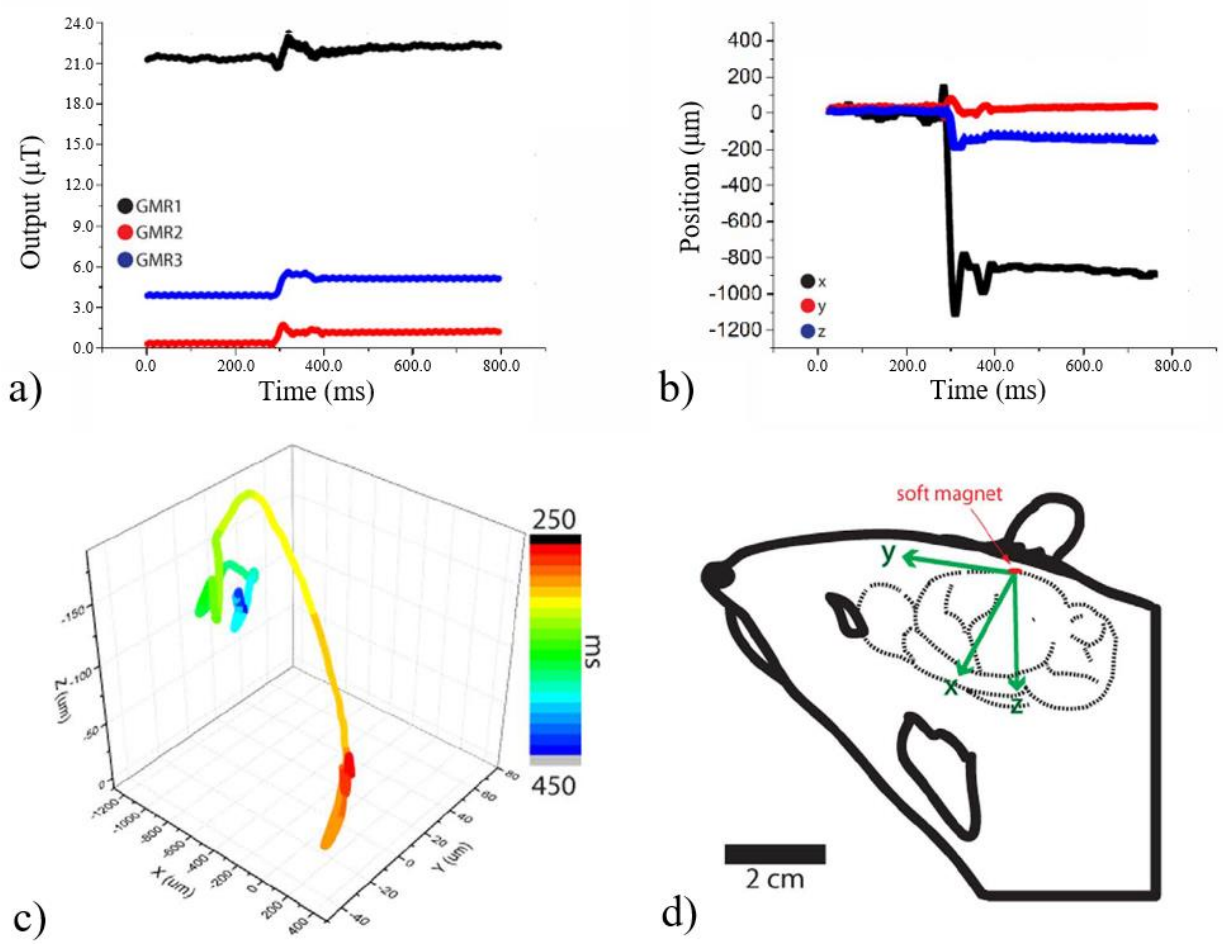

Figure 33. Dead animal with single soft magnet implantation: a) the GMR sensor array outputs, b) relative soft magnet position, c) the trajectory of the soft magnet implanted in dead rat brain (color indicates time), and d) illustration of coordinates.

Lastly, a live rat was given a single soft magnet implantation and the position of the soft magnet was monitored utilizing the same experiment setup as the dead rat. The GMR outputs, soft magnet position, and the trajectory of the implanted soft magnet are plotted in Figure 34. The sustained deformation of 1.6 mm occurred in the time scale of 100 ms. A total of 4 rats, 3 dead and 1 live, were tested with the sensors and each yielded consistent result under multiple exposures to the blast overpressure waves.

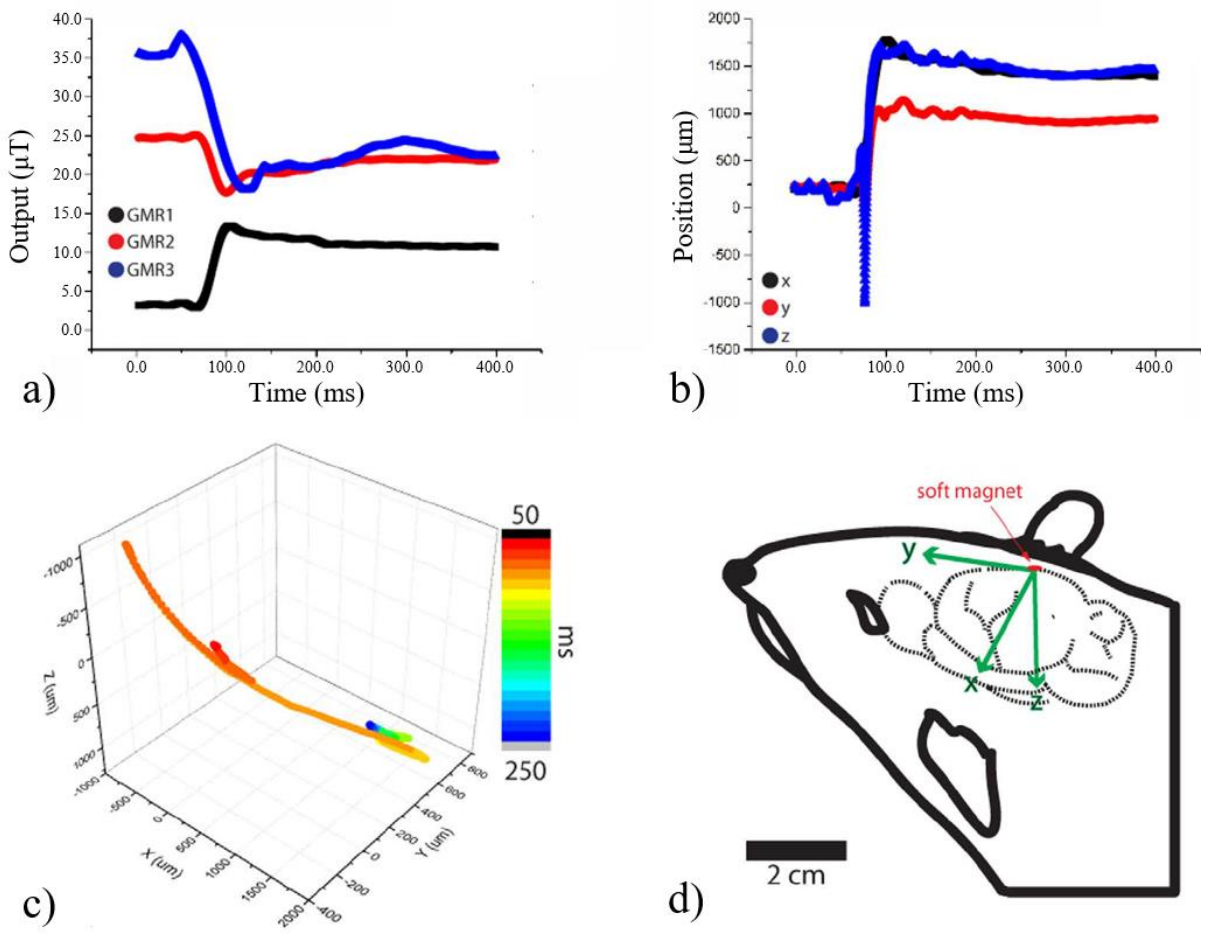

Figure 34. Live animal with single soft magnet implantation: a) the GMR sensor array outputs, b) relative soft magnet position, c) the trajectory of the soft magnet implanted in dead rat brain (color indicates time), and d) illustration of coordinates.

2.6 Discussions

The result indicates that a brain can be deformed by an exposure to blast wave even when the head and neck fixation prevent inertial acceleration effects, at least in rat models. Another interesting finding is that the displacements of the soft magnets were mostly in the dextrosinistral (ear-to-ear, x-axis in Figure 34) direction. It indicates that the deformations during bTBI may not be as simple as a blunt force trauma, but rather have complex, multi-axial dynamic strain fields which have been shown to be more injurious to neurons than uniaxial deformation. Compared to the dead rat's brain, the brain of the live rat appeared to be more pliable and softer as the time scale of relaxation (about 100 ms compared to 90 ms) and the degree of sustained deformations (1.6 mm compared to about 1 mm) were both larger than those of the dead rat. It is expected, however, that

on a longer time scale the living brain would completely relax back to its original position as fluid spaces re-equilibrate. These differences in the mechanical response, arising from the viscoelastic properties of the brain, under a blast wave are attributed from the biological differences between the dead and live animals; even though the rats were sacrificed minutes before the implantation and subsequent experiments, the lack of perfusion and the drainage of the cerebral fluid could change the mechanical properties and cause stiffening of the brain. Magnetic resonance elastography showed that a Yorkshire pig's cerebrum stiffened by 26% in just three minutes post mortem [91], which is likely to be caused by substantial influx of fluid at the collapse of the ionic homeostasis in the dying brain [92] and subsequent neuronal swelling [93]. The ability to capture post-mortem tissue stiffening behavior is another indication of the sensor's capability of detecting the intracranial deformation of the brain during bTBI consistent with expected material behavior.

From these results, it is clear that the 3D printed skull-brain simulants, dead rats, and live rats exhibited a wide range of mechanical behavior. Table 10 provides a summary of the major intracranial dynamics observations for each set of experiments. The observed results are consistent with expectations from existing literature. Brain tissue has a strain-rate dependent elastic modulus with more rigid behavior at higher strain-rates. Brain deformations during blast injury, though yet to be extensively studied, are expected to exhibit strain rates upward of $100s^{-1}$, levels which exceed reported damage thresholds at the cellular level. The brain tissue's viscoelastic behavior has been demonstrated to have moduli ranging from less than 1 kPa for quasi-static deformations ($< 0.1s^{-1}$ strain rate) up to 60 kPa for high rate dynamic deformations ($3000s^{-1}$ strain rate), both of which are lower than 0.6% agarose at comparable strain rates. The gel's motion was additionally constrained due the fact that it completely filled its containing compartment, the 3D printed skull, whereas the brain in both the dead and live animals contained CSF fluid spaces around and within the brain which would allow for additional movement. All tissues, including the brain, have been consistently demonstrated to stiffen significantly post-mortem. While the post-mortem time was minimized to the extent possible when testing the dead rat, this fact, paired with post-mortem lack of blood perfusion and consequential decreased water content, would be expected to raise the stiffness and solid-like characteristics of brain tissue behavior in the dead rat when compared to the live rat. Materials with lower stiffness and less solid-like behavior are less resistant to motion imposed by an outside force, thus reach higher internal deformations and velocities. By this logic, it is sensible that the greatest displacement and velocity were recorded in the live rat, while the

smallest displacement and velocity were recorded in the 3D printed skull filled with agarose gel as reflected in Table 10.

Table 10. Summary of Intracranial Dynamics during bTBI Experiments

Model	**Max Displacement**	**Max Velocity**	**Sustained Displacement**
3-D print skull	350 μm (at 20 ms)	23 mm/s	50 μm (at 60 ms)
Dead rat	1.2mm (at 25 ms)	50 mm/s	1 mm (at 90 ms)
Live rat	2.1 mm (at 30 ms)	70 mm/s	1.6 mm (at 100 ms)

However, due to the limited sensing distance (~1 cm), the GMR sensor array was exposed to the blast wave, causing an overestimation of the displacement at the moment of the impact. Although the effect was short-lived (< 1 ms), this could be resolved by using different type polymer or different magnetic powder to increase the magnetic strength. Despite this limited sensing distance, the system was successful in measuring the displacement of the soft magnet under blast waves, whose results reflected the difference in response due to the difference in mechanical properties of PDMS, agarose gel, and rat's brain (validation, 3D printed, dead and live rats).

This is the first report of direct *in situ* and *in vivo* monitoring of localized brain deformation under bTBI (at the implantation site) using animal models with a novel implantable sensor system. By implanting multiple soft magnets, the mapping of the brain deformation during bTBI could be obtained, although this would require further refinement of the method. However, the current size restriction imposed by rat anatomical features resulted in the present method to track only up to two soft magnets simultaneously. Moreover, in the present study, only surface soft magnet implantations (between dura and skull) were performed. This limitation was influenced by three major factors: magnetic field detection limits, vascular obstruction of subdural implantation, and potential for seizure on deep implantation. It is our current ongoing effort to address the limitations by increasing the magnetic strength of the soft magnet while reducing the form factor, refining the current surgical method, and identifying alternative methods to allow for deep implantation of the soft magnet into the brain.

Despite the abovementioned limitations, the presented system provides a unique tool in studying the brain's mechanical behavior during bTBI. Understanding of brain's mechanical

deformation under bTBI is important, as it has been shown to damage neurons in both magnitude and rate-dependent fashions in other models of neural trauma. In the future, sub-dural implantations should be systematically explored to assess the mechanical response (stress, strain, strain rate, etc.) in a specific brain region of interest. Such efforts may identify brain regions predisposed to mechanical injury from primary blast exposure. Further, this system should be used to study traditional impact-acceleration TBI as well as combined primary and secondary bTBI to directly compare the brain's mechanical behavior between different traumatic brain injury modalities. This novel sensor system will allow for testing hypotheses regarding pathogenesis post-TBI neuropathologies that have been largely speculative and shed light on potential methods for injury prevention, diagnosis, and treatment.

2.7 Conclusion

We present a wireless sensing system capable of monitoring the intracranial brain deformation in real-time during the event of a bTBI. The system consists of an implantable soft magnet and an external head-mounted magnetic sensor that can measure the field in three dimensions. The change in the relative position of the soft magnet *with* respect to the external sensor as the result of the blast wave induces changes in the magnetic field. The magnetic field data in turn is used to extract the temporal and spatial motion of the brain under the blast wave in real-time. The system has temporal and spatial resolutions of 5 μs and 10 μm. Following the characterization and validation of the sensor system, we measured brain deformations in a live rodent during a mild-bTBI. A series of experiments conducted on 3D printed skull phantom, dead and live rats with the deformation sensing system proved the long-standing myth that there exists substantial brain tissue deformation during mild-bTBI that could attribute to the brain injury and complications. More accurate computational mild-TBI models, more effective therapies and better protective gears can be developed based on biomechanical advancements enabled by our developed wireless intracranial deformation sensing system.

3. A WIRELESS STRAIN SENSING AND ACTUATION SYSTEM FOR HEART FAILURE AND BLADDER DYSFUNCTION MANAGEMENT[2]

3.1 Background

3.1.1 Introduction to physiological strains

It is crucial to monitor physiological strains since abnormal strain values can be an important indicator of organ dysfunctions or body diseases. Such correlations between abnormal strains and physiological abnormalities are prevalent within a number of organs and tissues including heart, bladder, uterus and skeletal muscle. Left ventricle (LV) global longitudinal strain (GLS), which measures the percentage of longitudinal LV length change at end-systole (end of blood pumping) comparing to that at end-diastole (end of blood filling), is a sensitive means for probing systolic heart failure, where LV is too weak to contract sufficiently. A GLS $\geq$ -12% is considered abnormal [48]. A similar correlation was also seen between reduced GLS and diastolic heart failure, where LV becomes too stiff to relax normally so that it cannot be filled properly with oxygenated blood during the diastole cycle [49] The strain of the bladder tissue reflects bladder volume, which varies irregularly for patients with bladder dysfunction, especially with urinary retention. During pregnancy the uterus can bear 5 times strain and expands its volume by 100 times. Also, the strain changes rapidly upon uterus contraction, a sign of incoming labor. In this case, it is crucial to monitor strain rates in addition to strain values. In sports medicine, skeletal muscle normally shortens for 50%-60% and an extended or reduced range of motion indicates muscle fatigue or damage. Table 11 displays normal and abnormal strains for various organs. From these examples we can see that the strain gauge of organs and tissues, especially chronical strain monitoring, can facilitate diagnosis and improve treatments.

[2] Parts of this chapter was previously published in 'A Wireless, Smartphone-Aided Magnetic Strain Sensor for Biomedical Applications' in *IEEE 30th International Conference on Microelectromechanical Systems (MEMS)* by T. Zhang, R. Rahimi, M. Ochoa, and B. Ziaie [122], ©2017 IEEE. In reference to IEEE copyrighted material which is used with permission in this thesis, the IEEE does not endorse any of Purdue University's products or services. Internal or personal use of this material is permitted. If interested in reprinting/republishing IEEE copyrighted material for advertising or promotional purposes or for creating new collective works for resale or redistribution, please go to http://www.ieee.org/publications_standards/publications/rights/rights_link.html to learn how to obtain a License from RightsLink. If applicable, University Microfilms and/or ProQuest Library, or the Archives of Canada may supply single copies of the dissertation.

Table 11. Normal and abnormal strains for various organs.

Organ	Complication	Normal/abnormal Strain (%)
Heart	Systolic heart failure	GLS ≤ -16 / GLS ≥ -12 [48]
Heart	Diastolic heart failure	GLS ≤ -15.8 / GLS > -15.8 [49]
Bladder	Bladder dysfunction	0-100 / > 100
Uterus	Pregnancy	0 / 500

3.1.2 Congestive heart failure: definition, epidemiology, monitoring, and management

Wireless measurement of physiological strain in specific tissues can provide significant diagnostic information regarding many important cardiovascular and pulmonary diseases. In particular, heart failure (HF), the inability of the heart to pump sufficient blood (a major public health issue [94]), can be evaluated by measuring LVGLS during the cardiac cycle. Implantable hemodynamic monitoring systems, such as CardioMEMS^{TM} HF system, can provide real-time cardiac pressure information that allows smarter HF management, leading to fewer hospitalizations and lower medical expenditure [95]. However, such systems require complicated fabrication and custom-made, cumbersome interrogation systems [96]. A more modern alternative for chronic physiological strain measurement is the use of smartphones as a platform for collecting, transmitting and analyzing physiological parameters due to their portability (mobile computation power) and the integration of various physical sensors on board. Among the various sensing modes available via smartphones, magnetic tracking is a favorable option for implantable pressure, strain, or deformation sensing systems due to its size, passiveness, high sampling rate and the fact that human body imposes zero magnetic interference [10], [11].

3.1.3 Chronic urinary retention: definition, epidemiology, monitoring and management

Urinary retention is the inability to completely empty the bladder during micturition (urination), defined as retaining more than 300 ml residual urine volume. It is part of the lower urinary tract symptoms (LUTS) along with other symptoms including hesitancy to start urine stream, poor or intermittent stream, and incontinence (lack of voluntary control over urination). With urine staying in bladder for an extended period, LUTS may lead to additional complications

such as urinary tract infection, bladder stones and vesicourethral reflux, which is the abnormal flow of urine back to ureters and kidney. Prevalence of LUTS is strongly correlated with age, affecting 47.9% to 76.3% of the population over 40 years old [97], [98].

Common causes of LUTS can be classified into obstructive and non-obstructive ones. Obstructive causes include physical blockage along the urinary tract such as tumor or stones in bladder / urethra, benign prostatic hypoplasia (BPH) in male, and bulge of rectum toward bladder in female (rectocele). Obstructions impose tremendous resistance on urine flow, leading to discomfort or compromised micturition abilities. Non-obstructive causes often involve muscular or neural disorders such as impaired detrusor contractility (IDC) and neurogenic injuries on brain, spinal cord or pelvis. Under muscular or neural disorders, the bladder cannot respond to urine levels properly or perform micturition normally. Figure 35 illustrates some examples of different causes of LUTS.

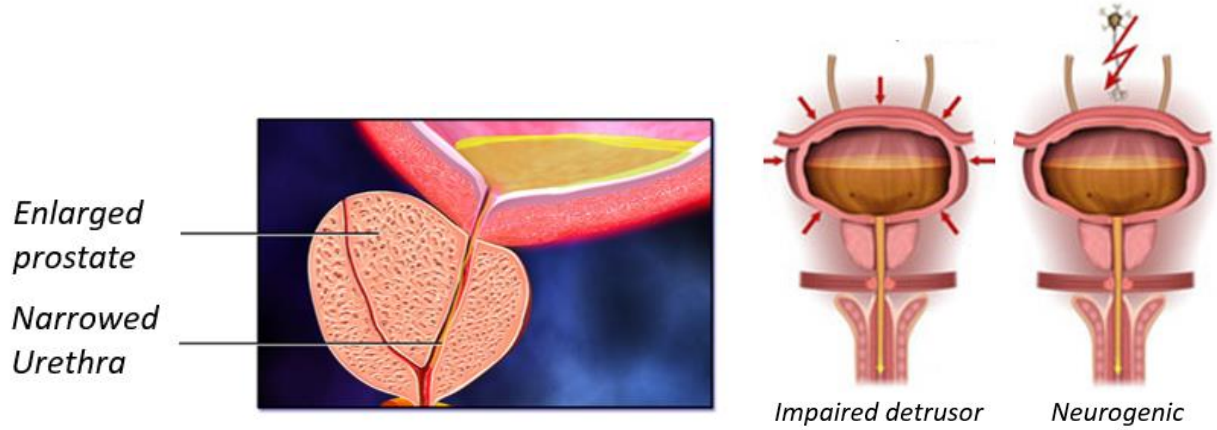

Figure 35. Examples of different causes of LUTS. Left: an obstructive cause where enlarged prostate narrows urethra, leaving smaller space for urine to flow; right: non-obstructive causes where detrusor muscle or neural system is impaired.

Chronic LUTS, especially chronic urinary retention (CUR), require long-term active management and treatments. The purpose of active CUR management is to shunt the retained urine regularly so that it won't cause further complications. The most common means of guiding retained urine is through self-clean intermittent catheterization (CIC), where a catheter is inserted into the bladder via urinary tract to drain any remaining urine. It has been proved to be effective against CUR and is considered safe with careful cleaning. After proper training the patient is able to perform CIC by him/herself and requires no hospitalization. However, CIC needs to be performed

4-6 times daily after each urination and is a lifelong effort if the condition doesn't improve. The discomfort during CIC also causes life quality deterioration and potential urinary tract infection if not cleaning properly. CUR treatment methods vary based on the actual cause of urinary retention. For obstructive causes, treatments often involve ultrasonic or surgical procedures to remove barriers such as stone, tumor, or enlarged prostate. For non-obstructive causes, physical exercise or transplanting healthy skeletal muscle is enforced to restore detrusor muscle functionalities whereas medication and electrode implantation is used to tune and regulate nerves related to LUTS.

To relief the discomfort and troublesomeness during active LUTS management, great emphasis has been addressed on the development of more convenient and comfortable ways of LUTS management. Most developed devices seek gender-specific novel solutions to CUR management caused by sphincter deficiency. AMS 800™ Urinary Control System (Boston Scientific) restores continence with a pneumatic occlusive cuff wrapping around the urethra of male patients, Figure 36 left. Normally the inflatable cuff is filled with liquid, squeezing urethra so that urine is trapped inside the bladder. Upon micturition, the pump which hides within the scrotum, is pressed and released repeatedly to drain the cuff. The inflatable cuff collapses, allowing the urine to flow through the urethra. When the patient finishes urination the button above the pump is pressed to initiate refilling the cuff. Once inflated the cuff will again obstruct the urethra. Vesiflo inFlow™ takes advantage of the shorter urethra in female and designed a tubular magnetic valve-pump that can be inserted into the bladder through urethra, Figure 36 right. This magnetic valve-pump replaces the full functionality of sphincter muscle. It constantly blocks the urethra and an external magnetic actuator is used to drive the magnetic pump wirelessly during micturition. The catheter-like valve requires replacement only once a month instead of inserting catheter tubes multiple times a day, improving the patient's experience and providing better incentives for active LUTS management. Our aim is to develop a novel system with active micturition management capability specifically for IDC related CUR, which is still in void to the best of our knowledge.

In addition to the devices dedicated to refining LUTS management, bladder volume monitors are essential to not only improving clinical diagnosis but also notifying the patients or healthcare personnel when the bladder should be emptied. They are particularly crucial to patients who cannot feel their bladder volume accurately due to neurogenic disorders. Once a bladder volume threshold is reached, the monitoring device can either issue an alert to the patient or healthcare personnel or trigger the active LUTS management device. Early investigation into

bladder volume monitoring dates back to 1970s where electric resistance and impedance volumetric sensing is used [99], [100]. Recent introduction of MEMS and bioMEMS microfabrication techniques has enabled development of a series of miniaturized bladder monitoring devices. Petrican et al. designed an ultrasonic bladder volume monitor [101] whereas Rajagopalan et al. developed a polypyrrole-based (electronically conducting polymer) stretchable strain sensor that is wrapped around the bladder [102]. Volumetric response is recorded by monitoring the resistance of stretched strain sensor band. Most of the above methods require wired means of data collection and are not feasible for daily use. In terms of wireless monitoring of bladder volume, Wang et al. presented a micturition alert device consisting of a permanent bulk magnet sutured on the anterior bladder wall and a warning unit sutured on the inferior abdominal wall [103]. In-vivo results from dogs demonstrated its efficacy. Inspired by the aforementioned methods and combining our motivation in developing a device for IDC-related CUR management, we aim to develop an implantable system that offers both wireless magnetic monitoring of bladder volume and capability of active IDC-related CUR management.

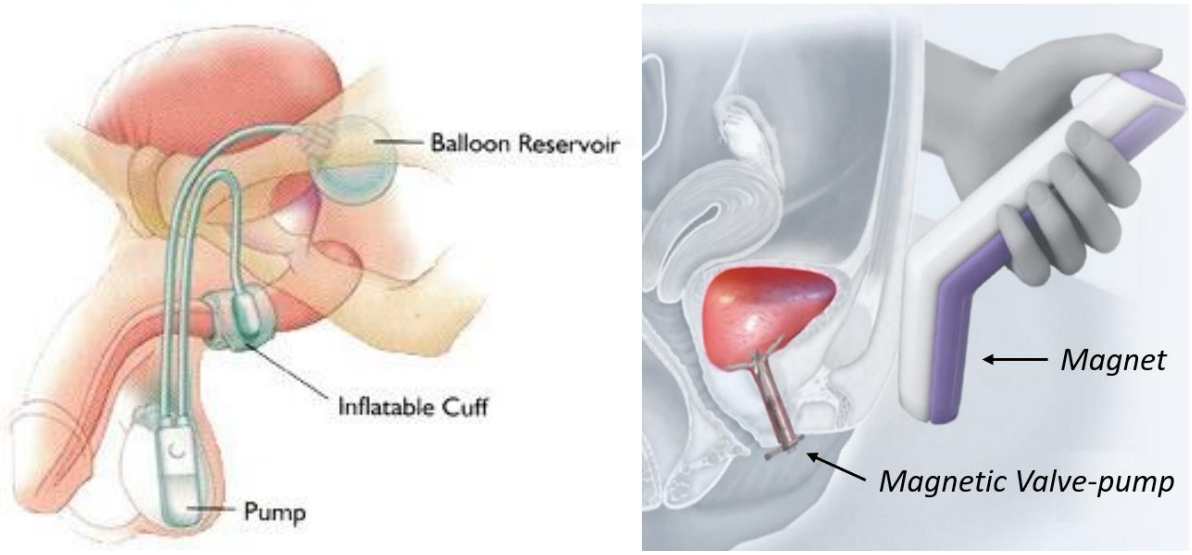

Figure 36. Recently developed devices for CUR management caused by sphincter deficiency. Left: AMS 800^{TM} Urinary Control System (Boston Scientific) restores continence among male patients using a pneumatic occlusive cuff wrapping around the urethra. Right: Vesiflo inFlow^{TM} takes advantage of the shorter urethra in female and designed a tubular magnetic valve-pump that can be inserted into the bladder through urethra. This magnetic valve-pump replaces the full functionality of sphincter muscle. It constantly blocks the urethra and an external magnetic actuator is used to drive the magnetic pump wirelessly during micturition.

3.1.4 Current strain gauge techniques

Current strain gauge techniques can be classified into three categories: resistive, fiber optic and capacitive. The resistive strain sensors consist of conductive materials such as metal, carbon nanotubes or liquid metal. Figure 37 shows examples of a flexible resistive strain sensor made from carbon nanotube on a bandage and another one made from liquid metal inside PDMS [104], [105]. Upon stretching, the conductive material undergoes deformation which is mainly elongation and have its resistance altered with the applied strain. Resistive strain sensors are generally low cost, easy to fabricate, and can be made flexible. However, they only have moderate sensitivity and the resistance that these sensors rely on are susceptible to environmental factors such as humidity and temperature. Additional hermetic sealing and temperature feedback components need to be designed for robust sensing performance. What's more, for reliable and repeatable strain measurements the resistive material cannot experience high strain values encountered in the aforementioned medical applications that alter the material's resistance irreversibly, limiting the sensors' dynamic range. For example, the polypyrrole-based resistive strain sensor presented in [102] has only a linear range within merely 20-40 %strain, opposing to normal bladder strain of about 100%. Lastly, resistive strain sensors often require subsequent circuitry to pick up the resistance dynamics and is unlikely to feasible for wireless strain measurements.

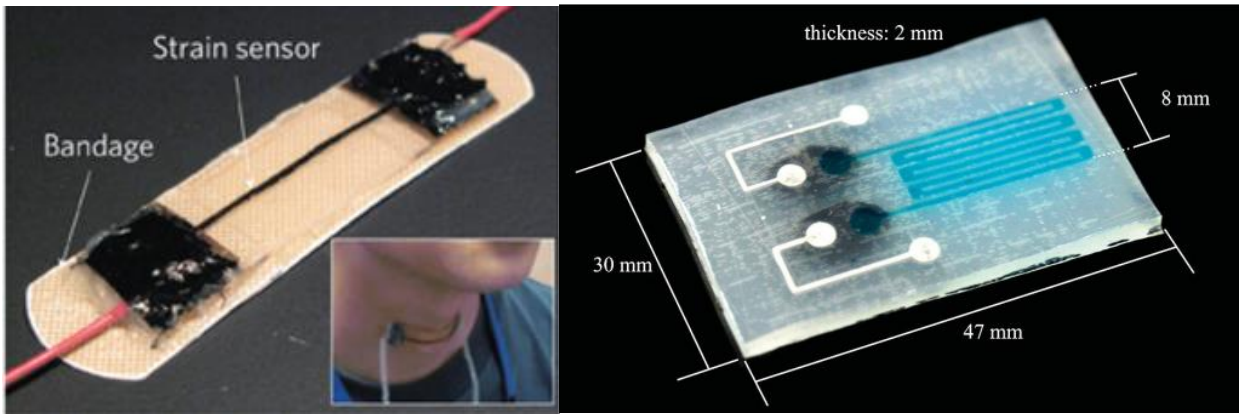

Figure 37. Examples of resistive strain sensors. Left: a flexible resistive strain sensor made from carbon nanotubes over a bandage [104]. A gel layer is applied over the black carbon nanotube region to protect it from mechanical damage. Right: a flexible resistive strain sensor comprising of serpentine microfluidic channels filled with conductive liquid metal [105]. The liquid is hermetically sealed within the channel to prevent leakage.

Fiber optic strain sensors measure strain by gauging the phase change of an emitted light beam attributed from the stretched optical path. They have good sensitivity, reliability and repeatability. On the other hand, the sensing system has to integrate bulky light source and has limited stretchability, leading to small sensing dynamic range. The capacitive strain sensors operate by sensing the capacitance variation stemmed from changes in geometry upon stretching. They have excellent sensitivity and high frequency response but have limited sensing range and are susceptible to electromagnetic noise. Figure 38 shows examples of a fiber optic strain sensor for dam structure strain sensing [106] and a capacitive strain sensor for bone strain monitoring during post-fracture healing [107]. Despite the distinct, even contradicting field of application in construction and human rehabilitation, very minor strains over rigid materials were measured in both scenarios. Overall, these common strain sensing techniques are ideal for small elongations and are not suitable for the large physiological strain monitoring applications introduced above.

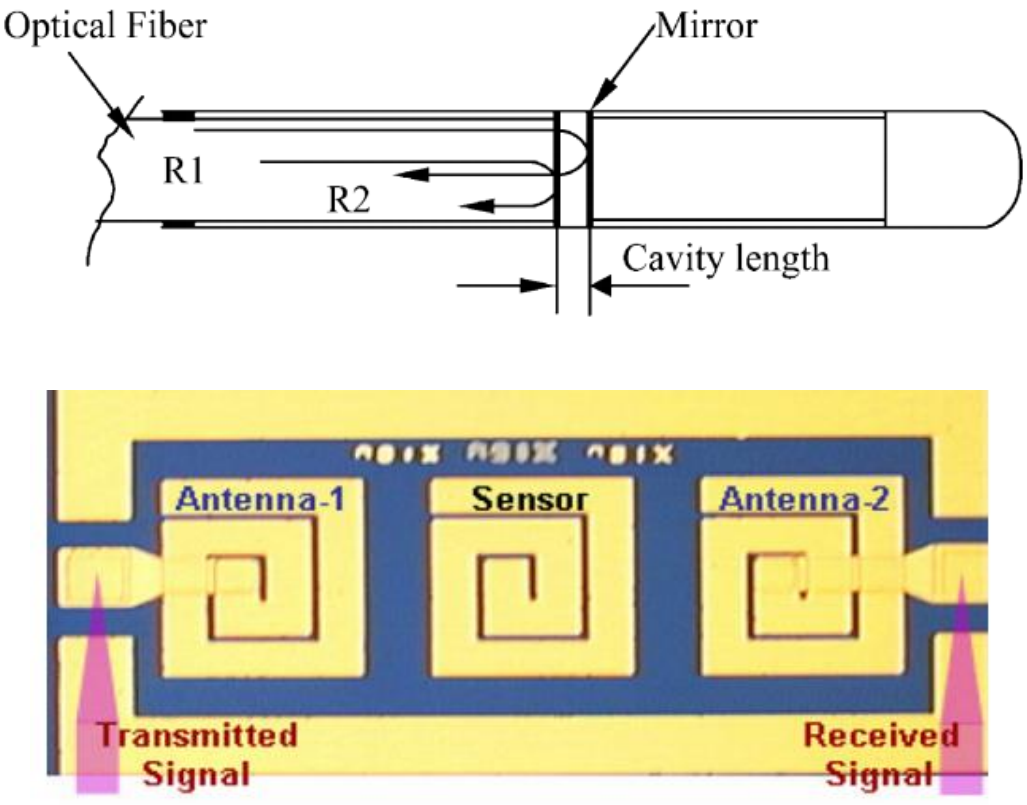

Figure 38. Examples of a fiber optic strain sensor [106] for dam structure strain sensing and a capacitive strain sensor for bone strain monitoring during post-fracture healing [107].

To overcome the limitations imbued in previous work toward chronic and large soft tissue strain monitoring, we present an implantable, passive magnetic strain sensing system with polymeric magnets that are laser-micromachined, re-magnetized and embedded into a carefully designed polydimethylsiloxane (PDMS) / Ecoflex® silicone composite band. The stiffer PDMS (elastic modulus 360–870 kPa) encapsulates the polymeric magnets while the softer Ecoflex® (elastic modulus 28.8 kPa) maintains the overall stretchability of the band. Algorithms for reliable wireless strain measurement is developed for various sensing modes. With such a configuration, this sensor is ideal as a monitor of chronic physiological complications such as congestive heart failure and bladder dysfunction.

3.2 Design Rationale

3.2.1 Impaired detrusor contractility (IDC) related chronic urinary retention (CUR)

To better design the desired system offering both wireless bladder monitoring and active management of IDC related CUR, the cause and basics of the underlying IDC problem must be scrutinized from a pathological perspective. Impaired detrusor contractility (IDC) refers to the problem of having underactive or acontractile detrusor. Underactive detrusor is defined as the detrusor with muscle that contracts in either inadequate magnitude or duration to empty the bladder completely without the presence of urethral symptoms, whereas an acontractile detrusor is defined as a bladder that cannot contract during urodynamic studies. A series of conditions, including neurogenic injuries, detrusor muscle damage, metabolic and myopathic disorders, may lead to IDC. Apart from the aforementioned diseases, a significant amount of IDC cases has been associated with the degeneration of detrusor functionality due to aging: the older the patients are, the weaker their muscles become. Madersbacher et al. conducted urodynamic studies among healthy elder population (age = 59 ± 16 years) who exhibit no disease related LUTS [108]. Exclusion criteria were outlined as acute and chronic urinary retention, urinary tract infection, medical therapies that inhibits neurogenic functionalities, and any previous surgery along the whole urinary tract. Urodynamic results showed a declining maximum urine flow rate with age and the deteriorating trend of other properties such as bladder capacity and prostate volume for males, resulting in an increase in residual urine volume. Intriguingly, the detrusor pressure at maximum flow remained the same within age groups between 40 and 80, implying a consistent muscle strength but fall short

in the detrusor's ability to maintain the same degree of contractility as before (i.e. smaller amount of bladder contraction under the identical detrusor pressure). Therefore, increasing the peak detrusor pressure may help mitigate other adverse effects on micturition and we will design the actuation operation based on this principle.

3.2.2 Operation theory

Figure 39 shows an illustration of the wireless bladder dysfunction monitoring system. The elastomeric strain sensor band is sutured/glued onto the surface of the bladder and strains/relaxes with the filling and emptying of bladder. The separation of embedded polymeric magnetic stripes induces a change in magnetic field which can be detected via an external magnetic sensor and interpreted as a signal of the bladder volume. The resulting change in magnetic field due to the applied strain can be picked up wirelessly by a smartphone from a distance comparable to human subcutaneous tissue thickness at lower abdomen.

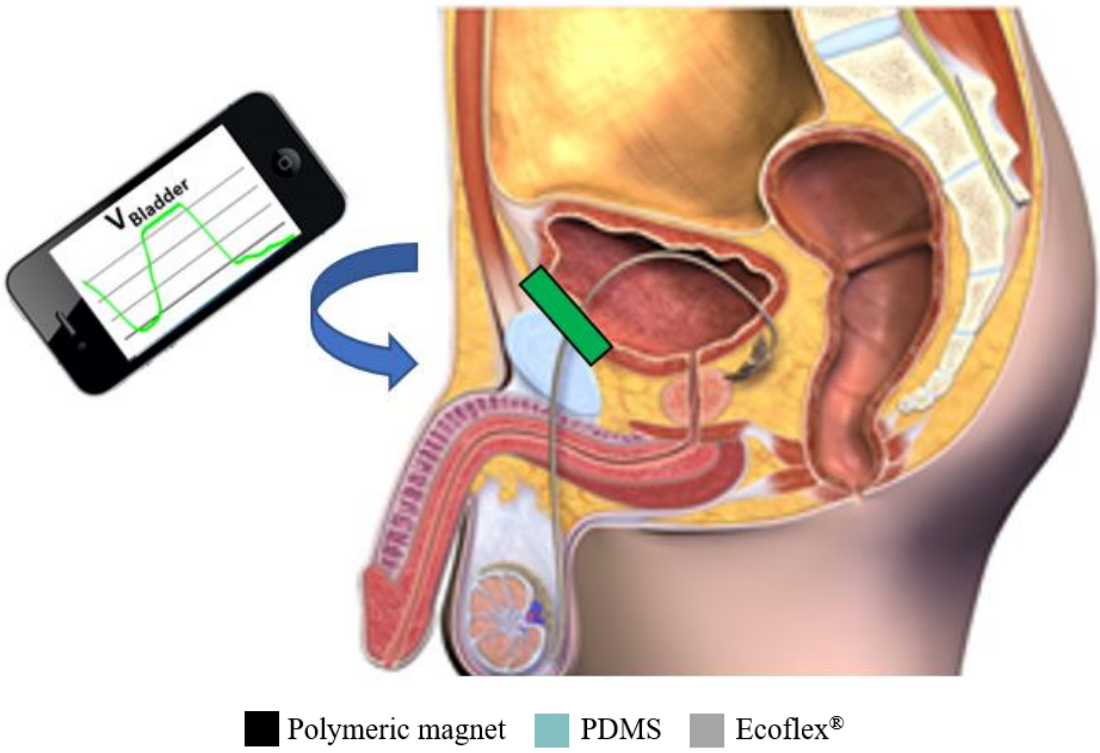

Figure 39. Schematic view of the wireless strain sensing system monitoring the strain of heart using a smartphone. Inset: enlarged view of the unique polymeric magnet/PDMS/Ecoflex® structure.

3.3 Fabrication

The fabrication of the elastomeric magnetic strain sensor band is illustrated in Figure 40. First, a commercial polymeric magnetic sheet, made from mixing polyvinyl chloride (PVC) binder with strontium ferrite ($SrFe_{12}O_{19}$, 0.5 mm thickness, Master Magnetics Inc., Castle Rock, CO, USA) or with neodymium-iron-boron particles (F65, 0.76 mm thickness, The Electrodyne Company, Inc., Batavia, OH, USA) is temporarily bonded onto a silicon wafer (for handling during fabrication) and is subsequently laser-cut into 10 mm × 2 mm stripes using a 10.6 µm CO_2 laser (Universal Laser Systems, Scottsdale, AZ, USA), Figure 40a (wafer not shown). Excessive magnetic regions are removed and the stripes are cleaned with IPA, Figure 40b. Next, a 1 mm PDMS layer (Sylgard184, Dow Corning, 10:1) is casted on the sheet, Figure 40c. The polymeric magnet / PDMS double layer is then flipped, and another 0.5 mm PDMS layer is casted on top, completely encapsulating the polymeric magnetic stripes, Figure 40d. Once fully crosslinked, the PDMS layer is laser patterned into 0.5 mm thick encapsulations around each magnetic stripe, Figure 40e. Then, a 1 mm Ecoflex® layer (0010, Smooth-On Inc., 1:1) is casted on both sides, filling the gap between polymeric magnet / PDMS isles and forming the stretchable regions, Figure 40f, g. Lastly the elastomeric band is released from the wafer and is magnetized in a vertical magnetic field from a neodymium permanent magnet (K&J Magnets, flux density B ≈ 1 T) for 1 minute, Figure 40h.

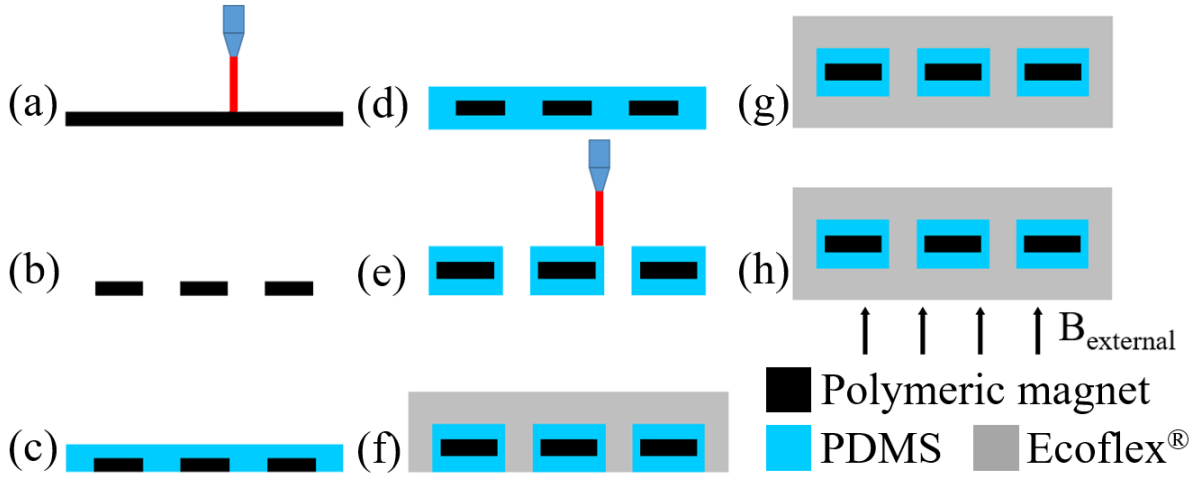

Figure 40. Fabrication process of the magnetic strain sensor. (a-b) Laser cut magnetic sheet into islands; (c-d) encapsulate stripes in PDMS; (e-g) laser machine into PDMS-magnet islands and encapsulate with Ecoflex®; (h) re-magnetize the band.

An exemplary of the fabricated magnetic strain sensor band and the visualization of different material sections is displayed in Figure 41. The band design shown has a separation of 6 mm between the black magnetic strips. Parts of the band made from different materials are color-coded as: black for polymeric magnetic strips, blue for PDMS cases, and red for Ecoflex® interconnections.

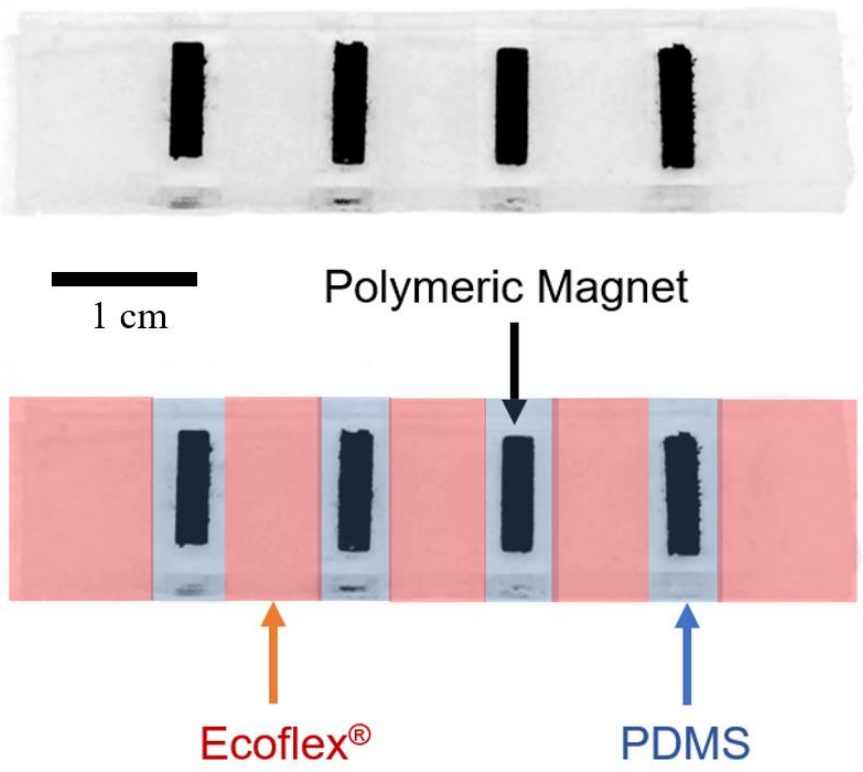

Figure 41. An exemplary image the fabricated magnetic strain sensor band and the visualization of different material sections. The band design shown has a separation of 6 mm between the black magnetic strips. Parts of the band made from different materials are color-coded as: black for polymeric magnetic strips, blue for PDMS cases, and red for Ecoflex® interconnections. The scale bar indicates 1 cm for both bands.

No fabrication or assembly of magnetic sensors is necessary for this wireless magnetic strain sensing system as we take advantage of the magnetic sensor already on board of a smartphone. We selected an iPhone 6 (Apple Inc., Cupertino, CA, USA) as the magnetic sensing unit but it can be replaced by any smartphone carrying a magnetic sensor with proper sensing system recalibration.

3.4 Experiment Setup and Methods

3.4.1 Mechanical and magnetic characterization

Effective elastic modulus of the fabricated elastomeric strain sensor bands with various designs was measured by a mechanical characterization station (MTESTQuattro, ADMET, Norwood, MA, USA). Geometric dependency of the sensor's effective elastic modulus is then modeled in MATLAB (MathWorks, Natick, MA, USA) and compared against the measured results.

The effectiveness of the dual silicone composite design adopted in the elastomeric strain sensor bands was validated by stretching sensor bands made of pure PDMS, pure Ecoflex®, and the dual PDMS/Ecoflex® composite on a manipulator platform. Maximum elongation when the band tears or the polymeric magnetic strips delaminate from the silicone cases was recorded.

Magnetic properties of the embedded polymeric magnetic strips were characterized in terms of their remanence (B_r), coercivity (H_c), and relative permeability (μ_r). The magnetic hysteresis loop of the polarized polymeric magnetic strips was measured by a superconducting quantum interference device (MPMS®3 SQUID, Quantum Design Inc., San Diego, CA, USA). Remanence (B_r) and relative permeability (μ_r) extracted from the hysteresis loop were then used for magneto-static finite element analysis (COMSOL Multiphysics, Burlington, MA, USA).

3.4.2 Wireless magnetic strain sensing system calibration, validation, and experiments

Sensing System Calibration PDMS/Ecoflex® composite strain sensors with separation of 4 mm, 6 mm and 8 mm between polymeric magnetic strips were placed horizontally and stretched to various strains on an automated actuator (MTESTQuattro, ADMET, Norwood, MA, USA). The magnetic field-strain data was recorded by an AK8963 3-axis GMR magnetic sensor (Asahi Kasei, Tokyo, Japan) on board of an iPhone 6 (Apple Inc., Cupertino, CA, USA) from 2.5 cm away, a distance close to average chest wall thickness [109], via a magnetometer sensor log application (REGREX Co., Ltd.). The resolution of the Hall Effect sensor is 1.67 LSB/μT in 14-bit mode and 6.67 LSB/μT in 16-bit mode. The sensor's sampling rate can be configured into 10 Hz or 100 Hz. In our experiments 16-bit mode and 10 Hz sampling rate was selected. The position of the magnetic sensor in the interior of the iPhone 6 is 2.0 cm from the top and 1.5 cm from the right edge, Figure 42 [110]. The physical region of the magnetic sensor was right above the center of the strain sensor

during measurements. Extra cautions were taken to ensure that no magnetic source or ferrite material that may distort magnetic field was in vicinity of the setup. Figure 43 illustrates the experiment setup for sensing system calibration with the sensing direction labeled in Cartesian coordinates. All structures and frames were made of acrylic, aluminum, or copper.

Figure 42. Position of magnetic sensor in iPhone 6 [110]

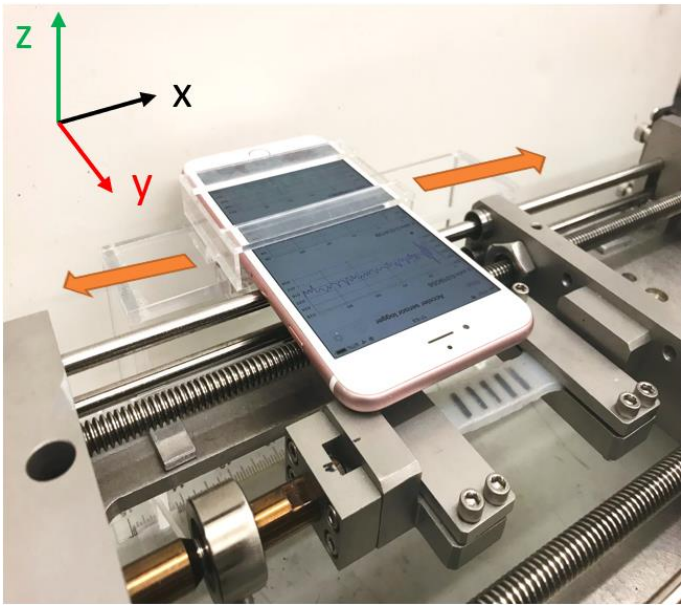

Figure 43. Experiment setup for sensing system calibration with sensing directions labeled in Cartesian coordinates. All structures and frames were made of acrylic, aluminum, or copper.

Scanning Mode Experiments Finite element analysis for the feasibility of scanning mode as well as alternating polarization of magnetic strips was conducted with COMSOL Multiphysics. Remanence (B_r) and relative permeability (μ_r) extracted from the hysteresis loop during magnetic characterization were passed into magneto-static simulations.

To validate the efficacy of alternating the polarization of magnetic strips, sensor bands with magnetic strips polarized in the same direction and in alternating directions were tested under the identical setup. The band design with 8 mm inter-strip separation was selected for validation since it's the design with the best sensing range but the least sensitivity. Measurements were taken at 40 mm above the center of the band.

Sensor bands embedding 10 mm × 2 mm stripes with 4mm, 6 mm and 8 mm inter-strip separations were used for scanning mode strain measurements over planar and curved surfaces. For scanning mode measurements over planar surfaces, the same setup as in Figure 43 was used and the smartphone, along with the on-board magnetic sensor, could move along the x axis for scanning over the magnetic sensor band. For scanning mode measurements over curved surfaces, the same smartphone scanning platform was utilized and the sensor band was adhered to a latex balloon filled with 50 ml of water, approximating a bladder with some residual urine. Figure 44 demonstrates the experiment setup for scanning mode measurements over curved surfaces. In both experiments, another actuator drove the smartphone scanning motion at a constant speed of 2 cm/s while the magnetometer measurements were recorded. The acquired transient data ($\vec{\boldsymbol{B}}_x$, $\vec{\boldsymbol{B}}_y$, $\vec{\boldsymbol{B}}_z$, t) are converted into spatial data ($\vec{\boldsymbol{B}}_x$, $\vec{\boldsymbol{B}}_y$, $\vec{\boldsymbol{B}}_z$, x) by multiplying the fixed scan rate (2 cm/s) with the reciprocal of sampling frequency (10 Hz).

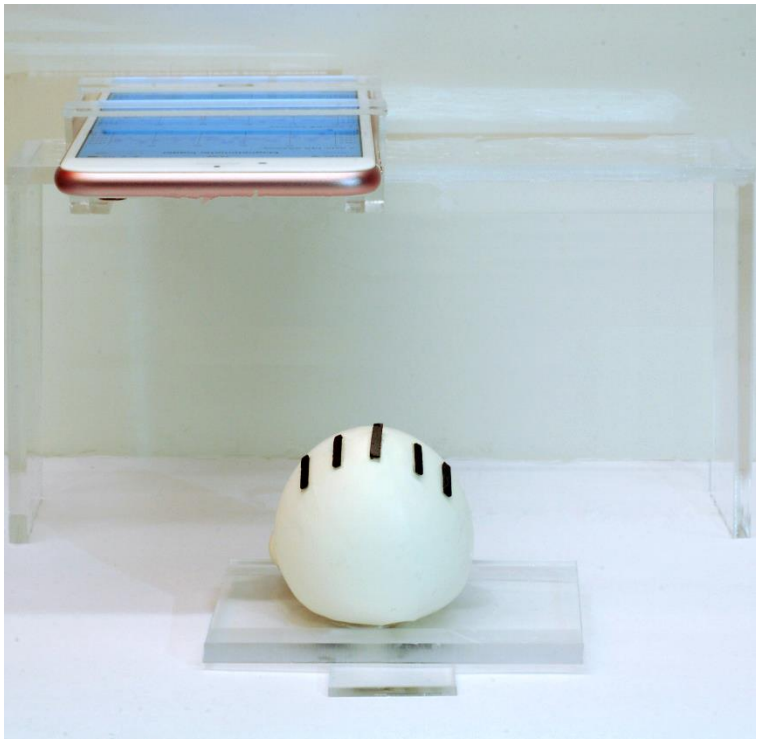

Figure 44. Experiment setup for scanning mode measurements over curved surfaces.

Durability Test The same automated actuator was used to test the long-term durability of the sensing system. Sensor bands were soaked in 37℃ PBS and stretched horizontally by the actuator from 0% to 80% strain periodically at a rate of 6 s/period. Although a strain rate close to that of the cardiac cycle was desired, this was the maximum actuation rate achievable with the available actuator and the test underwent 1600 cycles. Both the magnetic field measured from the smartphone and the mechanical tension on the sensor band were recorded. Such long-term durability test would verify both the mechanical durability and the magnetic stability of the sensing system.

Actuation Mode Experiments Sensor bands with 4mm, 6 mm and 8 mm inter-strip separations were tested under actuation mode. In addition, bands made from neodymium-iron-boron (NdFeB) polymeric magnetic strips were included in the actuation experiment as neodymium-iron-boron has stronger remanence (0.55 T) [111] than strontium ferrites, leading to greater force exerted on bladder.

First, the amount of magnetic force the sensor band can exert with respect to actuation distance were characterized. A schematic of the characterization setup is shown in Figure 45. The sensor band was placed on a high-precision digital milligram scale (0.01g precision, SW-GEM50, Smart Weigh Co. Ltd.) and an NdFeB magnet block was placed beneath the scale as the actuation source. Note that the placement of NdFeB magnet did not interfere scale measurements. The actuation distance, ranging from 27 mm to 47 mm, was modulated by inserting 3 mm or 6 mm acrylic sheets between the scale and the magnet. The scale reading less the self-weight of the sensor band was recorded as the amount of magnetic attraction force at the corresponding actuation distance.

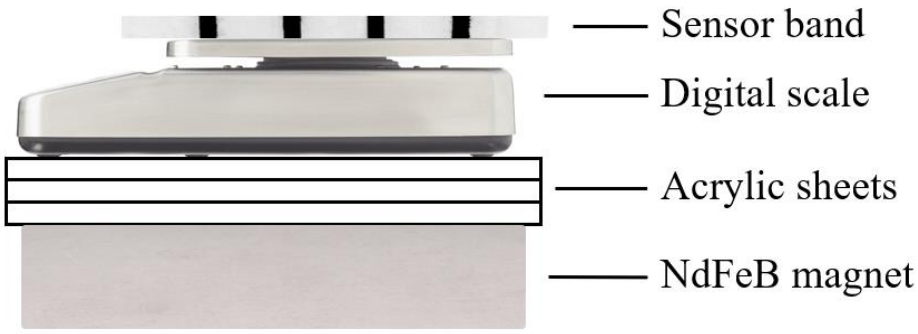

Figure 45. Setup of the actuation characterization experiment. The sensor band was placed on a high-precision digital milligram scale and an NdFeB magnet block was placed beneath the scale as the actuation source. The actuation distance was modulated by inserting 3 mm or 6 mm acrylic sheets between the scale and the magnet.

Then an in-vitro experiment was conducted to demonstrate the effectiveness of sensor band actuation on alleviating urinary retention. A rubber tube with 3 mm inner diameter was inserted into a latex balloon to approximate the bladder-urethra system. The balloon was filled with 75 ml water and the sensor band was adhered to the balloon. An NdFeB magnet block was placed behind the balloon so that the total separation between the magnet and the band reached 40 mm, a distance equivalent to subcutaneous adipose tissue thickness [112]. One end of the rubber tube was inserted into a measuring cylinder and was sealed before the experiment commenced. Figure 46 illustrates the setup for this in-vitro sensor band actuation experiment. Upon the start of the experiment, the seal was opened and a video was recorded until fluid ceased flowing into the measuring cylinder.

Video analysis was then performed to extract the amount of fluid outflow over time and the volume of residual fluid.

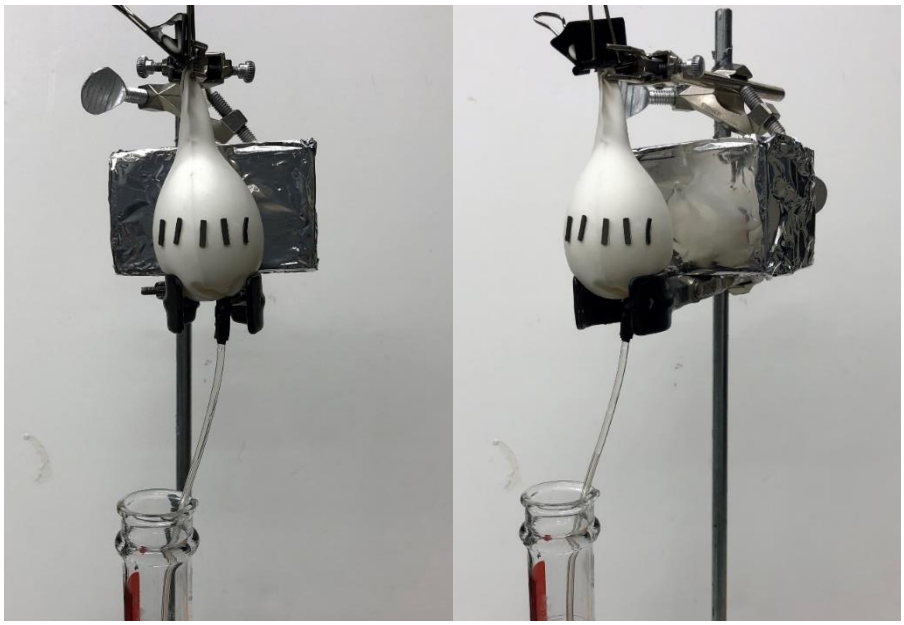

Figure 46. Front and side view of the setup for in-vitro sensor band actuation experiment.

3.5 Results and discussion

3.5.1 Mechanical characterization

Three strain sensor bands with identical dimensions but different separation between magnetic stripes (4 mm, 6 mm and 8 mm) were characterized for their mechanical properties, Figure 47a. Another two 6 mm strain sensors made from pure PDMS and pure Ecoflex® were used to justify the dual silicone band design, Figure 47b. Under the identical strain of 80%, sensor made from pure Ecoflex® (elastic modulus 27.4 kPa) undergo magnet/Ecoflex® delamination while sensor made from pure PDMS (elastic modulus 870 kPa) ruptured. The stiffer PDMS acts as a trap for magnetic stripe, fixing it in place despite poor bonding along the interface. The softer Ecoflex® acts as the stretchable interconnections between each PDMS isle, keeping the entire band nearly as stretchable as pure Ecoflex® band. The similar silicone composition of Ecoflex® and PDMS ensures tight bonding at their junction/interface that eliminates potential delamination. Figure 48 gives a more detailed view of the delamination effect observed in pure Ecoflex® bands and the intact structure in dual silicone bands under the same strain. Naserifar et al. [113] conducted finite

element analysis and experimental characterization on a similar design that utilizes material gradients.

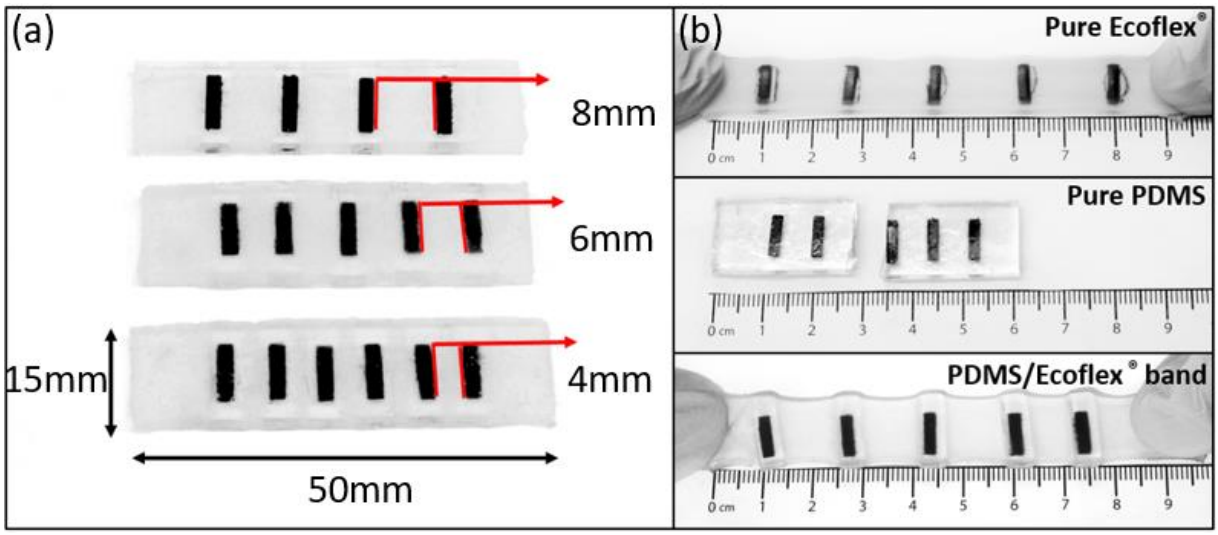

Figure 47. (a) optical image of the fabricated strain sensors with 4mm, 6mm and 8mm separation between polymeric magnets, (b) under 90%strain, pure Ecoflex® sensor underwent magnet/Ecoflex® delamination (top); pure PDMS sensor ruptured (middle); the dual silicone sensor functioned normally (bottom), separation between the magnetic stripes is 6mm in all three bands of different material.

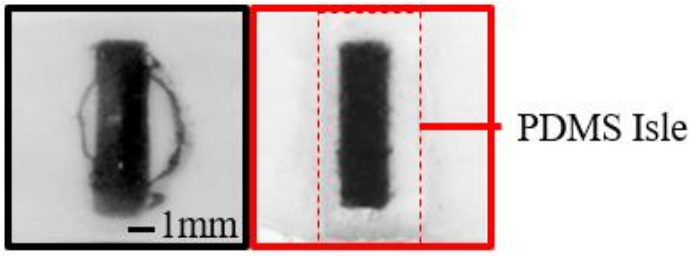

Figure 48. Detailed view of the delamination effect observed in pure Ecoflex® bands and the intact structure in dual silicone bands under the same strain.

Upon adjusting geometry parameters of the sensor band during design phase, it is beneficial if some quantitative idea of the design's effective Young's modulus mathematically before fabrication and mechanical characterization, providing design guidelines from a mechanical aspect. Geometry parameters are defined as number of magnetic strips *N*, inter-strip separation *d* in mm (including 0.5 mm PDMS encapsulation), length of stretchable ends *a* in mm. Width of each

magnetic strip is fixed at 2 mm. Figure 49 illustrates how each parameter is defined on a sensor band.

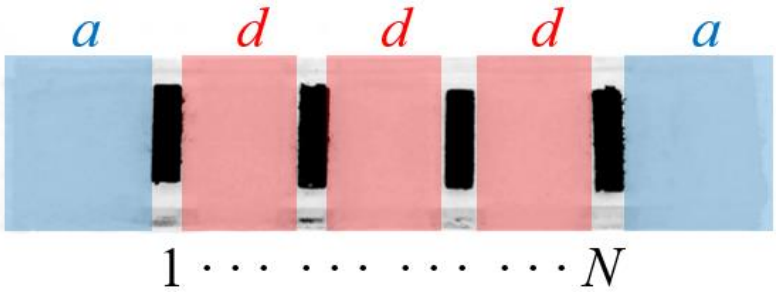

Figure 49. Definition of geometric design parameters of a sensor band.

The effective Young's modulus E_{eff} of a material is defined as the ratio of the stress σ_{band} experienced to the strain ε_{band} stretched to:

$$E_{eff} = \frac{\sigma_{band}}{\varepsilon_{band}} \quad (12)$$

where stress σ_{band} is in kPa and strain ε_{band} is defined as the amount of elongation ΔL divided by the original length of the material L:

$$\varepsilon_{band} = \frac{\Delta L}{L} \quad (13)$$

With absence of any stretching, the sensor band remains in its original length:

$$L = 2(a + N) + d(N - 1) \quad (14)$$

Upon stretching, we assume that only Ecoflex® interconnection regions undergo significant elongation as the mismatch of the Young's modulus between PDMS and Ecoflex® is tremendous (E_{PDMS} = 870 kPa >> $E_{Ecoflex}$ = 28.8 kPa). Considering the PDMS isles and magnetic strips as rigid body, the stress experienced by the sensor band can only be attributed from the stretched Ecoflex® region:

$$\sigma_{band} = \sigma_{Ecoflex} = E_{Ecoflex}\varepsilon_{Ecoflex} \quad (15)$$

The total stretchable Ecoflex® region has a length of:

$$L_{Ecoflex} = L - 3N = 2a - N + d(N-1) \quad (16)$$

The relation between the strain of the Ecoflex® region $\varepsilon_{Ecoflex}$ and that of the whole band ε_{band} can be expressed as:

$$\varepsilon_{Ecoflex} = \frac{\Delta L}{L_{Ecoflex}} = \frac{\Delta L}{L}\frac{L}{L_{Ecoflex}} = \varepsilon_{band}\frac{L}{L_{Ecoflex}} \quad (17)$$

Plugging Equations $L = 2(a+N) + d(N-1)$ (14)-

R

E

F

$$E_{eff} = \frac{\sigma_{band}}{\varepsilon_{band}} = \frac{E_{Ecoflex}\varepsilon_{Ecoflex}}{\varepsilon_{band}} = \frac{E_{Ecoflex}\varepsilon_{band}}{\varepsilon_{band}}\frac{L}{L_{Ecoflex}} = 28.8\left[1 + \frac{3}{(d-1) + {}^{(2a-d)}/_{N}}\right]kPa \quad (18)$$

Thus, we have derived a computational representation of the relationship between geometric design parameters and the effective Young's modulus of the PDMS/ Ecoflex® composite sensor band. Figure 50 contains a plot reflecting the relationship between geometric design parameters and effective Young's Modulus of the sensor band. Each curve represents a sensor band design with different inter-strip separation and all fabricated sensor bands have the number of strips *N*=5, and the length of stretchable ends *a*=4 mm. From the curve an estimation of the Young's modulus of the sensor bands is approximately 57 kPa for 4 mm design, 45 kPa for 6 mm design, and 39 kPa for 8 mm design. Young's modulus obtained from the measurements of sensor bands yield similar results of 56.0 kPa for 4 mm design, 45.1 kPa for 6 mm design, and 39.9 kPa for 8 mm design, which coincide well with the theoretical values. Therefore, we believe the derived relation is rather accurate and can provide non-trivial guidelines for sensor band design from a mechanical aspect.

\

h

LEcoflex=L−3N=2a−N+d(N−1) (16) into $Eeff = \sigma band \varepsilon band$

(12), the effective Young's modulus of the sensor band becomes:

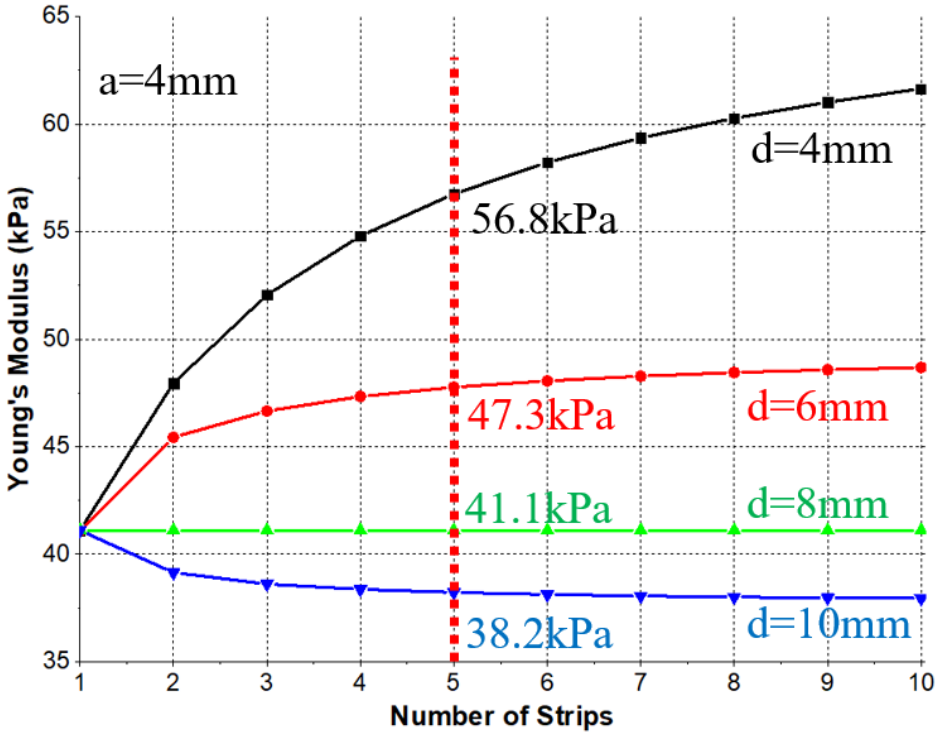

Figure 50. Plot reflecting the relationship between geometric design parameters and effective Young's Modulus of the sensor band. Each curve represents a sensor band design with different inter-strip separation and all fabricated sensor bands have the number of strips N=5 and the length of stretchable ends a=4 mm. Effective elastic modulus

Mechanical stress vs. strain measurements of the fabricated sensor bands indicate effective Young's moduli of 56.0 kPa for 4 mm design, 45.1 kPa for 6 mm design, and 39.9 kPa for 8 mm design, Figure 51. All fabricated sensor bands have the number of strips N = 5 and length of stretchable ends a = 4 mm Figure 49. This verifies our hypothesis that the incremental addition of extra Ecoflex® interconnection material provides more stretchable regions, reducing the effective elastic moduli of the fabricated bands. Maximum elongation at break is about 80% for 4 mm design, 100% for 6 mm design, and 120% for 8 mm design.

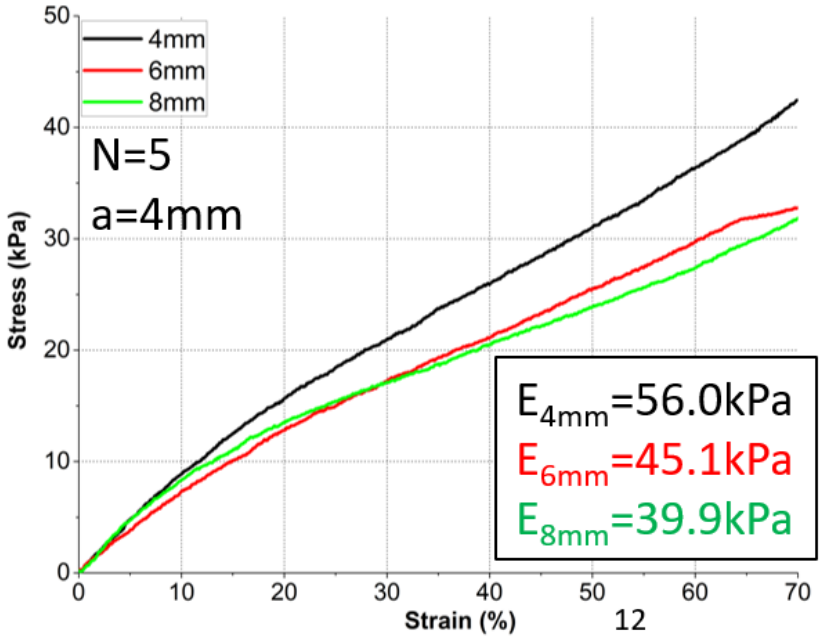

Figure 51. Stress vs. strain measurements of fabricated sensor bands. Results indicate an elastic modulus of 56.0 kPa for 4 mm design, 45.1 kPa for 6 mm design, and 39.9 kPa for 8 mm design. All fabricated sensor bands have the number of strips N = 5 and length of stretchable ends a = 4 mm.

3.5.2 Magnetic characterization

When acquired from the vendor, the polymeric magnetic sheet was originally magnetized in the Halbach array configuration. Halbach array, designed for augmenting the magnetic field on one side while canceling the field to near zero on the other side, is a spatially rotating pattern of magnetization, Figure 52a. Seemingly ideal for the purpose of maximizing induced magnetic field, however, the Halbach array strengthens the near-field magnetic field by redirecting most of the magnetic field lines that should have extended deeply into space, weakening the far-field magnetic field. In other words, magnets with Halbach array polarization are optimal for applications such as magnetic clamps or refrigerator magnets, where magnetic adhesion or attraction is required, but are not feasible for applications such as the intended heart failure or bladder dysfunction monitoring, where higher far-field magnetic intensity is desired. Applying a strong vertical magnetic field will re-align the magnetic domains and strengthen the far-field magnetic field, Figure 52b.

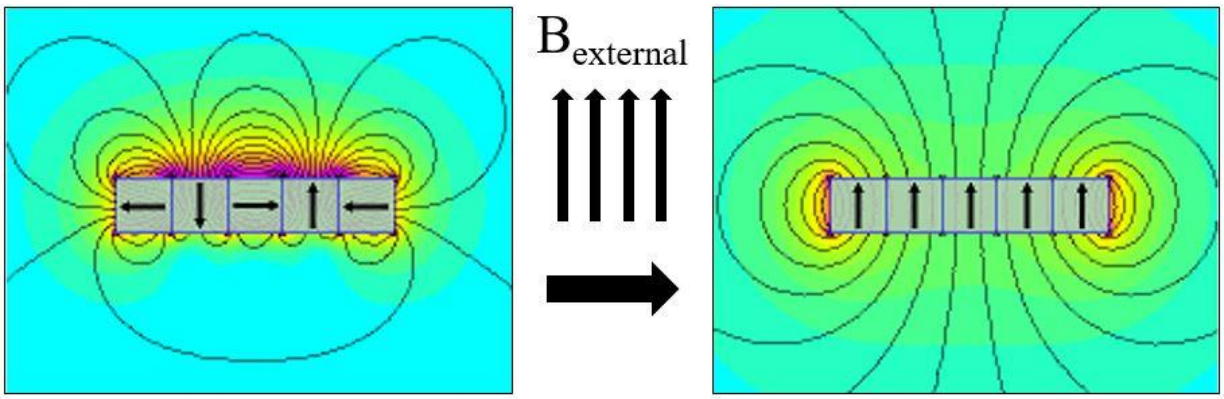

Figure 52. Magnetization and induced magnetic field in (a) Halbach array configuration, (b) uniform vertical configuration after exposed to a strong external magnetic field. Blue box indicates the unit cell of magnetization and the arrow indicates the direction of magnetization. [114]

Magnetic property characterization is crucial to understanding the polymeric magnet's behavior after magnetization. Figure 53 shows the obtained magnetic hysteresis loop with vertical external field sweeping from H = -80×10^4 A/m (B ≈ -1 T) to 80×10^4 A/m (1 T). Remanence (B_r) is equal to the y-intercept value and the magnetic coercivity (H_c) is equal to the x-intercept value. Relative permeability (μ_r) is equal to the slope of the tangent line near the magnetic intensity comparable to that inside human body (H = -10^4A/m to 10^4A/m) divided by the permeability of air (μ_0). Material datasheet from the Electrodyne Inc. stated magnetic properties of NdFeB magnetic strips as and no repeating magnetic characterization was performed. A summary of magnetic properties of strontium ferrite polymer magnet, obtained from hysteresis loop, and that of NdFeB polymer magnet, cited from datasheet [111], is manifested in Table 12.

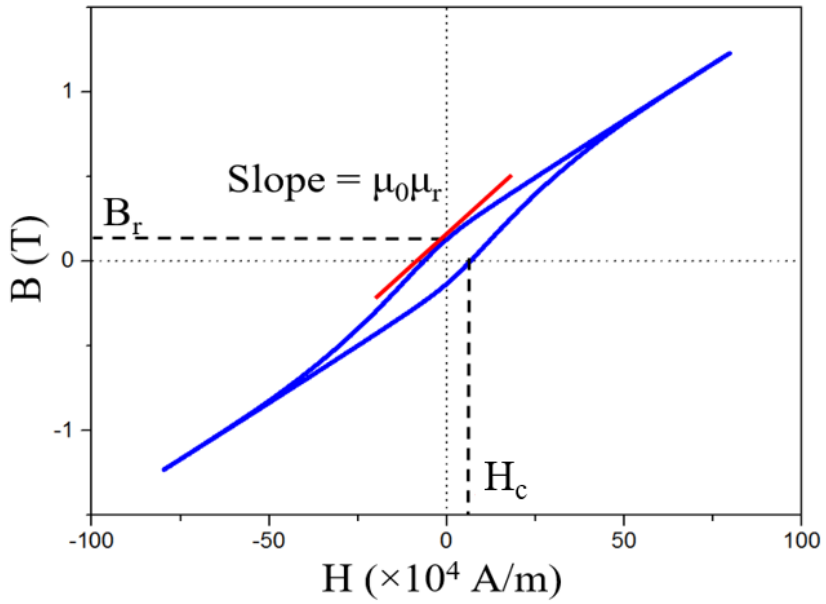

Figure 53. Magnetic hysteresis loop with external magnetic field sweeping from H = -80×10^4 A/m to H = 80×10^4 A/m. Remanence (B_r) and magnetic coercivity (H_c) are indicated by the y-intercept and x-intercept of the loop, respectively. Slope of the tangent line at H = 0 indicates the magnetic permeability ($\mu_r\mu_0$) when external field is removed.

Table 12. Magnetic parameters obtained from hysteresis loop and from datasheet

Name	**Symbol**	**$SrFe_{12}O_{19}$**	**NdFeB**	**Unit**
Remanence	B_r	0.131	0.55	T
Coercivity	H_c	1.5×10^5	3.9×10^5	A/m
Relative Permeability	μ_r	1.46	1.15	–

Figure 54 shows the finite element analysis of magnetic flux density induced by a 4 mm-separation strain sensor at various strains. The color map indicates the base 10 logarithms of the magnitude of magnetic flux density ($\log_{10}|\vec{\boldsymbol{B}}|$) while the arrow indicates the direction of flux density vector ($\vec{\boldsymbol{B}}$). The initial separation between each magnetic stripe is 4 mm and the sensor band is then stretched to 40 %strain and 80 %strain. At 0 %strain the magnetic field of each stripe overlaps and adds up to a strong magnetic field, reaching 50 μT at 2.5 cm distance away, Figure 54a. At 40 %strain, the magnetic field of each stripe starts to separate and the resultant magnetic

field at 2.5 cm drops to 25 μT, Figure 54b. At 80 %strain the magnetic field drops further to below 10 μT at 2.5 cm distance, Figure 54c.

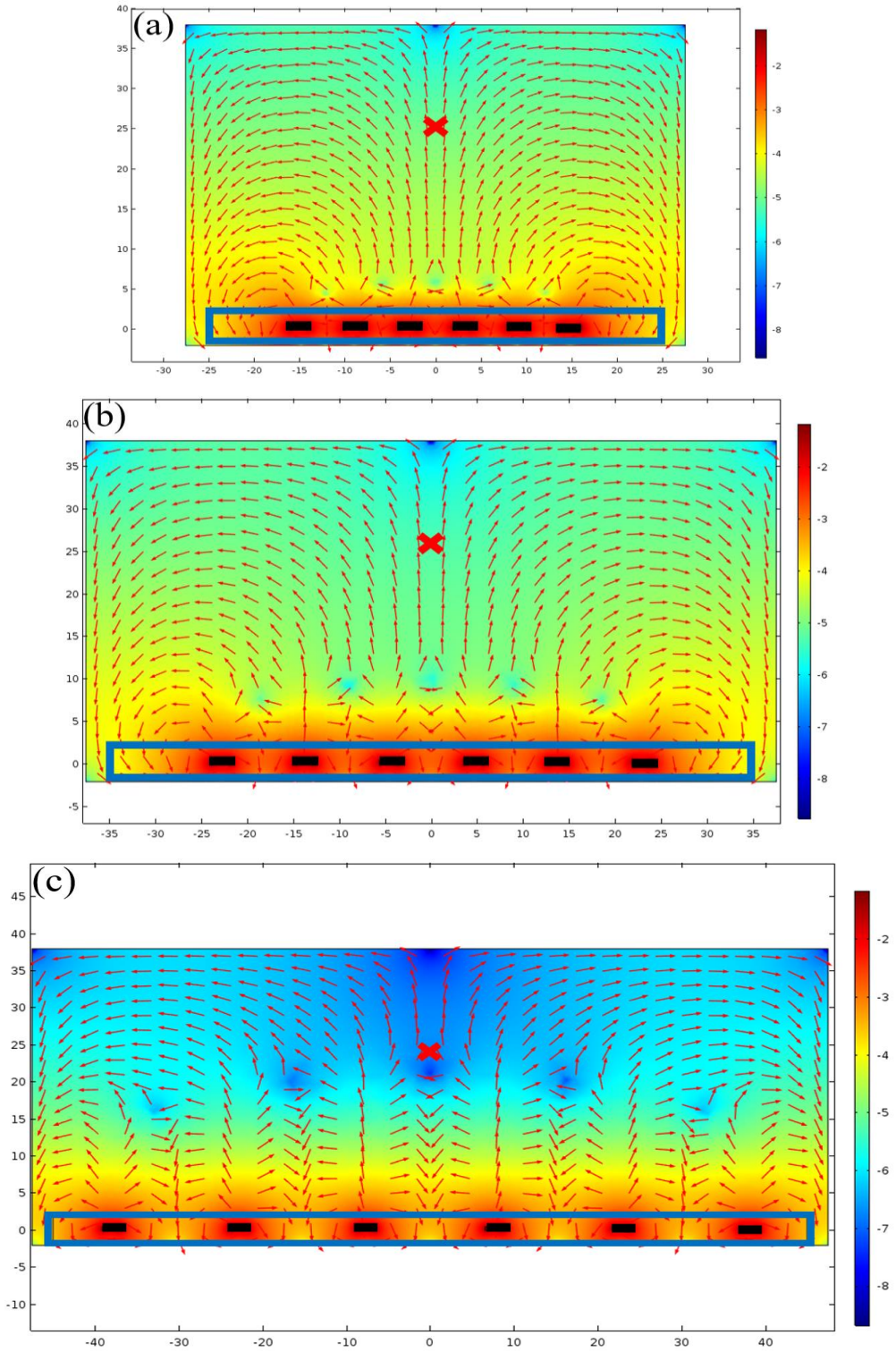

Figure 54. Magneto-static finite element analysis of a strain sensor at (a) 0 %strain, (b) 40 %strain and (c) 80 %strain. The red 'x' indicates the position of the sensor. The blue boxes are the sensor bands and the black boxes are the magnetic stripes. The color map indicates base 10 logarithmic of the magnitude of magnetic flux density ($\log_{10}|\vec{\boldsymbol{B}}|$) while the arrow indicates the direction of flux density vector ($\vec{\boldsymbol{B}}$). Scale bar for the color map has a unit of T and the xy coordinates have a unit of mm.

3.5.3 Sensor calibration and strain measurements under cardiac conditions

Sensors with 4 mm separation between magnetic strips exhibit the best sensitivity (1.13 µT / 10 %strain) thanks to denser magnetic stripe distribution but the least strain range (80 %strain) due to shorter stretchable Ecoflex® regions, Figure 55. For sensors with greater initial separation between magnetic stripes (6 mm, 8 mm), their maximum strain increases (100 %strain, 120 %strain), accompanied by a decrease in induced magnetic field and strain sensitivity (0.98 µT / 10 %strain, 0.85 µT/ 10 %strain). The background magnetic flux density is around 55 µT. The strain sensor was able to monitor strain and heart rate within ranges relevant to cardiac cycle (40–60 %strain, 60–100 bpm), Figure 56a, b [115].

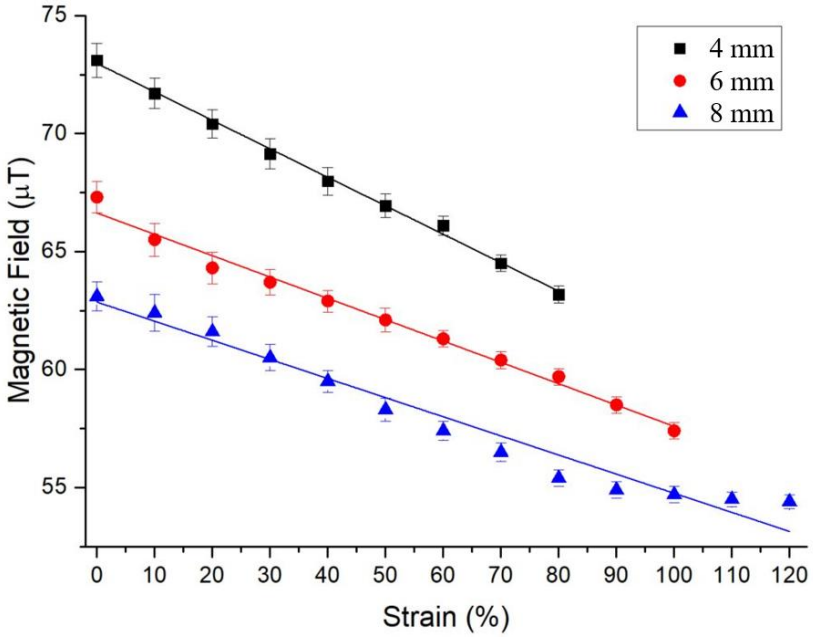

Figure 55. Magnetic field vs. strain calibration for the three sensor designs.

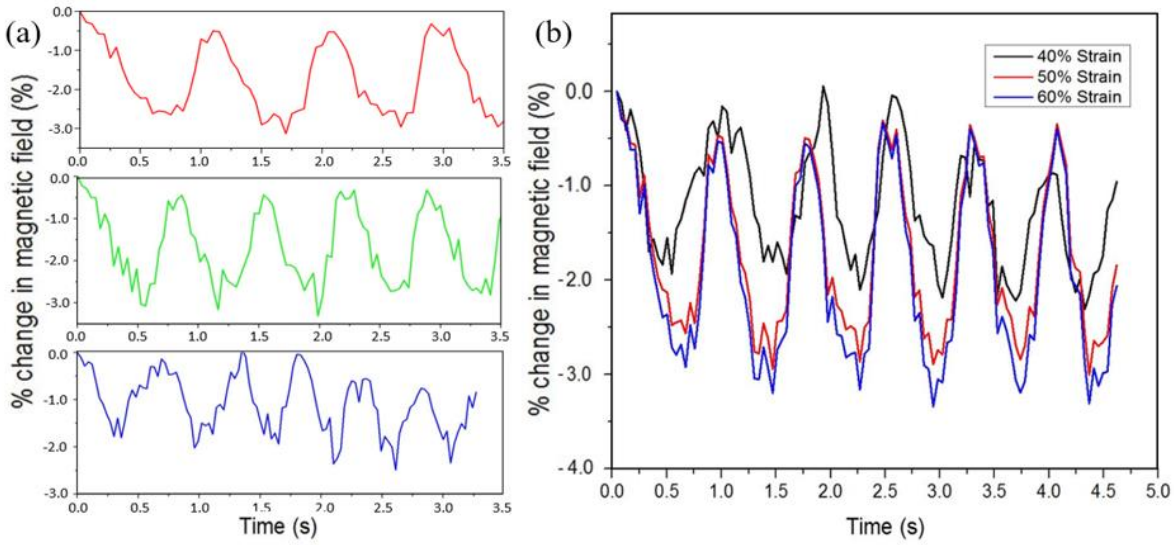

Figure 56. Response of a 4 mm sensor to simulate cardiac cycle conditions: (a) transient response of % change in magnetic field under normal strain of heart (50 %) but at a strain rate equivalent to 60 bpm (red), 80 bpm (green) and 100 bpm (blue), (b) transient response of % change in magnetic field under various strains at a rate of 75 bpm.

3.5.4 Biocompatibility

Materials used for this implantable strain sensor include PDMS, Ecoflex® and polymeric magnet (strontium ferrite with PVC binder). Both PDMS and Ecoflex® are nontoxic and biocompatible [116]. Strontium ferrite appears to be between 'harmful' and 'nontoxic' for aquatic organisms [82]. However, its cytotoxicity and biocompatibility for human are not well established. Industrial grade PVC binder inside polymeric magnet is not biocompatible but can be replaced with biocompatible medical grade PVC or polyethylene (PE) [117].

3.5.5 Scanning mode experiments

Scanning mode for planar strain sensing Figure 57 illustrates the scanning mode simulation for planar strain sensing in COMSOL Multiphysics. The magnetic sensor traverses 15 mm above a 4 mm design sensor band stretched to 20 %strain and the magnetic flux density $\left|\vec{\boldsymbol{B}}(x)\right|$ at each horizontal position x is computed, Figure 57 top. A representative result of the finite element analysis plotting the computed $\left|\vec{\boldsymbol{B}}\right|$ in horizontal (x) and vertical directions (z) is shown in Figure 57 bottom. The magnetic strips of the band in the top graph is aligned with the peaks of the computed vertical magnetic field $\left|\vec{\boldsymbol{B}}_z\right|$ (green curve). The peaks of the green curve are salient and

evenly spaced, matching the position of the magnetic strips in the band geometry. Since the horizontal position of the magnetic strips is determined only from the signal pattern acquired, results are independent to the height of sensor scanning as long as the peak patterns persist. Such alignment indicates, theoretically, promising feasibility of scanning mode for planar strain sensing. The relative location of the peaks can be computed with a simple peak-detection algorithm. Single-strain measurements can be computed from the peak-to-peak distance, which is the separation between adjacent magnetic strips and the final strain measurement would be the arithmetic mean of all single-strain measurements. Benefiting from the multi-strip sensor band design and the measurement-averaging method, the measurement error of the system is greatly reduced.

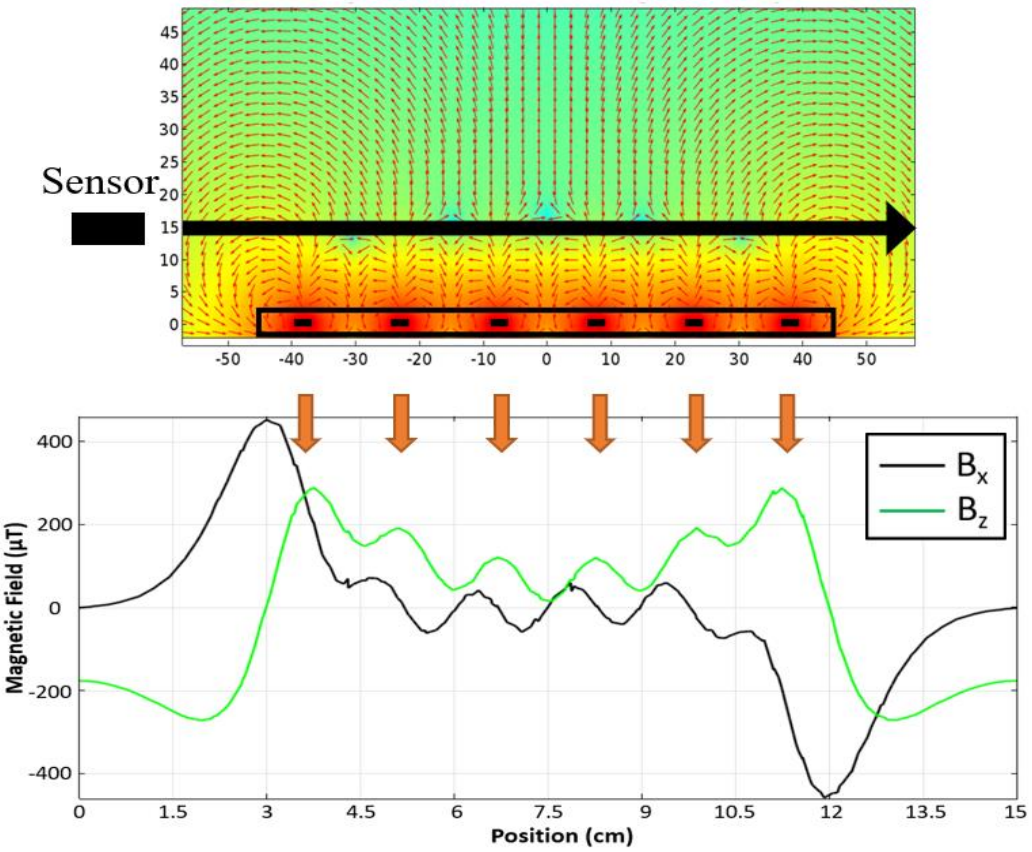

Figure 57. Illustration explaining the scanning mode simulation for planar strain sensing in COMSOL Multiphysics. Top: the magnetic sensor traverses 15 mm above a 4 mm design sensor band stretched to 20 %strain and the magnetic flux density $\left|\vec{\boldsymbol{B}}(x)\right|$ a at each horizontal position x is computed. Colormap indicates the base 10 logarithm of the magnetic flux density magnitude ($\log 10\left|\vec{\boldsymbol{B}}\right|$) and the red arrows corresponds to the direction of magnetic flux density at the position. Bottom: a representative result of the finite element analysis plotting computed $\left|\vec{\boldsymbol{B}}\right|$ in horizontal (x) and vertical (z) axis. The magnetic strips of the band in the top graph is aligned with the peaks of the computed vertical magnetic field $\left|\vec{\boldsymbol{B}}_z\right|$ (green).

The efficacy of alternating magnetic polarizations for magnetic strips is validated by comparisons between Figure 58 and Figure 59, as well as between Figure 61 and Figure 62.

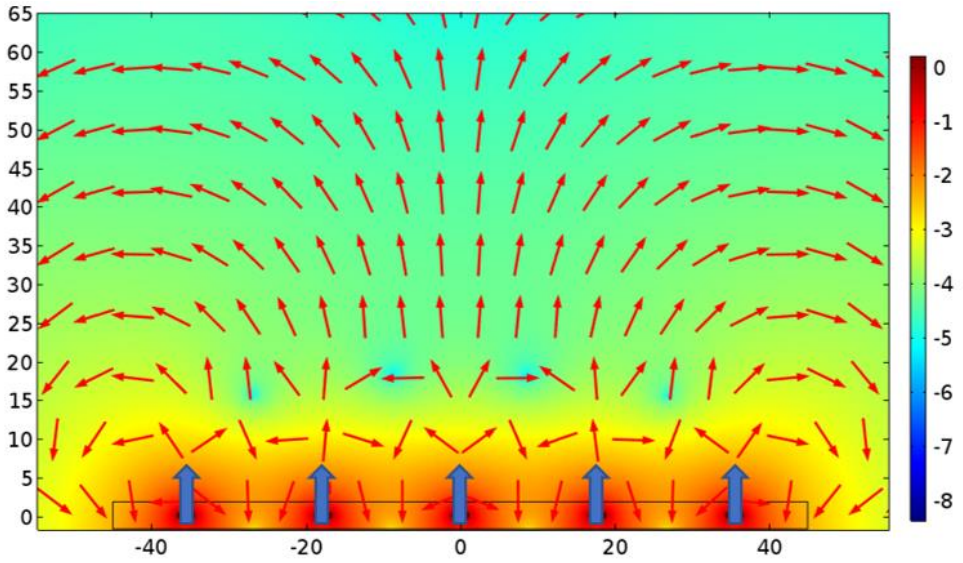

Figure 58. Magneto-static finite element analysis of sensor bands with uniformly polarized magnetic strips. Colormap indicates the base 10 logarithm of the magnetic flux density magnitude ($\log_{10}|\vec{\boldsymbol{B}}|$) and the red arrows corresponds to the direction of magnetic flux density at the position. Blue arrows indicate the direction of strip magnetization.

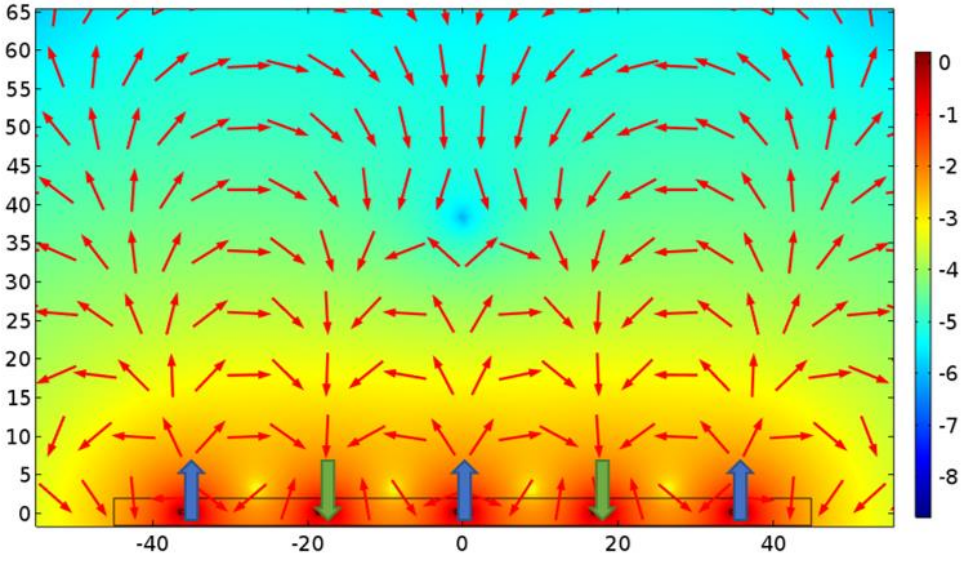

Figure 59. Magneto-static finite element analysis of sensor bands with alternately polarized magnetic strips. Colormap indicates the base 10 logarithm of the magnetic flux density magnitude ($\log_{10}|\vec{\boldsymbol{B}}|$) and the red arrows corresponds to the direction of magnetic flux density at the position. Blue and green arrows indicate the direction of strip magnetization.

Figure 58 and Figure 59 visualizes the direction and magnitude of magnetic flux density induced by sensor bands with uniformly and alternately polarized magnetic strips. Colormap indicates the base 10 logarithm of the magnetic flux density magnitude ($\log_{10}|\vec{\boldsymbol{B}}|$) and the red arrows corresponds to the direction of magnetic flux density at the position. In space above z = 25 mm, the colormap for sensor bands with alternately polarized magnetic strips in Figure 59 exhibits more visible color variation than the almost-uniform green space in Figure 58, implying greater magnetic field gradient. What's more, the direction of magnetic flux density for sensor bands with alternately polarized magnetic strips points either up or down above magnetic strips based on their direction of polarization. In Figure 59 it is clear that the induced loop-like pattern of red arrows extends to even 65 mm vertically above the magnetic strips. Such directional change of magnetic field provides more distinguishable signal for the scanning magnetometer, yielding peaks and troughs in magnetic flux density at a distance beyond what sensor bands with uniform polarization are capable of.

Figure 60 shows the experiment results for scanning mode measurements of planar strain sensing. Magnetic flux density picked up along a horizontal scan line at 25 mm above the sensor band under 20, 40, 60 and 80 %strain, as well as the final averaged strain measurements ε_{avg}, is displayed. Thanks to the multi-strip design and the measurement averaging method for error reduction, all strain measurements have an error of less than 5 %strain while the overall error at all strains achieves 1.98 %strain. The significant higher error at 80 %strain may come from the increasing nonuniform elongation of Ecoflex® interconnection between strips. It is noteworthy that the 'peaks and toughs' pattern becomes more distinguishable as the band stretches. This is attributed to the increase of inter-strip separation that provides greater space for the magnetic field gradient to accrue. Since more distinct measurement patterns enable wireless strain sensing at a greater distance for our system, we hereby propose another sensor band design strategy to increase inter-strip separation for far field sensing applications. However, there is still a tradeoff between the inter-strip separation and far field sensing ability because a sparser strip arrangement will lead to longer band length or inaccurate single measurements.

Figure 61 and Figure 62 plot the magnetic flux density along a horizontal scanning line 40 mm above the sensor band for sensor bands with uniformly and alternately polarized magnetic strips respectively. For sensor bands with uniformly polarized magnetic strips, Figure 61, neither the horizontal component $\vec{\boldsymbol{B}}_x$ nor the vertical component $\vec{\boldsymbol{B}}_z$ of the flux density exhibit the peaks

or troughs which are critical to the localization of magnetic strips and subsequent determination of overall band strain. The vertical component of magnetic flux density $\vec{B}_z$ does increase when scanning above the sensor band but forms a flat-topped 'mesa' where the desired peaks vanish. In Figure 61, where the same sensor band with uniform polarization is scanned at a smaller distance of 15 mm, the resultant curve of $\vec{B}_z$ is clearly a superposition of a taller 'mesa' pattern topped at 200 μT and the desired peaks. Compared with the shorter 'mesa' pattern with an elevation of 50 μT and the absence of desired peaks for sensor scanning at 40 mm, the induced magnetic field attenuates rapidly within the additional distance, diminishing the spatial magnetic pattern required for strain measurement. Hence, we conclude that sensor bands with uniform polarization is unfeasible for scanning mode at long distance.

For sensor bands with alternately polarized magnetic strips, both horizontal and vertical components of the scanned magnetic field at 40 mm shows the distinguishable 'peak and trough' patterns. Particularly, the vertical component $\vec{B}_z$ aligns well with the position of the magnetic strips, making it easy to quantify the inter-strip separation. The peaks of $\vec{B}_z$ in Figure 62 have approximately the same magnitude as $\vec{B}_z$ in Figure 61, implying that the alternation of strip polarization promotes long distance strain sensing in scanning mode by amplifying gradient rather than the intensity of the inter-strip magnetic field.

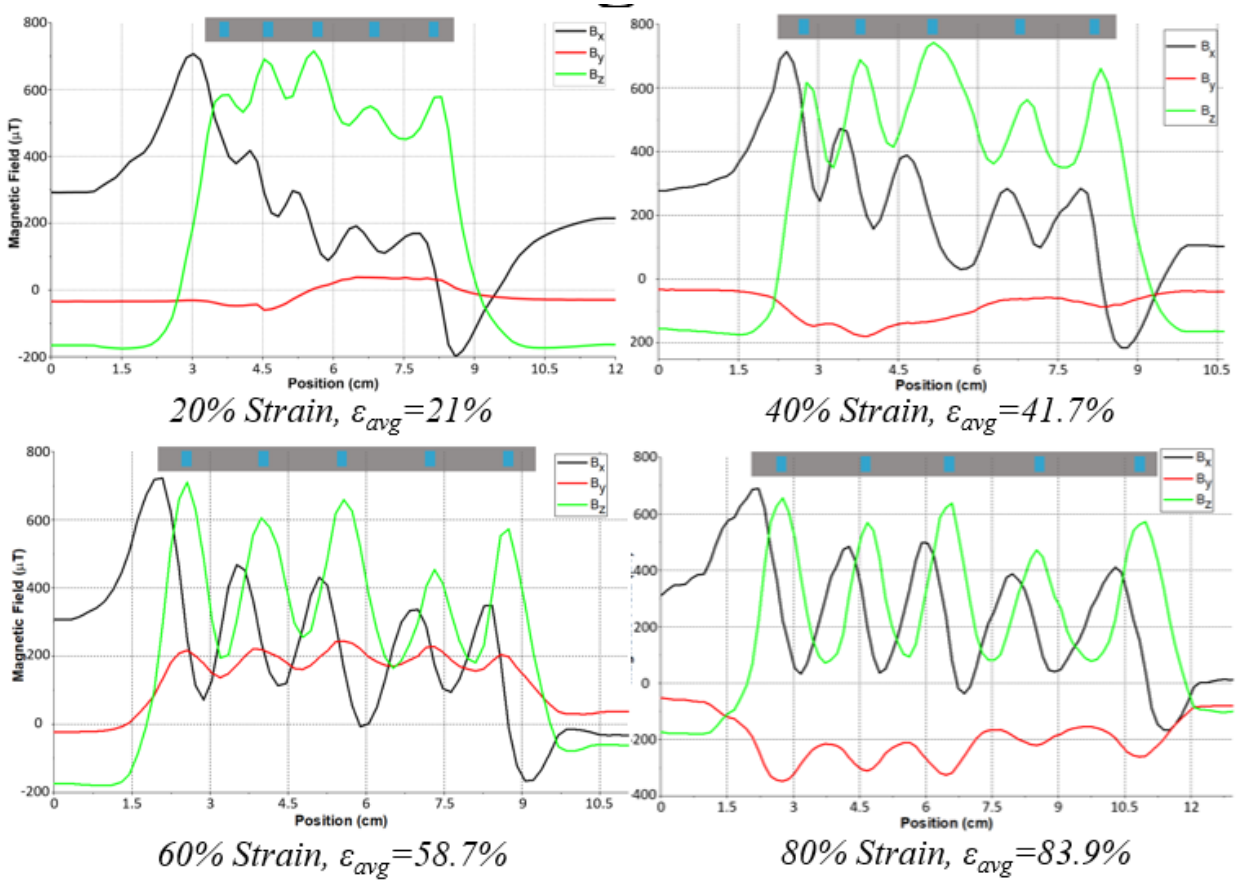

Figure 60. Experiment results for scanning mode measurements of planar strain sensing. Magnetic flux density picked up along a horizontal scan line at 40 mm above the sensor band under 20, 40, 60 and 80 %strain, as well as the final averaged strain measurements ε_{avg}, is displayed. The measurement error is 1 %strain at 20 %strain, 1.7 %strain at 40 %strain, 1.3 %strain at 60 %strain, and 3.9 %strain at 80 %strain.

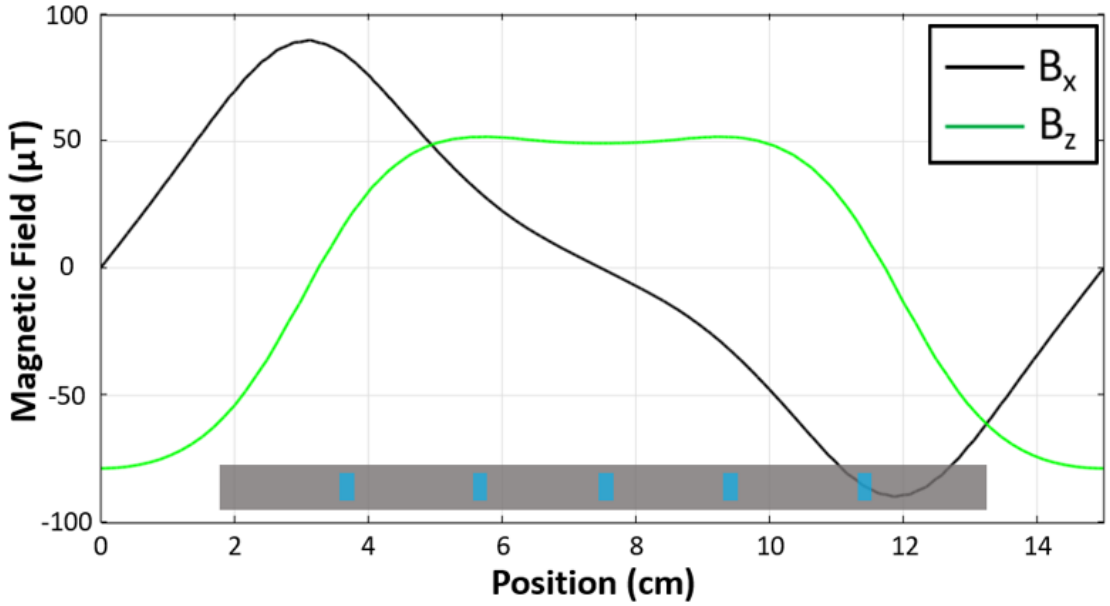

Figure 61. Magnetic flux density along a horizontal scanning line 40 mm above a sensor band with uniformly polarized magnetic strips. Neither $\vec{B}_x$ (black) nor $\vec{B}_z$ (green) exhibit the peaks or troughs which are critical to the localization of magnetic strips and subsequent determination of overall band strain. The vertical component of magnetic flux density $\vec{B}_z$ does increase when scanning above the sensor band but forms a flat-topped 'mesa' where the desired peaks vanish.

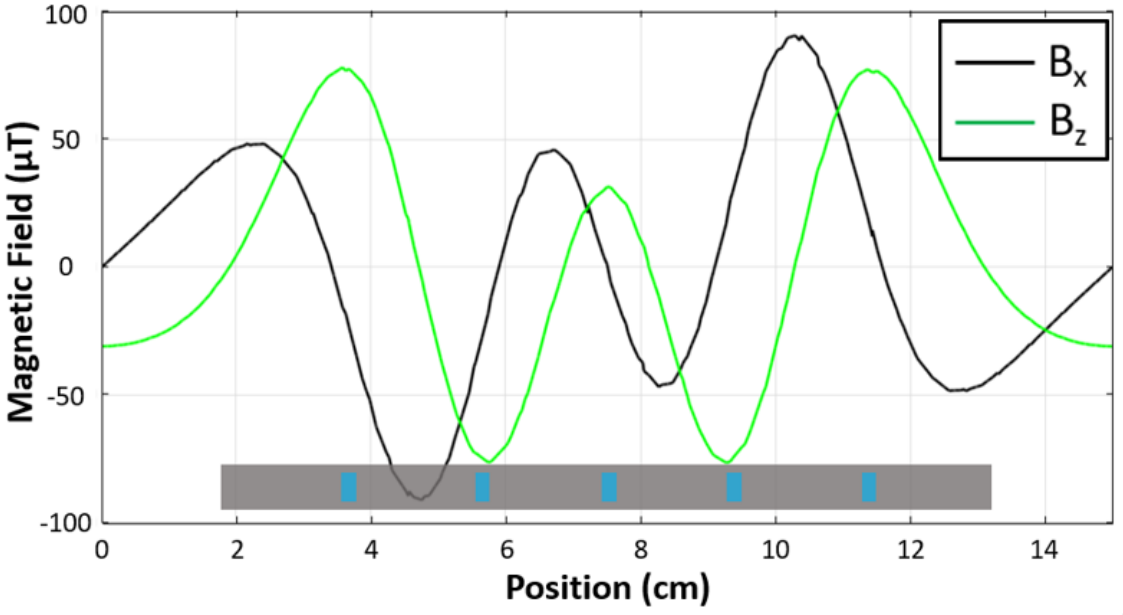

Figure 62. Magnetic flux density along a horizontal scanning line 40 mm above a sensor band with alternately polarized magnetic strips. Both horizontal and vertical components of the scanned magnetic field at 40 mm shows the distinguishable 'peak and trough' patterns. Particularly, the vertical component $\vec{B}_z$ aligns well with the position of the magnetic strips, making it easy to quantify the inter-strip separation.

Scanning mode for curved strain sensing Curved strain sensing experiments were conducted with the magnetometer scanning at a distance equivalent to abdomen thickness. Table 13 manifests some physiological measurements excerpted from Akkus et al. [112] including subcutaneous adipose tissue thickness of adults at anterior abdomen measured by ultrasonography.

Table 13. Anatomic measurements excerpted from Akkus et al. [112], including subcutaneous adipose tissue thickness of anterior abdomen measured at 5 cm below navel, waist circumference and body mass index. The subcutaneous adipose tissue thickness is measured by ultrasonography.

Item	**Males (n=141)**	**Females (n=308)**
Subcutaneous adipose tissue thickness (mm) at anterior abdomen (5 cm below navel)	11.05 ± 8.44	17.87 ± 9.68
Waist circumference (cm)	95.87 ± 10.65	90.91 ± 16.27
Body mass index (kg/cm^2)	27.56 ± 3.97	29.41 ± 7.18

Subcutaneous adipose tissue thickness of 11.05 ± 8.44 mm is reported for male subjects and 17.87 ± 9.68 mm for female subjects. These measurements have good generalization among adults as over 400 subjects with ages ranging from 18 to 80 were gauged. Sensor bands with 8 cm inter-strip separations were used per the design guideline that sparser strip arrangement promotes far field strain sensing. Based on the experiment results above, strains of an 8 cm design can be measured from 40 mm away and a proposed site of sensor band implantation is shown in Figure 63. Sensor band is to be sutured on the bladder near pubis where the subcutaneous tissue is thin. Upon scanning, the patients move a cellphone around their abdomen once and the system would yield the strain measurements or the interpreted bladder volume.

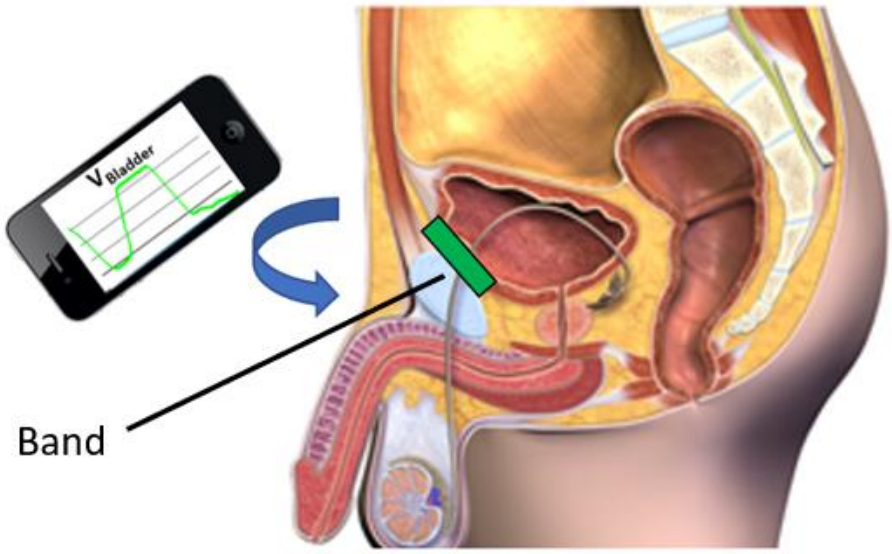

Figure 63. A proposed location of sensor band implantation. Sensor band is to be sutured on the bladder near pubis where the subcutaneous tissue is thin. Upon scanning, the patients move a cellphone around their abdomen once and the system would yield the strain measurements or the interpreted bladder volume.

Finite element analysis of the scanning mode for curved strain sensing under the proposed operation scenario is presented in Figure 64. A sensor band with 8 mm inter-strip separation was stretched along a circular surface to an equivalent bladder volume of 100 ml, 300 ml, and 500 ml. Observing the magnetic flux density colormaps in Figure 64a to Figure 64c, we found the magnetic flux density onsite of scanning trace increases as the band gets stretched. The magnetic sensor scanned along an identical path that is at least 35 mm away for all volumes. The magnitude of vertical magnetic flux density $\vec{\boldsymbol{B}}_z$ along the scanning curve for all bladder volumes are plotted in Figure 64d. Aligning with the observations on the magnetic flux density color maps in Figure 64a to Figure 64c, the measured vertical magnetic flux density is the highest and the 'peak and trough' pattern is the most distinctive in the simulation with a bladder volume of 500 ml. It is noteworthy that the peaks correspond to the first and the last magnetic strip disappeared as they became out of sensing range when placed along a circular surface. The same peak detection algorithm and strip localization technique used in planar strain sensing were adopted for the curved sensing mode to estimate an averaged overall strain measurement.

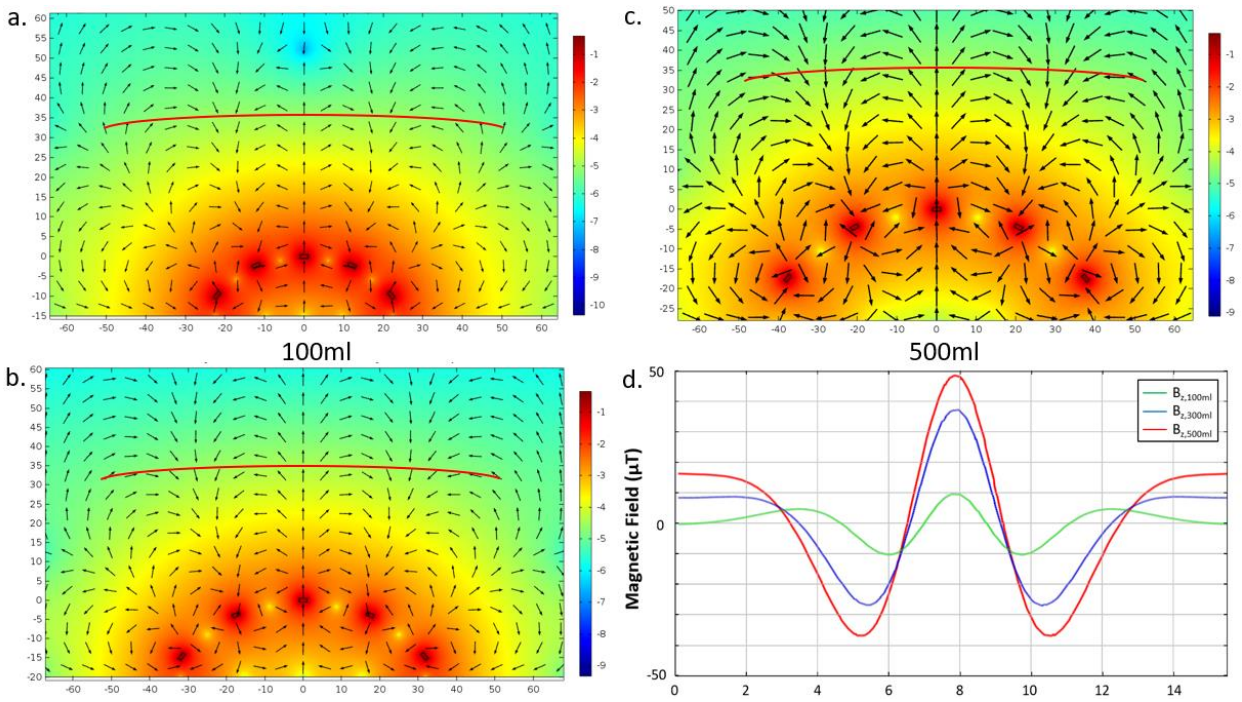

Figure 64. Finite element analysis of the scanning mode for curved strain sensing under the proposed operation scenario. A sensor band with 8 mm inter-strip separation was stretched along a circular surface to an equivalent bladder volume of (a)100 ml, (b) 300 ml, and (c) 500 ml. (d) Plot of the magnitude of vertical magnetic flux density $\vec{B}_z$ along the scanning curve for all bladder volumes.

The scanning mode experiment for curved strain sensing was conducted with the setup shown in Figure 44. The latex balloon was filled with 100 ml, 300 ml, and 500 ml water to mimic different amount of urinary retention. Figure 65 plots the vertical magnetic flux density $\vec{B}_z$ along the scanning trace in all three experiments. The sensor band at a strain equivalent to 500 ml bladder volume exhibits the greatest 'peak and trough' pattern as expected. In accordance with the simulation results, the peaks correspond to the first and the last magnetic strip disappeared as they went out of sensing range when placed along a circular surface. The error of the averaged strain measurement became 5.3 %strain, 6.7 %strain and 7.1 %strain at 100 ml, 300 ml and 500 ml. Compared with the average measurement error of 2.3 %strain, the rise of measurement errors in scanning mode for curved strain sensing can be mostly attributed from two factors. First, the absence of measurements from the first and last strip reduced the number of measurement averaging can be performed for error reduction. Second, the magnetic strips are no longer in-plane with each other, distorting the magnetic field so that a mismatch between the position of the peaks in magnetic flux density curve and the actual position of the strip.

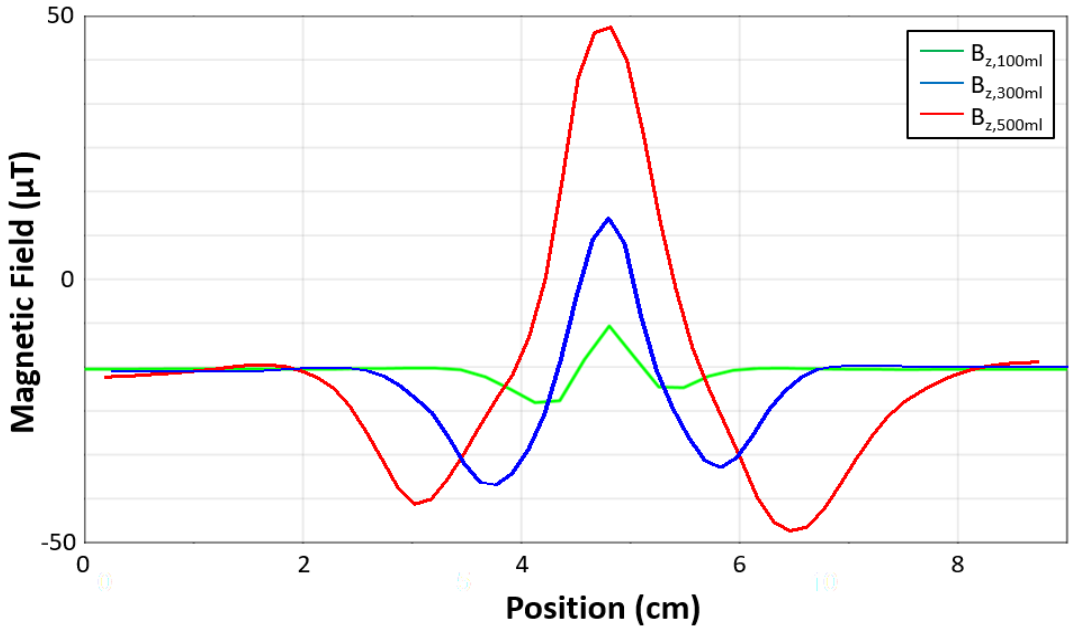

Figure 65. The vertical magnetic flux density $\vec{B}_z$ along the scanning trace in all three experiments. The sensor band at a strain equivalent to 500 ml bladder volume exhibits the greatest 'peak and trough' pattern as expected. In accordance with the simulation results, the peaks correspond to the first and the last magnetic strip disappeared as they went out of sensing range when placed along a circular surface. The error of the averaged strain measurement became 5.3 %strain, 6.7 %strain and 7.1 %strain at 100 ml, 300 ml and 500 ml.

3.5.6 Durability test

Results for transient signal of magnetic flux density picked up by a smartphone in 1600 cycles of sensor band stretched to 80 %strain, as well as the mechanical load of the sensor band in 1100 cycles of sensor band stretched to 80 %strain, are shown in Figure 66. The initial and end cycles of each recording is exhibited in detail. The amount of drift observed is less than 3% for magnetic flux density readings, Figure 66 left. This indicates that no substantial change in mechanical structure, magnetic property, or sensor drifting are present, proving the overall robustness of the proposed wireless strain sensing system. The minimal drift (< 2%) in the mechanical tension of the sensor bands further proves that no noticeable structural deterioration such as tear, delamination, or irreversible elongation appeared, Figure 66 right.

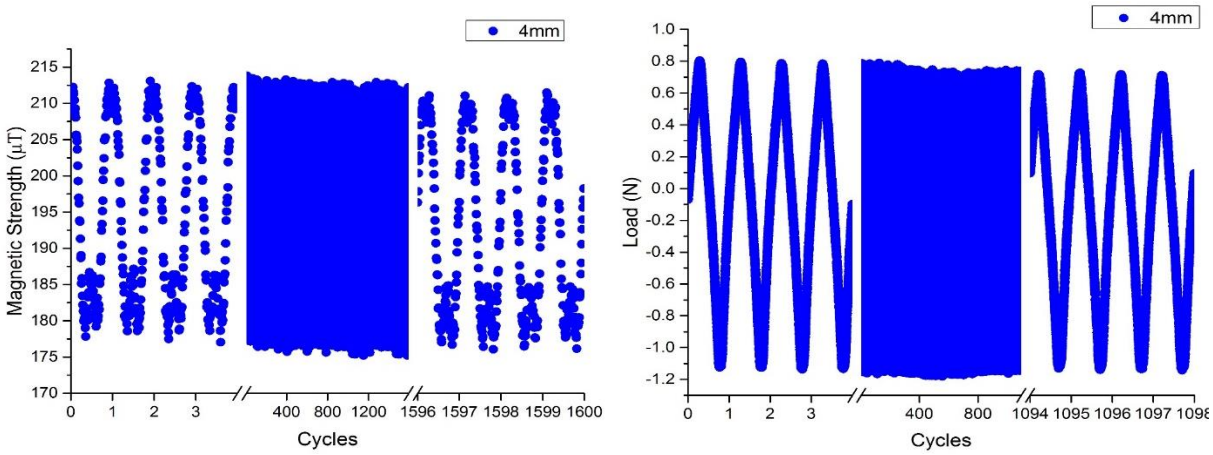

Figure 66. Durability test results. Left: transient signal of magnetic flux density picked up by a smartphone in 1600 cycles of sensor band stretching to 80 %strain, right: the mechanical load of the sensor band in 1100 cycles. The initial and end cycles of each recording is exhibited in detail. The amount of drift observed is less than 3% for the measured transient magnetic flux density, and less than 2% for the mechanical tension of the sensor band.

3.5.7 Actuation mode experiments

The magnetic attraction force exerted by magnetic strips made from strontium ferrite ($SrFe_{12}O_{19}$) or neodymium-iron-boron (NdFeB) powder and a neodymium-iron-boron actuation magnet over distance is plotted in Figure 67. Sensor bands each with five embedded magnetic strips but different inter-strip separation were tested. It follows an inverse squared relation with distance within the measurement range of 27 to 47 mm. Strips made from neodymium-iron-boron powder exhibit a stronger actuation force of 0.7 N at 27 mm and 0.13 N at 47 mm. Strips made from strontium ferrite powder exhibit about have the actuation force of 0.37 N at 27 mm and 0.06 N at 47 mm. No remarkable discrepancy is observed from the magnetic actuation force exerted by bands with different inter-strip separations. Malone-Lee et al. [118] established a function to describe the detrusor pressure P_{det} applied on the urine, exerted by bladder detrusor muscle:

$$P_{det} = \frac{F}{\pi r^2} = F\left(\frac{3V}{4\pi}\right)^{-2/3}/\pi \qquad (19)$$

where F is the force exerted by the detrusor muscle and V is the volume of the bladder. Following this equation and the detrusor pressure at maximum voiding rate depicted in [119], such actuation can add up to 19.6% of bladder pressure which should be effective to urination.

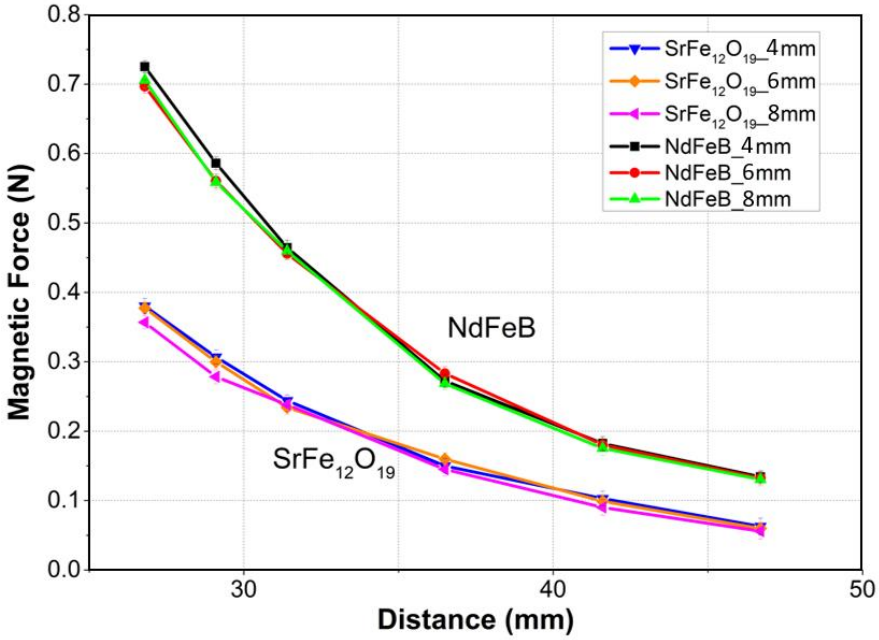

Figure 67. The magnetic attraction force exerted by magnetic strips made from strontium ferrite ($SrFe_{12}O_{19}$) or neodymium-iron-boron (NdFeB) powder and a neodymium-iron-boron actuation magnet over distance. It follows an inverse square law with distance within the measurement range of 27 to 47 mm.

Figure 68 plots the time-lapsed volume change of residual liquid volume inside the bladder phantoms free from actuation (red) and under actuation (blue). Vertical error bars are one standard-deviation of residual liquid volume at the given timestamp. Horizontal error bars on the last datapoints corresponds to one standard-deviation of ending timestamp when liquid stops flowing out. Starting with 75 ml of liquid inside, bladder phantoms under actuation dispense 74.1 ml in 69 seconds whereas phantoms void of magnetic actuation eject 69.4 ml in 85 seconds. With the additional detrusor pressure exerted from the attracted magnetic strips, bladder phantoms under actuation dispense liquid 18.8% faster and leave 83.9% less residual liquid than those without actuation. Despite that the actuation experiment with bladder phantom yields very preliminary result, it is a positive first step for future in-vitro and in-vivo experiments that further validate the effectiveness of magnetic bladder actuation.

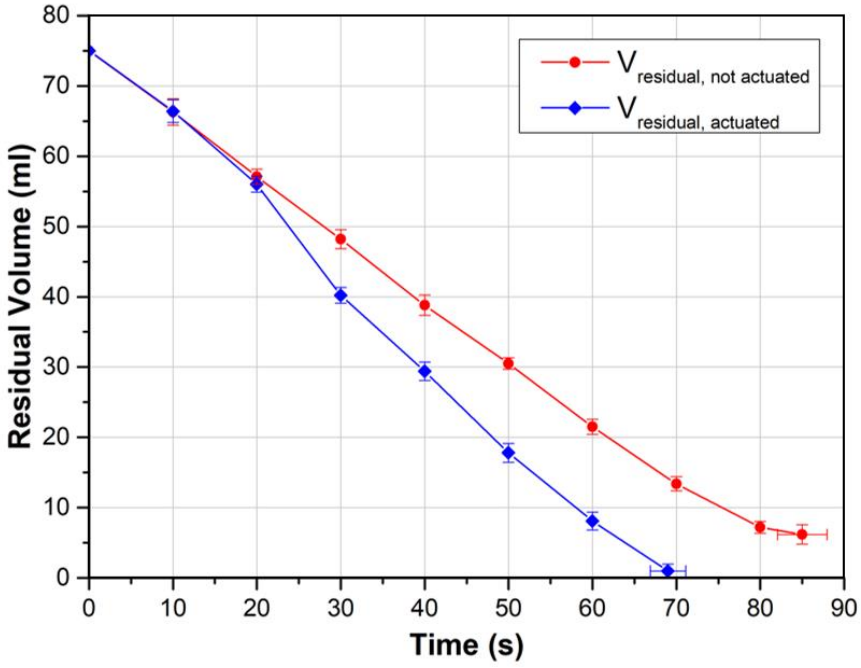

Figure 68. Time-lapsed volume change of residual liquid volume inside the bladder phantom free from actuation (red) and under actuation (blue). Vertical error bars are one standard-deviation of residual liquid volume at the given timestamp. Horizontal error bars on the last datapoints corresponds to one standard-deviation of ending timestamp when liquid stops flowing out.

3.6 Conclusion

We developed an implantable, passive magnetic strain sensing system with polymeric magnets laser- micromachined, re-magnetized and embedded into a carefully designed PDMS/Ecoflex® silicone composite band. The stiffer PDMS encapsulates the polymeric magnets while the softer Ecoflex® fills the gap between PDMS regions. This unique composite structure utilizes stiffness gradient, preventing magnet delamination from elastomer matrix while maintaining overall stretchability. Magneto-static finite element analysis and strain experiments were performed to justify the magnetic and mechanical aspect of the sensor design. The strain sensing system was then calibrated within physiological relevant strain ranges. Cardiac cycle relevant strains (60–100 bpm, 40–60 %strain) can be measured wirelessly by a smartphone from 25 mm away, a distance comparable to average human chest wall thickness, with a sensitivity of 1.13 μT/10 %strain. Scanning mode for strain sensing on planar and curved surfaces were simulated and validated. An average strain error of 2.3 %strain is recorded for planar strain sensing and 5.2 %strain for curved strain sensing. Utilization of alternating magnetic strip polarization

successfully extends the sensing range to 40 mm. In-vitro magnetic actuation experiments under urinary-tract related conditions show that the magnetic force from sensor bands add up to 19.6% detrusor pressure and alleviate urinary retention by facilitating micturition by 18.8% and by reducing bladder residual liquid by 83.9%.

4. CONCLUSIONS AND FUTURE DIRECTIONS

In this thesis, I have documented my efforts towards exploring and proving the feasibility of wireless magnetic sensing of tissue deformations featuring polymeric magnets. Results for a wireless brain deformation sensing system for blast induced traumatic injury (bTBI) featuring a polymeric magnetic disk and results for a wireless, smartphone-aided strain sensing system for heart failure (HF) or bladder dysfunction featuring a stretchable polymeric magnetic band are presented. Through end-to-end research and development on the two projects including background investigation, theory derivation, system design, sensor selection, algorithm development, system calibration, and experiment execution, we are now confident that tissue deformations can be measured wirelessly by tracking the motion of a piece of polymeric magnet attached to the tissue. With subtle sensing system design and rigorous validation, wireless magnetic tissue deformation sensing systems can provide a low-cost, wearable option for chronic complication monitoring with no line-of-sight required. Remarkably, some joint findings in mild-bTBI biomechanics with our collaborators in Professor Shi's lab have elucidated the lingering myth of whether a mild blast wave can penetrate through the skull and assert direct biomechanical impact on brain tissue and enabled breakthroughs in bTBI research [120], [121]. Meanwhile, the inclusion of a smartphone as part of the wireless strain sensing system demonstrates that, by subtle sensing system design, tissue deformation can be monitored magnetically and wirelessly using consumer electronics that are shipped in millions annually rather than dedicated sensors. This could greatly facilitate the commercialization of such product and make it easier to gain popularity among patients.

To surpass the level of potential and feasibility of wireless magnetic tissue deformation sensing systems that has been demonstrated thus far, additional validations and experiments are necessary. In the next few sections I will share my humble thoughts on future directions on pushing the unknown boundary a little further and on driving the projects towards possible commercialization.

4.1 The Wireless Intracranial Deformation Sensing System

4.1.1 Surface deformation vs. deep tissue deformation: relation and significance

As discussed in Chapter 2, the intracranial deformation sensing system can record real-time deformation during a blast event. However, this is a localized deformation measured at the site of the polymeric magnet and can only describe how the brain surface deformed. Given that the brain tissue has a heterogenous structure comprising of white matter and grey matter, each having different mechanical properties, the deformation inside the brain is likely to be distinct from that of the surface. A thorough understanding of deep tissue deformation during the blast, especially a mild blast, is critical to elucidating how blast wave damages white matters and gray matters, as well as to quantify the damage threshold for various brain regions. With a relation between the sub-surface deformation and surface deformation established, we will be able to extrapolate deep tissue deformation based on the recorded deformation data from brain surface.

In an effort towards the abovementioned endeavor, we have designed a novel coronal brain phantom and begun relevant experiments. In the designed phantom, transparent 'skull' made from acrylic contained a slice of silicone brain phantom or real animal brain tissue. Similar to the experiment described in Chapter 2, a piece of polymer magnet was placed on top of the brain phantom or tissue and an external GMR sensor array was deployed to measure magnet movement. Cross-section of the skull phantom was covered by acrylic plates and silicone oil was injected to the gap between the brain phantom and the skull phantom before sealing in order to mimic the cerebral spinal fluid (CSF). Figure 69 shows a picture of the proposed coronal brain phantom under high-speed camera with different components labeled in red. The same high-speed camera was used to record the anisotropic deformation across the brain phantom or tissue. Speckle dot patterns were painted or dyed on the brain phantom or tissue for subsequent image analysis. The experiment goal was to explore the relationship between the brain surface deformation measured by our novel wireless intracranial deformation sensing system and the deep tissue deformation captured in the high-speed image sequence of proposed coronal brain phantom.

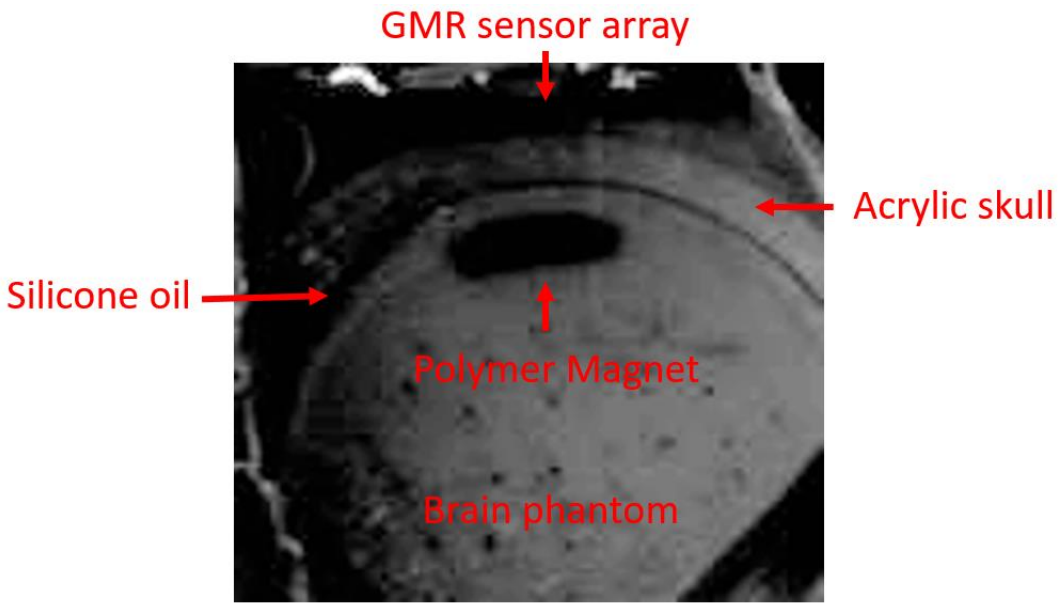

Figure 69. Picture of the proposed coronal brain phantom under high-speed camera with different components labeled in red. Speckle dot patterns were painted or dyed on the brain phantom or tissue for subsequent image analysis.

Figure 70 shows an exemplary set of images captured by the high-speed camera during a mild blast. The images were recorded at a 66666 frames/second and have their corresponding timestamps relative to the first frame labeled below. Digital image correlation (DIC) analysis was utilized to compute the inter-frame displacement inside a set of images. The DIC algorithm first divides every image into many rectangular mini patches each containing several pixels and, assuming the mini patches are small enough so that they don't change shape overtime, takes positions in consecutive frames with the highest Pearson's correlation as the patches' occurrence. Finally, inter-frame mini patch translation (displacement) is computed from the patch's position in the current frame and the next frame. The colored square overlay on each silicone brain phantom region is a colormap visualizing the amount of vertical deformation. Starting with no deformation at 0 ms, the silicone brain phantom underwent nonuniform deformation at 0.36 ms. The deformation of the phantom reached its maximum vertical deformation at 0.47 ms as resembled by a majority of mini patches in yellow or orange. Gradually, the silicone brain phantom relaxes and its deformation drops to zero.

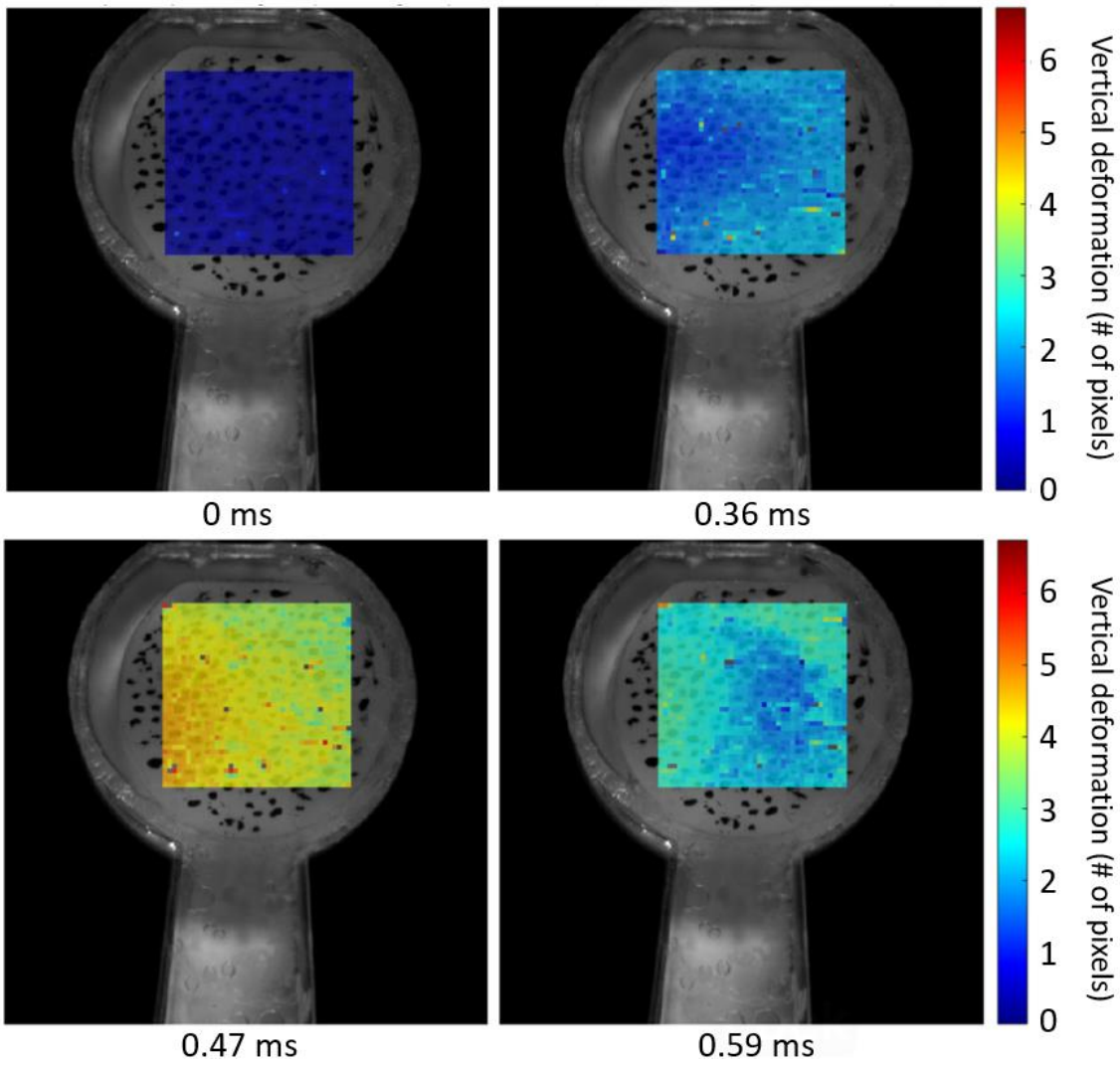

Figure 70. an exemplary set of images captured by the high-speed camera during a mild blast. The images were recorded at a 66666 frames/second and have their corresponding timestamps relative to the first frame labeled below. The colored square overlay on each brain phantom is a colormap visualizing the amount of vertical deformation. Starting with no deformation at 0 ms, the silicone brain phantom underwent nonuniform deformation at 0.36 ms. The deformation of the phantom reached its maximum vertical deformation at 0.47 ms as resembled by a majority of mini patches in yellow or orange. Gradually, the silicone brain phantom relaxes and its deformation drops to zero.

Preliminary results from a homogenous silicone brain phantom have confirmed that the nonuniformity of deformation, marked by the uneven color distributions in deformation colormaps, persists across all frames during the blast event. It is almost utterly certain that greater nonuniformity exists in real brain with heterogenous tissues such as white matter and gray matter. Such region-specific deformations, if can be related to the surface deformation measurements from

our wireless intracranial deformation system, will provide vast additional information for injury analysis and blast damage threshold determination.

Stepping beyond the current experiments, I believe it is imperative to:

- Replace homogenous silicone brain phantom with slices of real brain tissue.
- Establish quantitative relationship between the surface deformation and the deep tissue deformation through mathematical modeling, statistical analysis, or machine learning methods.
- Incorporate biochemical analysis with region-specific blast deformation to determine the blast damage threshold for each brain area.

4.2 The Wireless Magnetic Strain Sensing System

4.2.1 Integrate smartphone motion data in scanning mode strain sensing

Currently the scanning mode of wireless strain sensing requires the smartphone to traverse along a fixed trace at a fixed speed so that the transient magnetic sensor data ($\vec{\boldsymbol{B}}_x$, $\vec{\boldsymbol{B}}_y$, $\vec{\boldsymbol{B}}_z$, t) can be associated to spatially into ($\vec{\boldsymbol{B}}_x$, $\vec{\boldsymbol{B}}_y$, $\vec{\boldsymbol{B}}_z$, x). Even though fixed scanning trace ensured a controlled and consistent sensing mode, it is not practical in the intended application where the patient is expected to perform the scanning by hand. Under optimal conditions, our sensing system should be able to localize itself in space and record any arbitrary trace it moved along.

Such trace tracking feature is viable for a smartphone thanks to the inertial measurement unit (IMU) integrated to the phone. IMU usually comprises of an accelerator and a gyroscope which measures the unit's linear acceleration and angular velocity, respectively. Sometimes a magnetometer or a Global Positioning System (GPS) unit is also included. It has long been used for localization and tracking of aircrafts, satellites, automobile vehicles and consumer electronics. In short, the translational (linear) motion of the IMU is calculated by integrating accelerometer reading twice over time whereas the rotational (angular) motion of the IMU is computed by integrating gyroscope reading over time. The final motion trace is a joint estimation from translational and rotational motion results. If IMU data are recorded when the smartphone scans over sensor band, we will be able to estimate a scanning trace and associate temporal magnetic field data to the spatial domain. With the help of IMU reading and appropriate trace localization algorithms, our system can perform scanning mode strain sensing along arbitrary scanning lines.

Promising the method described above seems, it takes great engineering effort for a robust implementation to take place. Localization and tracking by accelerometers and gyroscopes only are prone to sensor drifting issues as part of the nature of using temporal integrations. Development of proper algorithms for calibrating IMU reading against other sensor references, and for fusing all sensor data into one final reliable trace estimation, will be crucial to a successful implementation.

4.2.2 In-vivo strain sensing experiment

Extensive experiments have characterized the proposed wireless, smartphone-aided magnetic strain sensing system in terms of its mechanical & magnetic traits, design tradeoffs and different strain sensing modes. While in-vitro experiments have proved the system's potential on targeted applications such as chronic heart failure monitoring and urinary retention management, no in-vivo experiment has been conducted to further confirm such feasibility. As part of a progressive investigation, it is suggestive to first conduct ex-vivo experiments using hearts and bladders taken from dead animals and then move on to full-fledged live animal experiments.

4.2.3 Further characterization of actuation mode

In-vitro characterization and experiments conducted in urinary tract related conditions have shown promising results for active urinary retention management. However, results are still preliminary without in-vivo experiments. One of the biggest downsides of magnetic actuation is that the actuation strength diminishes rapidly over distance so that wireless magnetic actuation could be too feeble especially when the bladder volume is high (severe urinary retention). To begin with, additional characterization and experiments should approximate the in-vivo environments by using bladders from dead animals. Should any actuation issue emerged, future research needs to focus on establishing new sensor band design strategies and guidelines for optimizing wireless magnetic actuation. Lastly, it is still uncertain if design strategies for wireless magnetic sensing and actuation will compliment or contradict each other. If complimentary, a jointly optimized design strategy should be summarized to achieve superior sensing and actuation performance. If contradictory, the tradeoff between sensing and actuation design strategy must be carefully examined to fulfill desired requirements.

REFERENCES

[1] G. Michel, T. Tonon, D. Scornet, J. M. Cock, and B. Kloareg, "The Cell Wall Polysaccharide Metabolism of the Brown Alga Ectocarpus Siliculosus. Insights into the Evolution of Extracellular Matrix Polysaccharides in Eukaryotes," *New Phytol.*, vol. 188, pp. 82–97, 2010.

[2] N. Singh and U. C. Sharma, "Introduction to Nano-Biomaterials," in *Nanotechnology Biomaterials*, no. 11, 2014, pp. 1–12.

[3] H. Yamada, *Strength of biological materials*. 1970.

[4] W. Huda and R. B. Abrahams, "X-Ray-based Medical Imaging and Resolution," *Am. J. Roentgenol.*, vol. 204, pp. 393–397, 2015, doi: 10.2214/AJR.14.13126.

[5] G. Li, S. K. Van De Velde, and J. T. Bingham, "Validation of a Non-invasive Fluoroscopic Imaging Technique for the Measurement of Dynamic Knee Joint Motion," *J. Biomech.*, vol. 41, pp. 1616–1622, 2008, doi: 10.1016/j.jbiomech.2008.01.034.

[6] S. F. Nemec, S. Marlovits, S. Trattnig, W. Matzek, M. E. Mayerhoefer, and C. R. Krestan, "High-resolution Magnetic Resonance Imaging and Conventional Magnetic Resonance Imaging on a Standard Field-strength Magnetic Resonance System Compared to Arthroscopy in Patients with Suspected Meniscal Tears," *Acad. Radiol.*, vol. 15, no. 7, pp. 928–933, 2008, doi: 10.1016/j.acra.2008.02.007.

[7] D. Stucht, K. A. Danishad, P. Schulze, and F. Godenschweger, "Highest Resolution In Vivo Human Brain MRI Using Prospective Motion Correction," *PLoS One*, vol. 10, no. 7, pp. 1–17, 2015, doi: 10.1371/journal.pone.0133921.

[8] P. N. T. Wells and H. Liang, "Medical Ultrasound: imaging of Soft Tissue Strain and Elasticity," *Sensors*, vol. 8, no. 64, pp. 1521–1549, 2011, doi: 10.1098/rsif.2011.0054.

[9] S. Dixon, "Diagnostic Imaging Dataset Statistical Release," 2019.

[10] E. L. Tan, B. D. Pereles, B. Horton, R. Shao, M. Zourob, and K. G. Ong, "Implantable Biosensors for Real-time Strain and Pressure Monitoring," *Sensors*, vol. 8, no. 10, pp. 6396–6406, 2008, doi: 10.3390/s8106396.

[11] S. Song, N. S. Race, A. Kim, T. Zhang, R. Shi, and B. Ziaie, "A Wireless Intracranial Brain Deformation Sensing System for Blast-Induced Traumatic Brain Injury," *Sci. Rep.*, vol. 5, no. November, pp. 1–10, 2015, doi: 10.1038/srep16959.

[12] "NDI Aurora Electromagnetic Tracking System." [Online]. Available: http://www.ndigital.com/aurora.php.

[13] "Ascension Technology Corporation Products Application." [Online]. Available: http://www.ascension-tech.com/products/microbird.php.

[14] D. Frantz, S. Kirsch, S. Leis, and A. Wiles, "Accuracy Assessment Protocols for Electromagnetic Tracking Systems," *Phys. Med. Biol.*, vol. 48, pp. 2241–2251, 2003, doi: 10.1016/S0531-5131(03)00328-5.

[15] W. Andra *et al.*, "A novel method for real-time magnetic marker monitoring in the gastrointestinal tract," *Phys. Med. Biol.*, vol. 45, pp. 3081–3093, 2000.

[16] J. Hummel, M. Figl, C. Kollmann, H. Bergmann, and W. Birkfellner, "Evaluation of a Miniature Electromagnetic Position Tracker," *Med. Phys.*, vol. 29, no. 10, pp. 2205–2212, 2002, doi: 10.1118/1.1508377.

[17] A. Plotkin and E. Paperno, "3-D Magnetic Tracking of a Single Sub-miniature Coil With a Large 2-D Array of Uniaxial Transmitters," *IEEE Trans. Magn.*, vol. 39, no. 5, pp. 3295–3297, 2003.

[18] F. H. Raab, E. B. Blood, T. O. Steiner, and H. R. Jones, "Magnetic Position and Orientation Tracking System," *IEEE Trans. Aerosp. Electromagn. Syst.*, vol. 15, no. 5, pp. 709–718, 1979.

[19] E. Paperno, I. Sasada, and E. Leonovich, "A new method for magnetic position and orientation tracking," *IEEE Trans. Magn.*, vol. 37, no. 4, pp. 1938–1940, 2001.

[20] H. P. Kalmust, "A New Guiding and Tracking System," in *IRE Transactions on Aerospace Navigational Electronics*, 1962, no. 9, pp. 7–10.

[21] W. Weitschies, R. Kotitz, D. Cordini, and L. Trahms, "High-resolution Monitoring of the Gastrointestinal Transit of a Magnetically Marked Capsule," *J. Pharm. Sci.*, vol. 86, no. 1, pp. 1218–1222, 1997.

[22] V. Schlageter, P. Besse, R. S. Popovic, and P. Kucera, "Tracking System with Five Degrees of Freedom using a 2D-array of Hall Sensors and a Permanent Magnet," *Sensors Actuators A Phys.*, vol. 92, no. 1, pp. 37–42, 2001.

[23] K. Enpuku *et al.*, "Biological Immunoassays without Bound/Free Separation utilizing Magnetic Marker and HTS SQUID," *IEEE Trans. Appl. Supercond.*, vol. 17, no. 1, pp. 816–819, 2007.

[24] K. Enpuku, D. Kuroda, T. Q. Yang, and K. Yoshinaga, "High Tc SQUID System and Magnetic Marker for Biological Immunoassays," *IEEE Trans. Appl. Supercond.*, vol. 13, no. 1, pp. 371–376, 2003.

[25] X. Wang, M. Q. Meng, and Y. Chan, "A Low-cost Tracking Method based on Magnetic Marker for Capsule Endoscope," in *Proceedings of International Conference of Information Acquisition*, 2004, pp. 524–526.

[26] W. Hou, X. Zheng, C. Peng, P. Kzv, F. Q. Dkrr, and F. R. P. Fq, "Experimental Study of Magnetic-based Localization Model for Miniature Medical Device Placed Indwelling Human Body," in *Proceedings of 27th International Conference of Engineering in Medicine and Biology Society*, 2005, pp. 1309–1312.

[27] S. Yamada, C. P. Gooneratne, M. Iwahara, and M. Kakikawa, "Detection and Estimation of Low-concentration Magnetic Fluid Inside Body by a Needle-type GMR Sensor," *IEEE Trans. Magn.*, vol. 44, no. 11, pp. 4541–4544, 2008.

[28] C. Carr, A. N. Matlachov, H. Sandin, M. A. Espy, and R. H. Kraus, "Magnetic Sensors for Bioassay : HTS SQUIDs or GMRs ?," *IEEE Trans. Appl. Supercond.*, vol. 17, no. 2, pp. 808–811, 2007.

[29] J. M. Daughton, "GMR and SDT Sensor Applications," *IEEE Trans. Magn.*, vol. 36, no. 5, pp. 2773–2778, 2000.

[30] F. C. Paixão, F. M. Silva, J. R. D. A. Miranda, and O. Baffa, "Magnetoresistive Sensors in a New Biomagnetic Instrumentation for Applications in Gastroenterology," in *Proceedings of 29th International Conference of Engineering in Medicine and Biology Society*, 2007, pp. 2948–2951.

[31] A. Platit, J. K. M. Vopalensky, and P. Ripka, "Precise AMR Magnetometer for Compass," in *Proceedings of IEEE Sensors*, 2003, pp. 472–476.

[32] J. Schotter *et al.*, "A Biochip Based on Magnetoresistive Sensors," *IEEE Trans. Magn.*, vol. 38, no. 5, pp. 3365–3367, 2002.

[33] L. K. Lagorce, O. Brand, and M. G. Allen, "Magnetic microactuators based on polymer magnets," *IEEE J. Microelectromechanical Syst.*, vol. 8, no. 1, pp. 2–9, 1999.

[34] T. S. Zhang, A. Kim, M. Ochoa, and B. Ziaie, "Controllable 'Somersault' Magnetic Soft Robotics," in *IEEE 28th International Conference on Microelectromechanical Systems (MEMS)*, 2015, pp. 1044–1047.

[35] J. Kim, S. E. Chung, S.-E. Choi, H. Lee, J. Kim, and S. Kwon, "Programming Magnetic Anisotropy in Polymeric Microactuators.," *Nat. Mater.*, vol. 10, no. 10, pp. 747–752, Oct. 2011, doi: 10.1038/nmat3090.

[36] S. H. Kim, K. Shin, S. Hashi, and K. Ishiyama, "Magnetic fish-robot based on multi-motion control of a flexible magnetic actuator.," *Bioinspir. Biomim.*, vol. 7, no. 3, p. 036007, Sep. 2012, doi: 10.1088/1748-3182/7/3/036007.

[37] M. Khoo and C. Liu, "Micro Magnetic Silicone Elastomer Membrane Actuator," *Sensors Actuators A Phys.*, vol. 89, no. 3, pp. 259–266, Apr. 2001, doi: 10.1016/S0924-4247(00)00559-8.

[38] R. Fuhrer, E. K. Athanassiou, N. A. Luechinger, and W. J. Stark, “Crosslinking Metal Nanoparticles into the Polymer Backbone of Hydrogels Enables Preparation of Soft, Magnetic Field-driven Actuators with Muscle-like Flexibility,” *Small*, vol. 5, no. 3, pp. 383–388, Mar. 2009, doi: 10.1002/smll.200801091.

[39] C. Chen, P. Huang, and B. Panigrahi, “An Artificial Cilia Based Micromixer for Superior Zebrafish Sperm Activation,” in *Proceedings of 30th IEEE International Conference on Microelectromechanical Systems*, 2017, pp. 1240–1243.

[40] Y. Feng, T. M. Abney, R. J. Okamoto, R. B. Pless, G. M. Genin, and P. V. Bayly, “Relative Brain Displacement and Deformation during Constrained Mild Frontal Head Impact,” *J. R. Soc. Interface*, vol. 7, no. 53, pp. 1677–1688, 2010, doi: 10.1098/rsif.2010.0210.

[41] L. Zhang, R. Makwana, and S. Sharma, “Brain Response to Primary Blast Wave using Validated Finite Element Models of Human Head and Advanced Combat Helmet,” *Front. Neurol.*, vol. 4, no. August, pp. 1–12, 2013, doi: 10.3389/fneur.2013.00088.

[42] T. Selbekk, R. Brekken, O. Solheim, S. Lydersen, T. A. N. Hernes, and G. Unsgaard, “Tissue Motion and Strain in the Human Brain Assessed by Intraoperative Ultrasound in Glioma Patients,” *Ultrasound Med. Biol.*, vol. 36, no. 1, pp. 2–10, 2010, doi: 10.1016/j.ultrasmedbio.2009.05.007.

[43] M. Hosseini-farid, M. Ramzanpour, M. Ziejewski, and G. Karami, “Estimating the Brain Strain Rates During Traumatic Brain Injury,” *Biomed. Sci. Instrum.*, vol. 54, no. 1, pp. 361–368, 2018.

[44] M. Hosseini-Farid, M. Amiri-Tehrani-Zadeh, M. Ramzanpour, M. Ziejewski, and G. Karami, “The Strain Rates in the Brain, Brainstem, Dura, and Skull under Dynamic Loadings,” *Math. Comput. Appl.*, vol. 25, no. 2, p. 21, 2020, doi: 10.3390/mca25020021.

[45] C. R. Bass, M. B. Panzer, K. A. Rafaels, G. Wood, J. Shridharani, and B. Capehart, “Brain injuries from blast,” *Ann. Biomed. Eng.*, vol. 40, no. 1, pp. 185–202, 2012, doi: 10.1007/s10439-011-0424-0.

[46] F. Pervin and W. W. Chen, “Dynamic Mechanical Response of Bovine Gray Matter and White Matter Brain Tissues under Compression,” *J. Biomech. Eng.*, vol. 42, no. 6, pp. 731–735, 2009, doi: 10.1016/j.jbiomech.2009.01.023.

[47] J. P. Sun *et al.*, “Noninvasive Quantification of Regional Myocardial Function Using Doppler-derived Velocity, Displacement, Strain Rate, and Strain in Healthy Volunteers: Effects of Aging,” *J. Am. Soc. Echocardiogr.*, vol. 17, no. 2, pp. 132–138, 2004, doi: 10.1016/j.echo.2003.10.001.

[48] T. Stanton, R. Leano, and T. H. Marwick, “Prediction of All-Cause Mortality from Global Longitudinal Speckle Strain: Comparison with Ejection Fraction and Wall Motion Scoring,” *Circ. Cardiovasc. Imaging*, vol. 2, no. 5, pp. 356–364, 2009, doi: 10.1161/CIRCIMAGING.109.862334.

[49] A. M. Shah *et al.*, "Prognostic Importance of Impaired Systolic Function in Heart Failure with Preserved Ejection Fraction and the Impact of Spironolactone," *Circulation*, vol. 132, no. 5, pp. 402–414, 2015, doi: 10.1161/CIRCULATIONAHA.115.015884.

[50] W. E. Baker, *Explosions in Air*. University of Texas Press, 1973.

[51] Z. Koccaz, F. Sutcu, and N. Torunbalci, "Architectural and Structural Design for Blast Resistant Buildings," in *14th World Conference on Earthquiake Engineering*, 2008, no. January.

[52] G. Ling, F. Bandak, R. Armonda, G. Grant, and J. Ecklund, "Explosive Blast Neurotrauma," *J. Neurotrauma*, vol. 825, no. June, pp. 815–825, 2009.

[53] A. Nakagawa *et al.*, "Mechanisms of Primary Blast-Induced Traumatic Brain Injury: Insights from Shock-Wave Research," *J. Neurotrauma*, vol. 1119, no. June, pp. 1101–1119, 2011, doi: 10.1089/neu.2010.1442.

[54] L. E. Goldstein, A. M. Fisher, C. A. Tagge, and X. Zhang, "Chronic Traumatic Encephalopathy in Blast-Exposed Military Veterans and a Blast Neurotrauma Mouse Model," *Sci. Transl. Med.*, vol. 4, no. 134ra60, 2012, doi: 10.1126/scitranslmed.3003716.

[55] G. Miller, "Blast Injuries Linked to Neurodegeneration in Veterans," *Science (80-.).*, vol. 336, no. May, pp. 790–791, 2012.

[56] J. M. Spikman, M. E. Timmerman, M. V Milders, W. S. Veenstra, and J. Van Der Naalt, "to General Cognitive Deficits , Injury Severity ," *J. Neurotrauma*, vol. 29, no. 1, pp. 101–111, 2012, doi: 10.1089/neu.2011.2084.

[57] H. G. Belanger, T. Kretzmer, and R. Yoash-gantz, "Cognitive Sequelae of Blast-related versus Other Mechanisms of Brain Trauma," *J. Int. Neuropsychol. Soc.*, vol. 15, pp. 1–8, 2009, doi: 10.1017/S1355617708090036.

[58] C. J. Bryan, T. A. Clemans, A. M. Hernandez, and M. D. Rudd, "Loss of Consciousness , Depression , Posttraumatic Stress Disorder , and Suicide Risk Among Deployed Military Personnel With Mild Traumatic Brain Injury," *J. Head Trauma Rehabil.*, vol. 28, no. 1, pp. 13–20, 2013, doi: 10.1097/HTR.0b013e31826c73cc.

[59] J. V Rosenfeld, A. C. Mcfarlane, P. Bragge, R. A. Armonda, J. B. Grimes, and G. S. Ling, "Blast-related traumatic brain injury," *Lancet Neurol.*, vol. 12, no. 9, pp. 882–893, 2013, doi: 10.1016/S1474-4422(13)70161-3.

[60] M. R. Galarneau, S. I. Woodruff, J. I. Dye, C. R. Mohrle, and A. L. Wade, "Traumatic Brain Injury during Operation Iraqi Freedom: Findings from the United States Navy–Marine Corps Combat Trauma Registry," *J. Neurosurg.*, vol. 108, no. May, pp. 950–957, 2008, doi: 10.3171/JNS/2008/108/5/0950.

[61] T. Tanielian and L. H. Jaycox, *Invisible Wounds of War: Psychological and Cognitive Injuries, Their Consequences, and Services to Assist Recovery*. 2008.

[62] R. A. Hurley *et al.*, "Blast-related Traumatic Brain Injury: What is Known?," *J. Neuropsychiatr.*, vol. 18, no. 2, pp. 141–145, 2006.

[63] C. R. Bass, K. A. Rafaels, and R. S. Salzar, "Pulmonary injury risk assessment for short-duration blasts," *J. Trauma - Inj. Infect. Crit. Care*, vol. 65, no. 3, pp. 604–615, 2008, doi: 10.1097/TA.0b013e3181454ab4.

[64] K. Rafaels *et al.*, "Survival risk assessment for primary blast exposures to the head," *J. Neurotrauma*, vol. 28, no. 11, pp. 2319–2328, 2011, doi: 10.1089/neu.2009.1207.

[65] C. Mac Donald, A. Johnson, and D. Cooper, "Detection of Blast-related Traumatic Brain Injury in US Military Personnel," *N. Engl. J. Med.*, vol. 364, pp. 2091–2100, 2011, doi: 10.1016/j.yccm.2011.08.007.

[66] R. D. Readnower *et al.*, "Increase in Blood-brain Barrier Permeability, Oxidative Stress, and Activated Microglia in a Rat Model of Blast-Induced Traumatic Brain Injury," *J. Neurosci. Res.*, vol. 88, no. September, pp. 3530–3539, 2010, doi: 10.1002/jnr.22510.

[67] G. A. Elder and A. Cristian, "Blast-Related Mild Traumatic Brain Injury: Mechanisms of Injury and Impact on Clinical Care," *Mt. Sinai Jouernal Med.*, pp. 111–118, 2009, doi: 10.1002/MSJ.

[68] I. Cernak and L. J. Noble-haeusslein, "Traumatic brain injury: an overview of pathobiology with emphasis on military populations," *J. Cereb. Blood Flow Metab.*, vol. 30, no. 2, pp. 255–266, 2009, doi: 10.1038/jcbfm.2009.203.

[69] H. Fischer, "U.S. Military Casualty Statistics : Operation New Dawn, Operation Iraqi Freedom, and Operation Enduring Freedom," 2013.

[70] S. Okie and S. D. Emme, "Traumatic Brain Injury in the War Zone," *N. Engl. J. Med.*, vol. 352, pp. 2043–2047, 2005.

[71] P. A. Taylor and C. C. Ford, "Simulation of Blast-induced Early-time Intracranial Wave Brain Injury," *J. Biomech. Eng.*, vol. 131, pp. 1–11, 2016, doi: 10.1115/1.3118765.

[72] A. Sundaramurthy, A. Alai, S. Ganpule, A. Holmberg, E. Plougonven, and N. Chandra, "Blast-Induced Biomechanical Loading of the Rat: An Experimental and Anatomically Accurate Computational Blast Injury Model," *J. Neurotrauma*, vol. 29, pp. 2352–2364, 2012, doi: 10.1089/neu.2012.2413.

[73] M. Chavko, T. Watanabe, S. Adeeb, J. Lankasky, S. T. Ahlers, and R. M. Mccarron, "Relationship between Orientation to A Blast and Pressure Wave Propagation inside the Rat Brain," *J. Neurosci. Methods*, vol. 195, no. 1, pp. 61–66, 2011, doi: 10.1016/j.jneumeth.2010.11.019.

[74] M. A. O'Reilly, A. Muller, and K. Hynynen, "Ultrasound Insertion Loss of Rat Parietal Bone Appears to Be Proportional to Animal Mass at Sub-megahertz Frequencies," *Ultrasound Med. Biol.*, vol. 37, no. 11, pp. 1930–1937, 2012, doi: 10.1016/j.ultrasmedbio.2011.08.001.Ultrasound.

[75] M. B. Panzer, B. S. Myers, B. P. Capehart, and C. R. Bass, "Development of a Finite Element Model for Blast Brain Injury and the Effects of CSF Cavitation," *Ann. Biomed. Eng.*, vol. 40, no. 7, pp. 1530–1544, 2012, doi: 10.1007/s10439-012-0519-2.

[76] M. Skotak *et al.*, "Rat Injury Model under Controlled Field-Relevant Primary Blast Conditions : Acute Response to a Wide," *J. Neurotrauma*, vol. 30, pp. 1147–1160, 2013, doi: 10.1089/neu.2012.2652.

[77] M. S. Chafi, S. Ganpule, and L. Gu, "Dynamic Response of Brain Subjected to Blast Loadings: Influence of Frequency Ranges," *Int. J. Appl. Mech.*, vol. 3, no. 4, pp. 803–823, 2011, doi: 10.1142/S175882511100124X.

[78] S. Budday *et al.*, "Mechanical Properties of Gray and White Matter Brain Tissue by Indentation," *J. Mech. Behav. Biomed. Mater.*, vol. 46, pp. 318–330, 2015, doi: 10.1016/j.jmbbm.2015.02.024.

[79] G. R. Diresta, J. Lee, N. Lau, F. Ali, J. H. Galicich, and E. Arbit, "Measurement of Brain Tissue Density Using Pycnometry," *Acta Neurochir. Suppl.*, vol. 36, pp. 34–36, 1990.

[80] I. Ennen, D. Kappe, T. Rempel, C. Glenske, and A. Hütten, "Giant Magnetoresistance: Basic Concepts, Microstructure, Magnetic Interactions and Applications," *Sensors*, vol. 16, no. 6, pp. 904–928, 2016, doi: 10.3390/s16060904.

[81] NVE Corporation, "AA/AB-Series Analog Magnetic Sensors," 2017.

[82] C. Blaise, F. Gagne, J. F. Fe, E. Canada, and M. Street, "Ecotoxicity of Selected Nano-Materials to Aquatic Organisms," *Environ. Toxicol.*, vol. 21, pp. 591–598, 2008, doi: 10.1002/tox.

[83] B. M. Kirrane, L. S. Nelson, and R. S. Hoffman, "Massive Strontium Ferrite Ingestion without Acute Toxicity," *Basic Clin. Pharmacol. Toxicol.*, vol. 99, pp. 358–359, 2006.

[84] M. Bellusci *et al.*, "Biodistribution and Acute Toxicity of a Nanofluid Containing Manganese Iron Oxide Nanoparticles Produced by a Mechanochemical Process," *Int. J. Nanomedicine*, vol. 9, no. 1, pp. 1919–1929, 2014.

[85] N. Grimaudo, "Biocompatibility of Nickel and Cobalt Dental Alloys," *Gen. Dent.*, vol. 49, no. 5, pp. 498–503, 2001.

[86] V. E. Donohue, F. Mcdonald, and R. Evans, "In Vitro Cytotoxicity Testing of Neodymium-Iron-Boron Magnets," *J. Appl. Biomater.*, vol. 6, no. 1, pp. 69–74, 1995.

[87] U. Arif *et al.*, “Biocompatible Polymers and their Potential Biomedical Appplications: A Review,” *Curr. Pharm. Des.*, vol. 25, no. 34, pp. 3608–3619, 2019.

[88] A. Colas and J. Curtis, “Silicone Biomaterials: History and Chemistry Medical Applications of Silicones,” in *Biomaterials Science: An Introduction to Materials in Medicine*, 1996, pp. 80–86, 697–707.

[89] A. Savitzky and M. J. E. Golay, “Smoothing and Differentiation of Data by Simplified Least Squares Procedures,” *Anal. Chem.*, vol. 36, no. 8, pp. 1627–1639, 1964, doi: 10.1021/ac60214a048.

[90] N. S. Race, “Causes and Consequences of Mild Blast-Induced Traumatic Brain Injury: From Biomechanics to Behavior,” 2017.

[91] J. Weickenmeier *et al.*, “Brain Stiffens Post Mortem,” *J. Mech. Behav. Biomed. Mater.*, vol. 84, no. April, pp. 88–98, 2018, doi: 10.1016/j.jmbbm.2018.04.009.

[92] R. J. Sevick *et al.*, “Cytotoxic Brain Edema: Assessment with Diffusion-Weighted MR Imaging,” *Radiology*, vol. 185, no. 3, pp. 687–690, 1992, doi: 10.1148/radiology.185.3.1438745.

[93] W. C. Risher, D. Croom, and S. A. Kirov, “Persistent Astroglial Swelling Accompanies Rapid Reversible Dendritic Injury during Stroke-Induced Spreading Depolarizations,” *Glia*, vol. 60, no. 11, pp. 1709–1720, 2012, doi: 10.1002/glia.22390.

[94] A. L. Bui, T. B. Horwich, and G. C. Fonarow, “Epidemiology and Risk Profile of Heart Failure,” *Nat. Rev. Cardiol.*, vol. 8, no. 1, pp. 30–41, 2011, doi: 10.1038/nrcardio.2010.165.

[95] W. T. Abraham *et al.*, “Wireless Pulmonary Artery Haemodynamic Monitoring in Chronic Heart Failure: a Randomised Controlled Trial,” *Lancet*, vol. 377, pp. 658–666, 2011, doi: 10.1016/S0140-6736(11)60101-3.

[96] F. Cros, D. O’Brien, M. Fonseca, M. Abercrombie, J. W. Park, and A. Singh, “Method of Manufacturing Implantable Wireless Sensor for In-vivo Pressure Measurement,” US 7,621,036B2, 2009.

[97] K. S. Coyne *et al.*, “The Prevalence of Lower Urinary Tract Symptoms (LUTS) in the USA, the UK and Sweden: Results from the Epidemiology of LUTS (EpiLUTS) Study,” *BJU Int.*, vol. 104, no. 3, pp. 352–360, 2009, doi: 10.1111/j.1464-410X.2009.08427.x.

[98] Y. Wang, H. Hu, K. Xu, X. Wang, Y. Na, and X. Kang, “Prevalence, Risk Factors and the Bother of Lower Urinary Tract Symptoms in China: a Population-Based Survey,” *Int. Urogynecol. J.*, vol. 26, no. 6, pp. 911–919, 2015, doi: 10.1007/s00192-015-2626-8.

[99] F. M. Waltz and W. E. Bradley, “Bladder Volume Sensing by Resistance Measurement,” *IEEE Trans. Biomed. Eng.*, vol. 18, no. 1, pp. 42–46, 1971.

[100] J. C. Denniston and L. E. Baker, “Measurement of Urinary Bladder Emptying using Electrical Impedance,” *Med. Biol. Eng.*, vol. 13, no. 2, pp. 305–306, 1975, doi: 10.1007/BF02477745.

[101] P. Petrican and M. A. Sawan, “Design of a Miniaturized Ultrasonic Bladder Volume Monitor and Subsequent Preliminary Evaluation on 41 Enuretic Patients,” *IEEE Trans. Rehabil. Eng.*, vol. 6, no. 1, pp. 66–74, 1998, doi: 10.1109/86.662622.

[102] S. Rajagopalan, M. Sawan, E. Ghafar-Zadeh, O. Savadogo, and V. P. Chodavarapu, “A Polypyrrole-Based Strain Sensor Dedicated to Measure Bladder Volume in Patients with Urinary Dysfunction,” *Sensors*, vol. 8, no. 8, pp. 5081–5095, 2008, doi: 10.3390/s8085081.

[103] J. Wang *et al.*, “Micturition Alert Device Dedicated to Neurogenic Bladders,” *Zhongguo Xiu Fu Chong Jian Wai Ke Za Zhi*, vol. 22, no. 5, pp. 597–601, 2008.

[104]T. Yamada *et al.*, “A stretchable carbon nanotube strain sensor for human-motion detection,” *Nat. Nanotechnol.*, vol. 6, no. 5, pp. 296–301, 2011, doi: 10.1038/nnano.2011.36.

[105] J.-B. Chossat, Y.-L. Park, R. J. Wood, and V. Duchaine, “A soft strain sensor based on ionic and metal liquids,” *IEEE Sens. J.*, vol. 13, no. 9, pp. 3405–3414, 2013, doi: 10.1109/JSEN.2013.2263797.

[106] P. Choquet, F. Juneau, and F. Dadoun, “New generation of fiber-optic sensors for dam monitoring,” in *Proceedings of the International Conference of Dam Safety and Monitoring*, 1999, no. October, pp. 1–10.

[107] R. Melik, N. K. Perkgoz, E. Unal, C. Puttlitz, and H. V. Demir, “Bio-implantable passive on-chip RF-MEMS strain sensing resonators for orthopaedic applications,” *J. Micromechanics Microengineering*, vol. 18, no. 11, 2008, doi: 10.1088/0960-1317/18/11/115017.

[108] S. Madersbacher, A. Pycha, G. Schatzl, C. Mian, C. H. Klingler, and M. Marberger, “The Aging Lower Urinary Tract: A Comparative Urodynamic Study of Men and Women,” *Urology*, vol. 51, no. 2, pp. 206–212, 1998, doi: 10.1016/S0090-4295(97)00616-X.

[109] A. R. Mclean, M. E. Richards, C. S. Crandall, and J. L. Marinaro, “Ultrasound Determination of Chest Wall Thickness: Implications for Needle Thoracostomy,” *Am. J. Emerg. Med.*, vol. 29, no. 9, pp. 1173–1177, 2011, doi: 10.1016/j.ajem.2010.06.030.

[110] E. Arribas, I. Escobar, and C. P. Suarez, “Measurement of the Magnetic Field of Small Magnets with a Smartphone: a Very Economical Laboratory Practice for Introductory Physics Courses,” *Eur. J. Phys.*, vol. 36, no. 6, pp. 1–11, 2015, doi: 10.1088/0143-0807/36/6/065002.

[111] T. E. C. Inc., “Reance F™ Flexible Neodymium Rare Earth Magnets,” 2013. [Online]. Available: http://www.edyne.com/products/flexiblemagnets/flexibleneodymiumironboron.aspx.

[112] O. Akkus, A. Oguz, M. Uzunlulu, and M. Kizilgul, "Evaluation of Skin and Subcutaneous Adipose Tissue Thickness for Optimal Insulin Injection," *J. Diabetes Metab.*, vol. 3, no. 8, p. 1000216, 2012, doi: 10.4172/2155-6156.1000216.

[113] N. Naserifar, P. R. Leduc, and G. K. Fedder, "Material Gradients in Stretchable Substrates toward Integrated Electronic Functionality," *Adv. Mater.*, vol. 28, pp. 3584–3591, 2016, doi: 10.1002/adma.201505818.

[114] K. M. Inc., "Halbach Arrays." [Online]. Available: https://www.kjmagnetics.com/blog.asp?p=halbach-arrays. [Accessed: 10-Dec-2020].

[115] A. M. Maceira, S. K. Prasad, M. Khan, and D. J. Pennell, "Reference Right Ventricular Systolic and Diastolic Function Normalized to Age , Gender and Body Surface Area from Steady-state Free Precession Cardiovascular Magnetic Resonance," *Eur. Heart J.*, vol. 27, pp. 2879–2888, 2006, doi: 10.1093/eurheartj/ehl336.

[116] G. Park *et al.*, "Immunologic and Tissue Biocompatibility of Flexible / Stretchable Electronics and Optoelectronics," *Adv. Healthc. Mater.*, vol. 3, pp. 515–525, 2014, doi: 10.1002/adhm.201300220.

[117] L. Bondemark, J. Kurol, and A. Wennberg, "Orthodontic Rare Earth Magnets: In Vitro Assessment of Cytotoxicity," *Br. J. Orthod.*, vol. 21, no. 4, pp. 335–341, 1994, doi: 10.1179/bjo.21.4.335.

[118] A. Kondo and J. G. Susset, "Physical Properties of the Urinary Detrusor Muscle: A Mechanical Model Based upon the Analysis of Stress Relaxation Curve," *J. Biomech.*, vol. 6, no. 2, 1973, doi: 10.1016/0021-9290(73)90083-3.

[119] J. Malone-Lee and I. Wahedna, "Characterisation of Detrusor Contractile Function in Relation to Old Age," *Br. J. Urol.*, vol. 72, no. 6, pp. 873–880, 1993, doi: 10.1111/j.1464-410X.1993.tb16289.x.

[120] M. K. Walls *et al.*, "Structural and Biochemical Abnormalities in the Absence of Acute Deficits in Mild Primary Blast-Induced Head Trauma," *J. Neurosurg.*, vol. 124, no. 3, pp. 675–686, 2015, doi: 10.3171/2015.1.JNS141571.

[121] R. Shi and N. Race, "Mild Blast-Induced Traumatic Brain Injury Model," in *Animal Models of Acute Neurological Injury*, 2019, pp. 367–378.

[122] T. Zhang, M. Ochoa, R. Rahimi, and B. Ziaie, "A Wireless , Smartphone-Aided Magnetic Strain Sensor for Biomedical Applications," in *IEEE 30th International Conference on Microelectromechanical Systems (MEMS)*, 2017, pp. 235–238.

VITA

Born February 18th, 1991 in the China-Japan Friendship Hospital in Beijing, China, Tianshuo Zhang is the only child of Xu Zhang and Xiaojie Pan. At the age of 6, he was given the English name Tony by his English teacher and had been using it since then. He attended High School Affiliated to Renmin University of China, also known as RDFZ, and graduated in 2009. For undergraduate study, Tony went to Rensselaer Polytechnic Institute in Troy, New York and graduated *cum laude* with dual degrees in Electrical Engineering and Applied Physics. His senior design project is to develop a low-cost wind turbine blade damage probing system for General Electric. During his junior and senior year, Tony conducted research on electro-optical modulator devices under Professor Zhaoran Huang.

Upon graduation in 2013, Tony enrolled to the direct-Ph.D. program in Electrical Engineering at Purdue University West Lafayette campus. Fascinated by the idea of wearable and stretchable sensors and circuitries for biomedical applications, he began research under the supervision of Professor Babak Ziaie. Tony's research focused on wireless magnetic sensing of tissue deformations to gain insights of inner organs such as brain, heart, or bladder. This is a highly interdisciplinary topic that involves extensive collaboration, especially with Professor Riyi Shi of the Weldon School of Biomedical Engineering. Through various research projects he gained skills and knowledge in magnetic fundamentals, signal processing, image processing, and physiological topics. Aside from conducting research, Tony had also been serving as a teaching assistant for undergraduate calculus and circuit courses. In addition, he completed R&D internships at Microsoft Research Asia for HoloLens, and at Xmotors.ai for driver monitoring system.

Besides academic and professional endeavor, Tony has been in a relationship with his high school classmate, Xufei Xu, since 2011. They share passions in workout, cooking, cats and animal welfare.

PUBLICATIONS

[1] TS. Zhang, Y. Guo, and C. Lu, "Apparatus and Method for Measuring Physiological Information of Living Subject in Vehicle", US Patent 10696305, June 30, 2020

[2] TS. Zhang, M. Ochoa, R. Rahimi, and B. Ziaie, "A Wireless, Smartphone-Aided Magnetic Strain Sensor for Biomedical Applications", *2017 30th IEEE International Conference on Micro Electromechanical Systems (MEMS)*, 2017, pp. 235-238.

[3] N. Race, G. Acosta, S. Vega-Alvarez, E. Lungwitz, TS. Zhang, W. Truitt, B. Ziaie, and R. Shi, "Psychosocial Learning Deficits After Mild Blast Injury Are Induced by Intracranial Deformation and Oxidative Stress", *Journal of Neurotrauma*, vol. 33, no. 13, PSA-033, 2016.

[4] S. Song, N. Race, A. Kim, TS. Zhang, R. Shi, and B. Ziaie, "A Wireless Intracranial Brain Deformation Sensing System for Blast-Induced Traumatic Brain Injury", *Scientific Reports*, 5, 16959, 2015, https://doi.org/10.1038/srep16959.

[5] W. Seo, W. Yu, T. Tan, J. Zhou, TS. Zhang, B. Ziaie, and B. Jung, "Diaper-Embedded Urinary Tract Infection Monitoring System Powered by A Urine-Powered Battery", *2015 IEEE Biomedical Circuits and Systems Conference (BioCAS)*, 2015, pp. 1-4.

[6] TS. Zhang, A. Kim, M. Ochoa, and B. Ziaie, "Controllable 'Somersault' Magnetic Soft Robotics", *2015 28th IEEE International Conference on Micro Electromechanical Systems (MEMS)*, 2015, pp. 1044-1047.

[7] N. Race, M. Walls, S. Vega-Alverez, S. Song, A. Kim, TS. Zhang, B. Ziaie, and R. Shi, "Brain Deformation, Structural Damage, and Biochemical Alterations in Mild Blast-Induced TBI in Rats", *2014 Annual Meeting of Biomedical Engineering Society (BMES)*, 2014.

[8] S. Song, A. Kim, TS. Zhang, N. Race, Y. Gu, B. Ziaie, and R. Shi, "Intracranial Deformation Sensor for Blast-Induced Traumatic Brain Injury", *2014 Annual Meeting of Biomedical Engineering Society (BMES)*, 2014.

[9] TS. Zhang, P. Wu, ZR. Huang, "Linear PNP Silicon EO Modulator for Analog Applications", *Asia Communications and Photonics Conference*, AF2B.13, 2013.